ANKARA YILDIRIM BEYAZIT UNIVERSITY

GRADUATE SCHOOL OF NATURAL AND APPLIED SCIENCES

DEVELOPMENT OF HIGH-STRENGTH AND CORROSION-RESISTANT ALUMINUM ALLOYS

Ph.D. Thesis by

Furkan ÖZDEMİR

Department of Materials Engineering

September 2022

ANKARA

DEVELOPMENT OF HIGH-STRENGTH AND CORROSION-RESISTANT ALUMINUM ALLOYS

A Thesis Submitted to

The Graduate School of Natural and Applied Sciences of

Ankara Yıldırım Beyazıt University

In Partial Fulfillment of the Requirements for the Degree of Doctor of Philosophy in Materials Engineering, Department of Materials Engineering

by

Furkan ÖZDEMİR

September 2022

ANKARA

Ph.D. THESIS EXAMINATION RESULT FORM

We have read the thesis entitled **"DEVELOPMENT OF HIGH-STRENGTH AND CORROSION RESISTANT ALUMINUM ALLOYS"** completed by **FURKAN ÖZDEMİR** under the supervision of **PROF. DR. HASAN OKUYUCU** and we certify that in our opinion it is fully adequate, in scope and in quality, as a thesis for the degree of Doctor of Philosophy.

Prof. Dr. Hasan OKUYUCU

Supervisor

Prof. Dr. Özgül KELEŞ	Prof. Dr. Ahmet TÜRK
Jury Member	Jury Member
Prof. Dr. Abdullah YILDIZ	Assist. Prof. Dr. M. Fatih ÖKTEM
Jury Member	Jury Member

Prof. Dr. Sadettin ORHAN

Director

Graduate School of Natural and Applied Sciences

ETHICAL DECLARATION

I hereby declare that, in this thesis which has been prepared in accordance with the Thesis Writing Manual of Graduate School of Natural and Applied Sciences,

- All data, information and documents are obtained in the framework of academic and ethical rules,
- All information, documents and assessments are presented in accordance with scientific ethics and morals,
- All the materials that have been utilized are fully cited and referenced,
- No change has been made on the utilized materials,
- All the works presented are original,

and in any contrary case of above statements, I accept to renounce all my legal rights.

Date: 14.09.2022 **Signature:……..**

Name & Surname: Furkan ÖZDEMİR

ACKNOWLEDGEMENTS

I would like to express my gratitude to the all people who contributed in some way to the work described in this thesis. First, I would like to thank my advisor, Professor Hasan Okuyucu, for his guidance, encouragement, and confidence in me. This endeavor would not have been possible without his support.

I would like to express my heart-felt gratitude to Associate Professor Rajeev Kumar Gupta for providing me all the facilities and his research laboratories at University of Akron and North Carolina State University. He has been and inspiring mentor for all the time of my academic and daily life. I consider myself to be extremely privileged to work with him. With his guidance, I've grown as a scientist and expanded the limits of my intellect and intelligence.

I would like to thank my examining committee members, Prof. Dr. Özgül Keleş, Prof. Dr. Ahmet Türk, Prof. Dr. Abdullah Yıldız and Assist. Prof. Dr. M. Fatih Öktem for their criticism, insightful comments and valuable contributions to this work.

I would like to extend my deepest gratitude to my colleagues and lab mates in Ankara, Akron, and Raleigh. Especially, Farooq, Jijo, Sandamal, Bhuvana, Sean, Nazenin, Luiza, and Ahmed for their friendship, help in adjusting my life in the US and technical discussions that I really enjoyed.

Financial support from Scientific and Technological Research Council of Turkey (TÜBITAK) by 2214/A program is highly appreciated.

Financial support by the National Science Foundation (NSF-CMMI 2131440) under the direction of Dr. Alexis Lewis is highly acknowledged.

Most of all, I would like to thank my family, my parents, and my brother for all the support. Finally, I would like to thank my wife, Merve for all her constant support encouragement and trust. Without their support, none of this would have been possible.

DEVELOPMENT OF HIGH-STRENGTH AND CORROSION-RESISTANT ALUMINUM ALLOYS

ABSTRACT

Aluminum alloys are of outstanding importance to industries requiring lightweight materials. The remarkable properties of Al alloys, which come in a variety of grades, are unsurpassed for many applications. However, these properties are limited by conventional techniques, and given the potential of aluminum alloys, novel techniques and materials are critical to achieving alloys with superior properties. The interplay between strength and corrosion is a rarity in Al alloys, as the corrosion resistance of Al alloys has deteriorated following efforts to strengthen them.

The present study aims to simultaneously enhance the strength and corrosion performance of Al alloys through nanocrystalline structure, enhanced solubility of alloying elements and uniform distribution of secondary phases by high energy ball milling.

The present work involves the synthesis and characterization of ultra-high strength, highly corrosion resistant light Al alloys by high energy ball milling and suitable alloying elements. The methodology includes a top-down approach starting with high-energy ball milling of commercial age-hardening alloys and modifying process parameters to achieve higher alloy performance. Finally, based on the knowledge gained from commercial alloys, the synthesis of binary alloys and the mechanisms that provide excellent properties were investigated.

Many viable alloying elements were investigated to fill the research gap on binary Al alloys, although the role of each alloying element may vary and therefore each alloy system should be treated as an individual case. Therefore, the corrosion protection mechanism of the Al-Fe system has been studied in detail through electrochemical along with analytical techniques such as XPS, TEM, SIMS. Understanding how Fe significantly improves the corrosion resistance of Al in solid solution and nanocrystalline structure can guide the development of a new generation of light metal

alloys for applications with the most desired mechanical properties and aggressive environments.

Keywords: Aluminum alloys, Pitting corrosion, nanocrystalline alloys, Localized corrosion, Aluminum alloy corrosion, Strength, High-energy ball milling

YÜKSEK MUKAVEMETLİ VE KOROZYONA DİRENÇLİ ALÜMİNYUM ALAŞIMLARININ GELİŞTİRİLMESİ

ÖZ

Alüminyum alaşımları, hafif malzemelere gereksinim duyan uygulamalar için son derece kritik bir öneme sahiptir. Sahip olduğu özellikleri ve farklı alaşım elementleriyle çeşitlendirilebilirliği, alüminyumu bir çok farklı alanda ve mühendislik uygulamalarında tercih edilmesini sağlamaktadır. Ancak aliminyumun bu cazip özellikleri geleneksel üretim yöntemleriyle elde edilen alaşımlarda sınırlı kalmaktadır. Aliminyum alaşımlarında üstün özellikler elde etmek için yenilikçi üretim yöntemlerine ihtiyaç vardır. Ayrıca, alüminyuma mukavemet kazandırmak için yapılan işlemler korozyon dayanımını önemli ölçüde zayıflatmakta ve korozyon direncinin düşmesine yol açmaktadır.

Bu çalışmada amaç; nanokristal yapının, çözünürlük sınırını aşmış alaşım elementlerinin etkisinin ve muhtemel ikincil fazların düzgün dağılımının sonucunda alüminyum alaşımlarının mukavemet ve korozyon performansını eş zamanda artırmaktır.

Bu çalışma, yüksek mukavemete ve korozyon performansına sahip alüminyum alaşımlarının uygun kompozisyon ve parametrelerle üretimi için yüksek enerjili bilyalı değirmen ile sentezi ve karakterizasyonunu içermektedir. Çalışmada tümden gelime benzer bir deneysel metodoloji uygulanmıştır. Başlangıçta, hali hazırda ticari uygulamaları bulunan çökeltme ile sertleştirilebilir sınıftaki alüminyum alaşımları çalışılmış, sonrasında proses parametreleri ve kompozisyonal etkiler irdelenmiş, en sonunda da elde edilen bulgular ışığında bir dizi yeni alaşımlar üretilmiştir.

Bu alandaki bilimsel boşluğu doldurmak için yapılan deneysel çalışmalar sonucunda her bir alaşım elementinin rolünün farklı olduğu ve mekanizmalarının anlaşılması için her bir alaşımın ayrı ayrı irdelenmesi gerektiği saptanmıştır. Bu yüzden de, Al-Fe alaşımı elektrokimyasal ve XPS, SIMS, TEM gibi analitik teknikler kullanılarak ayrıntılı şekilde irdelenmiştir. Geleneksel üretim yöntemlerinde istenmeyen bir element ya da bir safsızlık göstergesi olarak kabul edilen demirin bir alaşım elementi

olarak kullanıldığı Al-Fe alaşımı son derece yüksek korozyon direnci göstermiştir. Hali hazırda çok yüksek mukavemete sahip olduğu literatürde de bilinen bu alaşımın gösterdiği yüksek korozyon performansının nedenleri; ikincil fazlarla matriks arasında azalan galvanik farka, pasif film yapısındaki Fe katılımı sonucu oluşan pasivasyon kabilyetinin artmasına ve metal film arayüzündeki Fe zenginleşmesine bağlanmıştır.

Maliyet, erişilebilirlik gibi faktörlerin yanı sıra geri dönüştürülmüş malzemelerin yüksek performanslı alaşımlar olarak değerlendirilmesin sağlayabilecek olan bu alaşımlar, korozif ortamlarda yüksek performans gösteren alaşımların geliştirilmesi noktasında önemli bir potansiyel vaad etmektedir.

Anahtar Kelimeler: Alümiyum alaşımları, Alüminyum korozyonu, Lokalize korozyon, nanokristal alaşımlar, Yüksek-enerjili bilyalı öğütme, mukavemet

CONTENTS

NOMENCLATURE

Abbreviations

µA	Microampere
µm	Micrometer
nm	Nanometer
Å	Angstrom
cm^2	Square centimeter
°F	Fahrenheit
g	Gram
GPa	Gigapascal
h	Hour
HV	Hardness Vickers
K	Kelvin
mV	Milivolt
kV	Kilovolt
mΩ	Milliohm
mA	Milliampere
M	Molar
rpm	Round per minute
ppm	Part per million
wt.%	Weight percent
at.%	Atomic percent

Acronyms

IADS	International Alloy Designation System

HEBM	High-energy ball milling
IMP	Intermetallic particles
PCA	Process controlling agent
SCE	Saturated Calomel Electrode
DC	Direct current
EDS	Energy dispersive spectroscope
FCC	Face-centered cubic
FWHM	Full widths at half maximum
JCPDS	Joint committee on powder diffraction standards
SEM	Scanning electron microscope
TEM	Transmission electron microscope
FIB	Focused Ion Beam
XRD	X-ray diffractometer
XPS	X-ray photoelectron spectrometer
SADP	Selected area diffraction pattern
ToF-SIMS	Time of Flight-Secondary Ions Mass Spectrometer

LIST OF TABLES

LIST OF FIGURES

CHAPTER 1

INTRODUCTION

Aluminum which is one of the most abundant elements in the earth's crust has gained much importance since the beginning of the 19th century. It has a wide range of applications ranging from household uses to aerospace applications. Especially in the automotive and aerospace industries, aluminum has continuously gained importance due to its high strength and low weight. Aluminum, which has a density of about one-third that of steel, can achieve high strength without significantly increasing its density by introducing some alloying elements [1].

The mechanical properties of aluminum alloys are significantly enhanced by the introduction of alloying elements in combination with thermomechanical treatments and, in particular, by age hardening in the 2xxx, 6xxx, and 7xxx alloy series. However, only a limited number of elements are soluble to any appreciable extent, so most alloying elements are revealed in the form of secondary phases, which are responsible for localized corrosion due to their different electrochemical nature.

Al alloys possess the potential to enhance the current properties. The need for high-strength alloys with low weight makes Al alloys very attractive to be processed in various non-equilibrium processes. Among these processes, microstructures that provide nano-grains attracted serious research attention, such as equal-channel angular pressing or extrusion [2,3], high pressure torsion [4], surface mechanical treatment [5], and high-energy ball milling [6,7].

Research has mainly focused on enhancing the mechanical performance of Al alloys through methods that provide nanocrystalline structure. Significant improvements have been reported for Al alloys exceeding a yield strength of 1 GPa [8]. However, little research on the corrosion behavior of these alloys is scarce. Esquivel and Gupta reported the simultaneous improvement in strength and corrosion of Al alloys produced by high-energy ball milling [9]. Unlike other techniques, high-energy ball milling is reported to provide bulk structures or powders that can be consolidated into

the desired shape, while other methods such as ion implementation [10] and sputter or vapor deposition [11,12] produce structures in the form of thin films.

Research in the field of high strength corrosion-resistant alloys is scarce and there is a research gap that needs to be filled. The present study takes an action about the development and characterization of Al alloys that warrant significant research.

The present study followed a top-down like methodology and aimed to investigate the corrosion and hardness of nanocrystalline age hardening Al alloys vis a vis commercial age hardening alloys at the beginning. Then, the influence of milling atmosphere and compositional modifications are investigated. Finally, the binary Al-Zr, Y, La, and Fe alloys are investigated. All of the specific objectives present a novel and original contribution to the literature and to the overall goal of developing high-strength corrosion-resistant Al alloys.

Advances in today's technology demand more energy-efficient and environmentally friendly materials and processes. The results of this research would bring significant improvements in the scopes of recycling and advanced processing techniques that demand improved materials.

CHAPTER 2

LITERATURE REVIEW

Aluminum due to its various properties that makes it unique and versatile in many cases, finds a wide range of applications in many industries including applications from wrapping foils to high-tech engineering applications. Aluminum is ranked in second place after steels for structural use [13]. However, the density of aluminum is superior to steel and many other metals by the virtue of being a lightweight metal. The density (2.7 g/cm^3) is approximately one-third of steel density (7.83 g/cm^3) and when coupled with high strength, enables the designing and employing of lightweight structures which are significant for transportation considerations ranging from land to space vehicles. [1,13]. The general classification of aluminum alloys and microstructural features is reviewed under section 2.1.

Aluminum is a fairly active metal, but due to the formation of a thin protective oxide layer on its surface, pure aluminum exhibits corrosion resistance in certain environments. Nevertheless, efforts made to end up with a high-strength aluminum significantly deteriorate the corrosion resistance of aluminum alloys. The high strength and excellent corrosion resistance is a combination that are not found in aluminum alloys. The fundamentals of aluminum corrosion are reviewed in section 2.3.

Nanocrystalline materials are one of the most important milestones in the history of materials science. Since their first introduction, the studies conducted on nanocrystalline materials demonstrate significantly different results than their counterparts [14]. The nanocrystalline Al alloys and corrosion of nanocrystalline Al alloys are reviewed in sections 2.3 to 2.5, respectively.

The specific literature review and background information are divided into chapters according to the approach and methodology. The specific details including the specific literature review can be found in each Chapters 2 to 8.

2.1 Al and Al Alloys

Production of aluminum is mainly divided into two categories as primary production, in which aluminum is extracted from aluminum-bearing minerals, and secondary production, which is the production from aluminum scrap.

Primary production of aluminum includes steps like Bauxite ore dressing (beneficiation), production of refined alumina from bauxite ore (Bayer Process) [15], and metallic Al production by molten salt electrolysis (Hall-Herault process) [16]. Secondary production includes steps like pretreatment and smelting/refining from the scrap. Al production in general, requires melting, refining, and introducing alloying elements to achieve demanded chemical composition and casting.

Aluminum alloys are divided into two main categories: Cast aluminum alloys and wrought aluminum alloys. The shape and intended use of the end product determines the class of aluminum. Wrought alloys are formed into the shape of rods, bars, plates, sheets/foils with the help of mechanical forces, while cast alloys are produced in the form of more irregular/complex shapes such as engine blocks, frames for direct use, or in the form of ingots that can be an intermediate product for further alloy processing.

2.1.1 Alloy Nomenclature

The International Alloy Designation System (IADS) has established the most widely accepted nomenclature for Al alloys since the 1970s. The system has its base on the classification system used by the Aluminum Association of the United States [1].

The IADS designates a four-digit number for each class of alloys where the first digit is based on the principal alloying element [13]. The 1xxx series of alloys have no primary alloying element, 2xxx series of alloys in which copper is the primary alloying element, 3xxx series in which the manganese is the main alloying element, 4xxx is the series of alloy in which silicon is the main alloying element, 5xxx is the alloy series which magnesium is the primary alloying element, 6xxx series is which the magnesium and silicon are main alloying elements, and 7xxx series of the alloys which zinc is the main alloying element. Last two digits of the 1xxx series provide

information about the purity of the alloy while this phenomenon does not apply to other alloy series. However, the second digit indicates the purity or any modification in the alloy in all series. For example, 2024 and 2124 differ only slightly in the alloy composition.

2.1.1.1 Wrought Alloys

Alloy series are explained in 2.1.1 which provides brief information about the alloying elements in the alloy series determined by the association. Wrought alloys are distinguished from cast alloys, in which the aluminum is melted and shaped through casting, while wrought alloys are shaped without melting.

1xxx series: Minimum 99% of aluminum-containing alloys with Fe and Si as major impurities. Frequently desired in chemical and electrical applications due to high thermal conductivity and good corrosion resistance.

2xxx series: Mg is usually found in this alloy system as a secondary alloying element along with a main alloying element of copper. Heat treatment is conducted to provide strength increase and it is preferred in applications where high strength and low-weight are demanded such as automotive and aircraft parts.

3xxx series: This alloy series is an improved version of the 1xxx series with manganese addition which provides better strength while maintaining good plastic deformation capability.

4xxx series: Silicon can be present in the microstructure as high as 12wt% as a main alloying element that provides a decrease in the melting point due to the eutectic point at 12wt%Si. Therefore, this alloy series provides good welding and brazing properties.

5xxx series: Magnesium as a main alloying element is generally found below 5% due to maintaining alloy stability when the temperature is elevated. These alloys are good low-temperature properties such as good corrosion resistance makes them attractive for marine applications. However, suffer from stress corrosion cracking at elevated temperatures.

6xxx series: Magnesium silicide (Mg_2Si) coming from primary alloying elements of magnesium and silicon, makes this series age hardening. This series of alloys have relatively lower strength than other age hardening alloys. However, the 6xxx series provides better corrosion resistance along with better plastic deformation capabilities.

7xxx series: Zinc is introduced in between 1 and 8% as a main alloying element. Copper and chromium are frequently preferred in this alloy series. Providing significantly high strength makes this series preferred in structural applications such as airframe structures.

8xxx series: Miscellaneous alloying elements such as are categorized under this alloying series. Fe and Si containing 8011, Ni and Fe containing 8001, Fe and Mn containing 8006, and Li containing 8090 can be given as examples where various properties are demanded [1,13,17,18].

2.1.1.2 Cast alloys

Alloys that are processed by melting and casting are given a four-digit number to categorize cast alloys. The notation by association differentiates the cast alloy from wrought alloys by the dot before the last digit. The series is used as follows; 1xx.x series which is 99% or more Al, 2xx.x series, 4xx.x series, 5xx.x series, and 7xx.x series includes the same major alloying element with the wrought alloy series of the same first digit. The differences are as follows; 3xx.x series which has Si with Cu and/or Mg added, 8xx.x series which tin is a main alloying element, and finally, unlike 6xxx wrought alloy series, 6xx.x series is unused series in cast alloys while other elements are categorized under 9xx.x series [1,13,17,19].

2.1.1.3 Temper designations

A further classification of aluminum alloys is made according to the heat treatability of the alloys. The alloys whose properties, such as mechanical/strength are enhanced by cold working are called non-heat treatable alloys or strain/work-hardened alloys. The temper designation for these alloys is by the letter H [20].

The alloys that strengthen when subjected to heat treatment are called heat treatable alloys or precipitation/age hardening alloys. The 2xxx, 6xxx and 7xxx series of alloys

and 2xx.x, 3xx.x and 7xx.x series of alloys fall below this category. The letter designation for the age hardening alloys is T. The age hardening alloys are subjected to the treatment of solution heat treatment and aging naturally at ordinary temperature or artificially at elevated temperature (100-200°C). The heat treated naturally aged alloys are denoted by T1, T2, T3, T4 while artificially aged alloys are denoted by T5, T6, and T9. O and F letters are used for the annealed condition and as fabricated condition, respectively. The details of T3 and T6 treatment for the commercial alloys are given as follows: 2024-T3- Solution heat treated (at 495°C) and cold worked, 6061-T6 Solution treated (at 530 °C) and aged artificially (at 160 °C) [1,13,20,21].

2.2 Microstructure and physical metallurgy of Al alloys

Aluminum is alloyed with most of metals, but there are only a few metals that have adequate solid solubilities, such as copper, silicon, magnesium, and zinc (The solubilities are presented in **Table 2.1**). Nevertheless, some elements despite having solid solubility less than 1%, provide significant enhancements in the properties of alloys. For example, the introduction of transition metals is proven to provide significant grain refinement in aluminum alloys [1,13,22].

Al in the annealed and pure state, has significantly low strength (yield strength: ~10 MPa). This low strength can be enhanced only by hardening through solute atoms if it desired to use in annealed condition. The criteria for achieving this hardening are listed as follows:

- Solute must have solid solubility at the temperature where annealing performed
- Solute must be present in the solid solution after the heat treatment concluded
- Solute must be inert to the other elements that has capability to form phases that not soluble in the matrix [1,13].

Table 2.1 Candidate alloying elements and maximum solid solubilities at given temperature [1,23]

Element	Temperature (°C)	Max S. Solubility (wt.%)	Max. S. Solubility (at.%)

Cd	649	0.4	0.09
Co	657	<0.02	<0.01
Cu	548	5.65	2.4
Cr	661	0.77	0.4
Ge	424	7.2	2.7
Fe	655	0.05	0.025
Li	600	4.2	16.3
Mg	450	17.4	18.5
Mn	658	1.82	0.9
Ni	640	0.04	0.02
Si	577	1.65	1.59
Ag	566	55.6	23.8
Sn	228	~0.06	~0.01
Ti	665	~1.3	~0.74
V	661	~0.4	~0.21
Zn	443	82.8	66.4
Zr	660.5	0.28	0.08

Aluminum alloys have a complex microstructure and achieve improved properties due to the alloying elements such as Zn and Mg as listed above. However, due to low solubility of these alloying elements, new phases are evolved during thermomechanical treatment or solidification [24]. This evolved phases are mainly intermetallic compounds (IMC) with a size ranging from of nano to micrometers. The heterogeneous structure leads to a significant improvement in the strength of the alloys, but they are detrimental to the corrosion resistance of the alloys. The influence of this secondary phases on the corrosion behavior is discussed in section on the corrosion of aluminum.

2.3 Corrosion of aluminum

Aluminum, when exposed to the atmosphere forms a thin-protective oxide layer that protects the metal from oxidation in many environments. Due to this oxide layer, aluminum is a corrosion resistant material that resists weathering and many acids. Corrosion bases of the aluminum are dissolution of metal as anodic reaction:

$Al \rightarrow Al^{+3} + 3e^-$

and oxygen reduction or hydrogen reduction reaction depending on the acidity of the environment.

$O_2 + 2H_2O + 4e^- \rightarrow 4OH^-$

$2H^+ + 2e^- \rightarrow H_2$

The corrosion of aluminum is dictated by the interaction and thus the reaction of local anodes and cathodes to the matrix. In general, aluminum is considered to be corrosion resistant in slightly aggressive aqueous environments due to the protective oxide layer as a consequence of thermodynamic stability of Al oxides. However, there is not a general consensus about the mechanisms of passive layer breakdown by the influence of chloride ions, but the agreement has been made on adsorption of aggressive anions and thus the initiation of localized attack followed by formation of soluble transitional complexes on the oxide surface [25–27].

2.3.1 Thermodynamic principles

The Pourbaix diagrams are used to demonstrate the thermodynamic aspects of the aluminum corrosion. The diagrams plotted as potential vs pH presents the predominant species and stable phases in the given potential and pH range. The Pourbaix diagram for pure Al is presented in Figure 2.1.

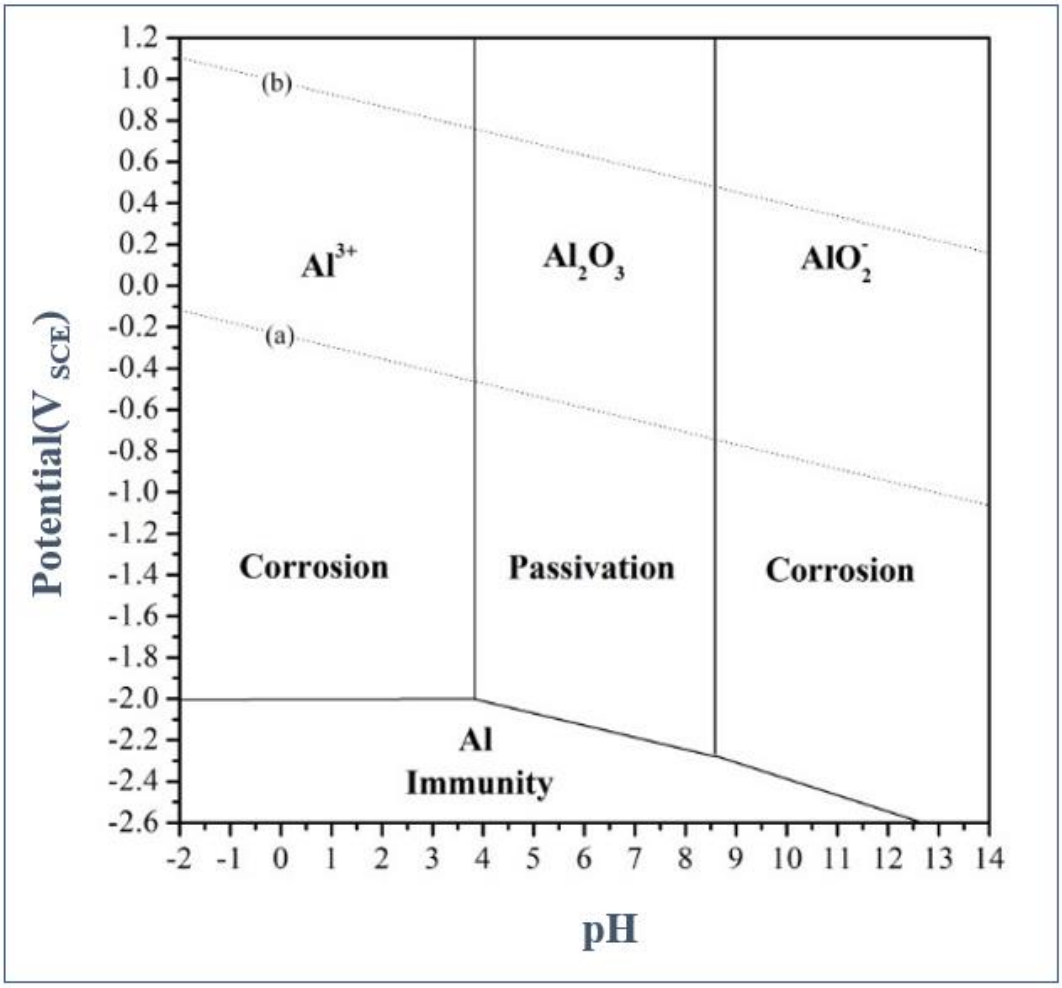

Figure 2.1 Pourbaix diagram for Pure Al, (adapted from [28]) a) line for water stability b) line for decomposed products

Aluminum is passive in the range between 4 and 9 pH thanks to the oxide film. However, the modification in the passive range due to different environments, passive film fails to maintain its stability. Al goes into Al^{+3} state in lower pH zones, while it forms AlO^{2-} in the higher pH zones.

The Pourbaix diagrams are not practical for engineering applications where pure metals are significantly less in demand due to their properties, especially for structural applications. Because this diagrams have certain limitations to be used for the alloys. Pourbaix diagrams do not provide the influences of alloying elements and mainly constructed for pure metals. In addition, the influence of the electrolyte is neglected,

especially the influence of the chlorides. Moreover, the diagrams are constructed for 25 ℃ and the influence of temperature is neglected. Finally, corrosion is a kinetic process and reaction rate information is not found in these diagrams. Therefore, all the parameters should be considered for each alloy on certain condition. **Figure 2.2** exemplifies how the Pourbaix diagram for an alloy (AA 5086) was modified in a 0.5 M of NaCl electrolyte [26].

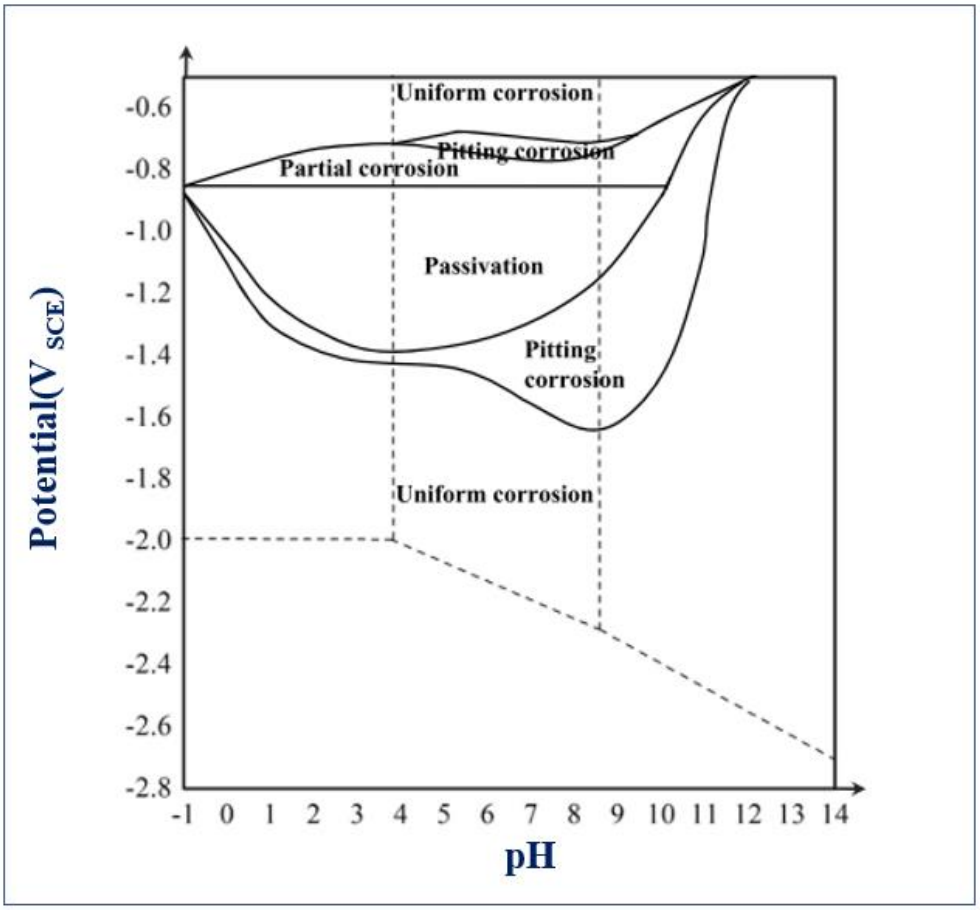

Figure 2.2 Pourbaix diagram for an AA5086 alloy exposed to 0.5 M NaCl electrolyte (adopted from [26])

As it can be seen from **Figure 2.2**, localized corrosion predominates the passivated regions observed in **Figure 2.1**. The Pourbaix diagram still lacks important information about the reaction rate and kinetics of the cathodic and anodic reactions which can be evaluated by anodic and cathodic polarizations [26,29].

2.4 Corrosion of aluminum alloys

The complex microstructure of Al alloys, which has evolved from efforts made to strengthen aluminum alloys, has a significant influence on corrosion performance. The inhomogeneities have different electrochemical nature than the matrix and might be more or less noble, which will determine the character whether anodic or cathodic, respectively. The pitting in aluminum alloys generally believed to be initiated at the interface between these particles and the Al matrix, which are accounted for the breakdown of the passive film. Pitting corrosion is associated with the breakdown of passive film on the alloy surface and thus the loss of film stability. However, Al alloys are affected by the intermetallic particles that are accounted for two types of pit morphologies, namely circumferential pits and selective dissolution of the particles.

The intermetallics are classified into three main categories [30];

Precipitates formed during ageing process that can be in different shapes, ranging from plate-like to spherical. These particles range in size from micrometers to angstroms and affect the corrosion behavior depending on their concentration, whether they are finely distributed in the matrix or concentrated in the grain boundaries, resulting in a tendency to stress corrosion or inter-granular corrosion [31]. Cu, Mg, Li, Zn and Si are the elements responsible for precipitates such as $MgZn_2$, Al_2Cu and Mg_2Al_3 [30].

Constituent particles are generally larger in size and their shapes are more irregular with a size range of reaching approximately 10 micrometers. They might evolve during solidification and might be realigned during thermomechanical treatment. They are mainly attributed to pitting corrosion mainly found in Fe, Si, Mg, Mn containing alloys such as Al_7Cu_2Fe and Al_3Fe [22,30].

Alloying element containing small particles are classified as dispersoid that ranging from 0.5 to 0.05 µm in size. Ti, Zr, Cr, and Mn are generally classified as dispersion formers that forms dispersoids at high temperatures. Common examples can be given as, Al_6Mn, Al_3Zr and Al_3Ti [30,32]

2.4.1 Galvanic interaction when in contact with dissimilar metals

Considering the electrode potential which is revealed in the galvanic effects due to contact of different metals, the experimental data dictate the corrosion resistance of the metal when it is in contact with dissimilar metals. Experimental data provides that the sacrificial attack of aluminum and alloys is expected when they are interacted with many metals through an aggressive media. It must strictly be considered that the galvanic difference provides only limited information, since the actual corrosion current is also determined by polarizations which is affected by electrolyte/metal interface which includes oxides on the surface [1,17,33,34].

2.5 Al Alloys processed by unconventional techniques

Al alloys, considering the environmental aspects associated to energy efficiency and weight reduction, have been attracting significant attention. It is debatable that the Al alloys reached to its theoretical potential on the scope of material properties. Therefore, the research has been continuously made to enhance properties by employing unconventional processing techniques. Al alloys with a yield strength greater than 1 GPa was reported [8] and several research findings have been reporting the property improvement by alloying additions in an increasing trend [4,14,35].

The methods provide dissimilar microstructure and therefore the properties are achieved by unconventional processes. The obtained structure might be amorphous or nanocrystalline, which enables the supersaturation of secondary elements that are not possible to present under equilibrium conditions [35,36].

2.5.1 Methods for microstructure modification

The form of the Al alloys produced by unconventional techniques is reported to be in the form of coatings or thin films produced by sputter deposition [35,37,38], ion implementation [35,38,39] and electrodeposition [35,40,41]. The form of these products are not suitable for structural applications since upscaling the coatings and thin films are not convenient to be used in practical applications [39].

Unconventional techniques that provide bulk Al-alloys are mainly classified as severe plastic deformation such as equal channel angular pressing [42,43], high pressure torsion [4,35,44] and accumulative roll bonding [45]. These techniques provide significant enhancement in the mechanical properties due to grain refinement. Nevertheless, the alloys do not demonstrate enhancement in the solid solubility and therefore the corrosion performance of this alloys are not influenced in a positive manner as much as mechanical properties. However, high energy ball milling is reported to provide significant enhancement in the solute solubility in Al alloys that is promising for enhancement in corrosion performance [9,36,46,47].

2.5.2 High-energy ball milling

High energy ball milling is also termed as mechanical milling or mechanical alloying is a nonequilibrium processing technique. Unconventional techniques aim the high energy state of materials to tailor desired properties by energizing the material. Conventionally, the influence of pressure, temperature, light etc. was employed to energize material. However, use of mechanical forces is much more convenient by severe plastic deformation techniques [48].

Mechanical alloying (high-energy ball milling) was initially designed in the 1960s to develop oxide dispersion strengthened superalloys [49] but the understanding the science behind this technique is initiated at late 80s and still in progress [50].

High energy ball milling statement is generally preferred when the operation does not involve alloying but just milling. The operation involves the combining elemental or pre-alloyed powders in a milling medium together with a process controlling agent (PCA) (optional) to avoid agglomeration and welding. Mechanism of alloying is presented in **Figure 2.3**. The process is a repetitive cold welding followed by fracturing and rewelding that in a continuous operation [40,48,51].

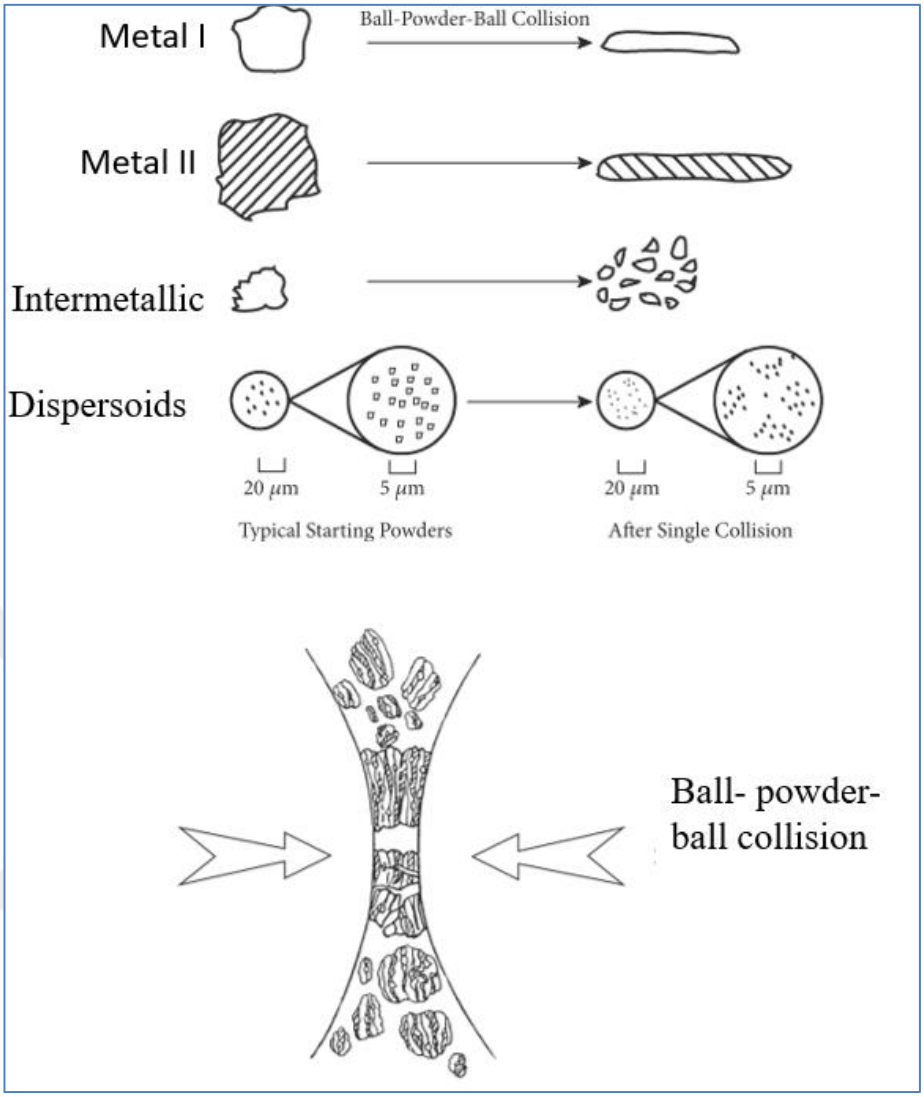

Figure 2.3 Schematical representation of deformation characteristics of high-energy ball milling. Reproduced from [48].

Process can be performed in laboratory scale mills that yields 10 to 20 g per run and in planetary mills than can produce 200 to 500 g at a batch. Attritors, which are the low energy mills, have much more capacity extending 40-50 kg powder per hour [48]. Suryanarayana also reports that the large scale attritors for commercial applications and high-energy mills with a production capacity of 5 tons of powder per hour in Russia [48].

2.6 Corrosion behavior of high energy ball milled Al alloys

Vast majority of the work on high energy ball milled Al alloys has focused on improving the mechanical properties of the alloys. The corrosion investigation of ball milled Al alloys attracted limited attention especially till the last few years. The ability to provide extended solid solubility is a great merit in the scope of corrosion investigation. Moreover, the grain refinement occurs up to the nanoscale, resulting in a nanocrystalline structure that is expected to demonstrate different corrosion behavior than its counterparts [35,38].

Sikora et al. reported the influence of nanocrystalline AA5083 alloy produced by high energy ball milling [52]. Corrosion behavior was reported as significantly different from commercial AA5083 by the parameters of pitting potential, which was slightly noble, and current density together with corrosion potential, which were similar to commercial AA5083. This was mainly attributed to the refinement or dissolution of the secondary phases which are cathodic to the matrix. Kuş et al. reported the corrosion performance of nanocrystalline AA5083 vis a vis commercial AA5083 alloy [53,54]. The electrochemical corrosion investigation gave similar results both in nanocrystalline and conventional alloys. However, immersion tests and surface investigation demonstrated that the pits and the damage were bigger in the nanocrystalline alloys, unlike the work by Sikora et al [52].

Gupta et al. [46] reported significantly improved corrosion performance in the nanocrystalline Al-Cr alloys (in situ consolidated and spark plasma sintered) produced by mechanical alloying and subsequent consolidation with spark plasma sintering where in-situ consolidation is not observed. Gupta et. al attributed superior corrosion performance of the nanocrystalline alloys to mutual presence of supersaturated solid solution and nanocrystalline nature [55].

There are studies that reports a lower corrosion performance in a AA5052 due to grain refinement [35,56]. Influence of grain size on the corrosion of Al alloys indicated that establishing a general theory on this effect is not clear, since there is not absolute consensus about this effect and many other properties are affected by grain refinement

processes [57]. Gupta and Birbilis also advocate a similar approach for the nanocrystalline stainless steels since many aspects such as composition, environment and processing techniques must be considered [58].

Esquivel and Gupta reported the simultaneous increase in strength and corrosion performance of the alloys produced by high energy ball milling [36]. Alloys produced by mechanical alloying of Al-5at% M, where M stands for Mo, Nb, Cr, V, Ni, exhibited nano-scale grain refinement along with extended solute solubility [9]. The hardness and corrosion performance of the alloys produced herein was superior to any Al alloy available in the market. The improved corrosion performance of the alloys is attributed to the following mechanisms such as enrichment of the passive film by solute atoms and consequent increase in passivity [59,60] , tendency to re-passivate by modifications in the critical pit solution [37], release of corrosion inhibiting oxyanions such as chromates or vanadates [61] and the decrease galvanic activity in between secondary phase and the surrounding matrix [9].

Keeping the various influences reported by abovementioned literature in mind, the properties of the Al alloys produced by high energy ball milling might be similar, even worse, or better than those of their counterparts. However, with the help of high energy ball milling, there is a high potential for developing Al alloys with high strength and corrosion resistance. Designing process parameters and selection of alloying elements have a significant influence the aforementioned properties. Therefore, understanding the influences intermetallics under the umbrella of electrochemical features is critical for designing alloys with superior properties.

CHAPTER 3

EXPERIMENTAL

The experimental procedure for material synthesis and characterization tools are explained in this section. Materials and methods for each chapter is discussed individually within the chapter itself. This section contains general information about all the experimental work performed throughout the study.

3.1 Materials

The materials prepared by high energy ball milling of pre-alloyed powder and mechanical alloying of the elemental powder. The raw materials for the commercial alloys are procured as pre-alloyed master alloy powder (Valimet AM2024, AM6061, AM7075) and high energy ball milled. The powders used for mechanical alloying (Al, V, Fe, Zr, Y, La) along with the composition of the alloy powders for commercial alloys are presented in **Table 3.1**.

Table 3.1 Alloy chemical composition used for high energy ball milling

Alloy powder	Concentration (wt.%)								
	Al	**Cu**	**Mg**	**Mn**	**Fe**	**Si**	**Cr**	**Ti**	**Zn**
AA2024	Bal.	3.8-4.9	1.2-1.8	0.3-0.9	0.5 Max	0.5 Max	0.1 Max.	0.15 Max	0.25 Max
AA6061	Bal.	0.15-0.4	0.8-1.2	0.15 Max.	0.7 Max	0.4-0.8	0.04-0.35	0.15 Max	0.25 Max
AA7075	Bal.	1.2-2.0	2.1-2.9	0.30 Max	0.5 Max	0.4 Max	0.18-0.28	0.20 Max	5.1-6.1
Al	99.7	-	-	<0.1	<0.1	<0.1	-	-	-
Fe	-	-			99.9				
La 99.9					<0.1				
Zr 99.9	<0.05	-	<0.1	-	<0.2	<0.1	-	-	-
Y 99.9					<0.04				
V 99.9				<0.1	<0.1				

The raw materials for the mechanical alloying and additives are in the pure powder form. The purity of Al powder was 99.7% and the mesh size was -50/100. The alloying

elements were at least 99.8% pure with a mesh size of ~100. For the process controlling agent (PCA), stearic acid is used with a 1.5% in weight.

3.2 High-Energy Ball Milling

The loading and sealing of the powder to the stainless-steel vials are performed in high purity argon atmosphere where supplied in a glovebox (**Figure 3.1**). All the raw materials are loaded and prepared for milling within the glovebox except for the operation performed in Chapter 5 which the influence of milling atmosphere is investigated therein.

Figure 3.1 Powder loading in the glovebox

3.2.1 Milling parameters

For high energy ball milling, stainless-steel media is used (stainless-steel balls and vials). The ball to powder weight ratio is kept constant at 16:1 and 25 g of powder is loaded for each operation. Each spherical ball is in 4 g of weight with a diameter of 1 cm. After loading and sealing, the vials are placed in Fritsch Pulverisette 7 (**Figure 3.2**) planetary ball mill. The milling is performed for 100 hours, and the rotation speed was kept at 280 rpm. The process is interrupted for 1-hour cycles to avoid possible high temperature effects due to constant friction. The status of the operation is checked

in every quartet of the operation. For this purpose, vials are removed and opened in the glovebox to monitor the situation if there is any cold welding and/or agglomeration.

Figure 3.2 Fritsch Pulverisette 7- High-energy ball mill

3.3 Consolidation

Powder obtained after operation is consolidated via cold compaction. The cold compaction is performed in an auto-pellet press using a die made of tungsten carbide with a diameter of 7 mm. The 21400 kg of load is applied to yield 3 GPa of pressure with multiple steps. The operation is started with application of 1000 kg and gradually increased by 2000 kg at each step and hold half a minutes at the applied force. Overall, the pressure application took 4 to 5 minutes to reach the 3 GPa.

3.4 Characterization of the microstructure

3.4.1 Scanning electron microscopy (SEM) and Energy dispersive X-ray Spectroscopy (EDS)

At first, the microstructure of the powder and the consolidated samples were investigated to analyze microstructural features in a relatively fast characterization techniques such as SEM, EDS and XRD. SEM can provide a nano-scale resolution depending on the sample and instrument conditions. Both secondary electron (SE) and back-scattered electron modes which provides information about surface and chemical

nature of the alloy are operated. The specimens for the SEM investigation are prepared by grinding until 1200 grit surface finish. Then the polishing is carried out until 0.05 µm surface finish under running ethanol. Specimens are rinsed and dried in air after ultrasonic cleaning in a bath of ethanol for 5 minutes. SEM performed in FEI Verios 460 L-FESEM (Figure 3.3) equipped with an Oxford energy dispersive spectrometer (EDS).

Figure 3.3 FEI Verios 460L Field Emitted Scanning Electron Microscopy

3.4.2 XRD

X-ray diffraction provides information about the phases, crystallite size and lattice strain in a relatively faster amount of time as compared to burdens of specimen preparation for TEM.

The XRD investigation is carried out in a Rigaku Smartlab diffractometer (Figure 3.4). The diffractometer is equipped with graphite monochromator and the Cu Ka radiation is used for the investigation on the Bragg-Brantano setup.

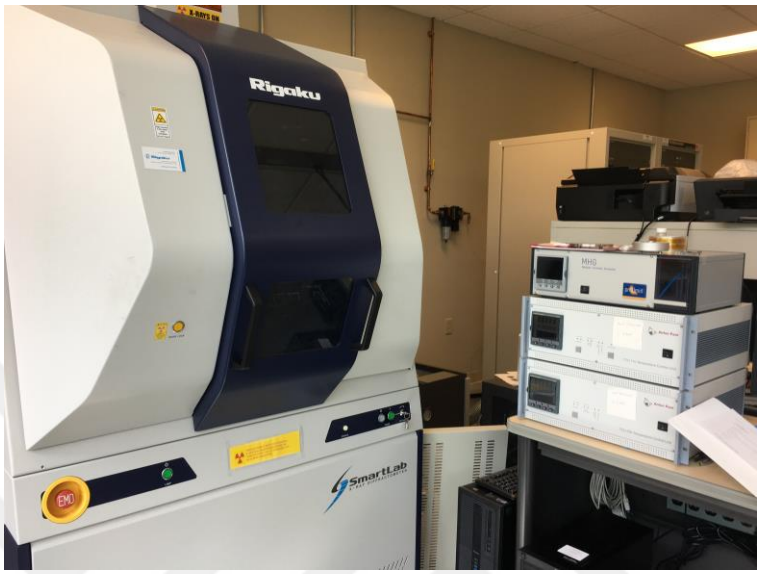

Figure 3.4 Rigaku Smartlab Diffractometer

The contribution due to instrumental broadening is determined by LaB_6 standard sample. The grain size and lattice strain are calculated by Rietveld refinement and Scherrer's equation where Rietveld pattern fitting was not possible due to low R^2 score. The pattern fitting is performed in Panalytical Xpert Highscore plus software. The grain size calculated by Scherrer's equation is as follows:

$$\text{Crystallite size} = \frac{K\lambda}{\beta \cos\theta} \qquad (3.1)$$

Where λ is the wavelength (1.54056 Å), β is the broadening at fully with half maximum after eliminating the instrumental broadening and θ is the diffraction angle. The scan step and speed are kept at 0.01 and 1°/min, respectively. The scan range is specified in each chapter according to the alloy constituents.

XRD also employed to determine the solid solubility of the solute atoms in the case of binary alloys since the change in the lattice parameter which was calculated by Bragg's

law, is attributed to presence of alloying elements in the solution referencing the experimentally determined values of solid solubility changes in binary Al alloys [62].

3.4.3 Focused Ion Beam

Focused ion beam (FIB) is a technique that has been in use since early 1980s. This technology has been increasing its capacity with the advancement in ion milling and micro-manipulation techniques. FIB enables local milling, local material deposition in a high precise manner. Also, it enables fast and efficient preparation of samples for transmission electron microscopy investigation and thin film manipulation. There are also studies that reporting the micromachining of devices such as MEMS through FIB [63].

A ThermoFisher Quante 3d FEG FIB-SEM (Figure 3.5) was employed for TEM sample preparation in the present work. Specimens were protected with platinum coating to avoid surface damage due to ion beam milling before the milling operation. A landing voltage of 30 kV with various beams currents was utilized to monitor the specimen to avoid damage due to ion beam. Cross section lift-out with an approximate thickness of 1–2 µm of lamella was performed by an omniprobe manipulator. Further thinning of the sample and contamination cleaning was carried out after placing the lamella on a TEM grid.

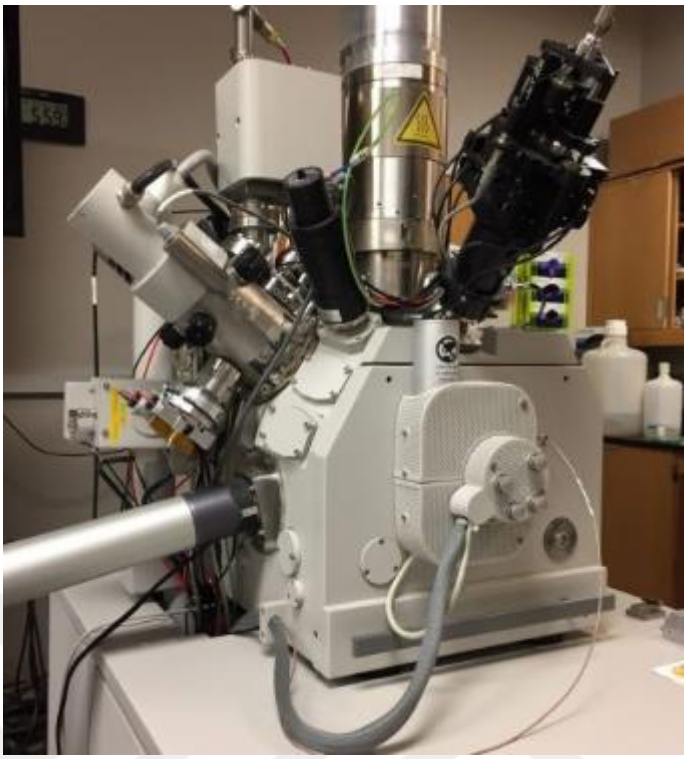

Figure 3.5 The ThermoFisher Quanta 3D FEG FIB-SEM instrument

3.4.4 Transmission electron Microscopy (TEM)

Microstructure and also passive film properties is further investigated by a Thermofisher Talos F200X Field Emission Gun Scanning Transmission Electron Microscope (Figure 3.6) operated at 200 kV. Both bright field which provides more magnification opportunity to show nano scale features in the microstructure and dark field image which provides more contrast that will provide the grain size determination more precisely. Selected are diffraction (SAED) pattern also provides information about the crystal structure of the alloys. Therefore, the correlation in between the XRD and TEM data can be established to evaluate the quality of the data.

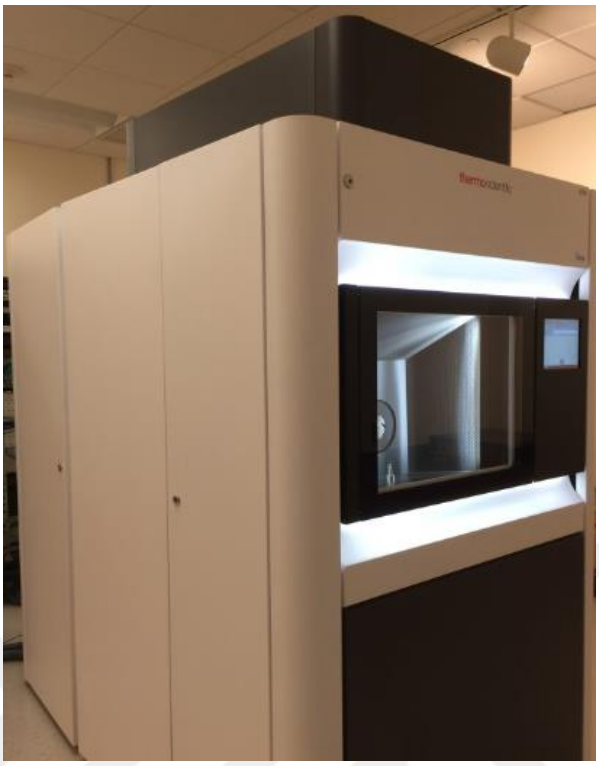

Figure 3.6 Talos F200X G2

3.5 Corrosion investigation

3.5.1 Electrochemical corrosion tests

Electrochemical corrosion investigation was carried out to assess fast and versatile results about the corrosion performance of the alloys. For this purpose, cyclic potentiodynamic polarization (CPP), anodic and cathodic polarizations, potentiostatic (PSP) polarizations and open current potential (OCP) measurements were carried out in a BioLogic VMP-300 (Figure 3.7) multichannel potentiostat controlled by EC- Lab software. The conditions of the experiments are discussed specific to each chapter.

Figure 3.7 BioLogic VMP-300 Multichannel Potentiostat (Image obtained from [64].)

Experimental parameters are stated in each chapter's experimental section. Three electrode cell setup was used for the experiments where specimens are working electrode, a platinum mesh is counter electrode and saturated calomel as reference electrode. A schematical representation for the three-electrode cell is presented in the image Figure 3.8.

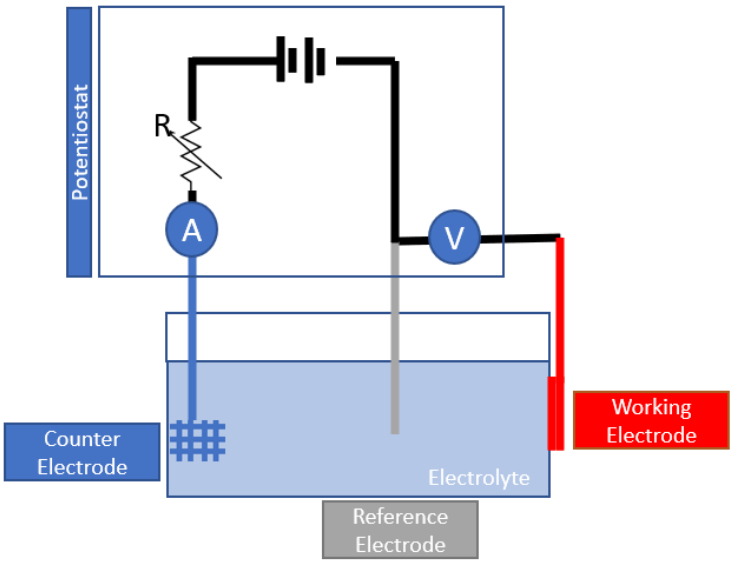

Figure 3.8 Schematical representation of the three-electrode cell

3.5.2 Immersion tests

Immersion tests were carried out to investigate the corrosion resistance and evaluate the correlation with electrochemical corrosion test. The specimen surface preparation was conducted, and specimens were immersed in NaCl solutions ranging from 0.1 M to 0.6 M. In order to investigate the corrosion initiation, specimens immersed for short times like 1 to 2 hours. Prolonged immersions like 1 week and 2 weeks immersions are also performed to investigate long term effect of exposure. In order to evaluate surface features of the alloys, the corrosion products were removed by dilute HNO_3 (30 vol%) cleaning (1 min) after the immersion in some cases which are specified in each chapter.

3.6 Characterization of surface

Surface characterization is critical for understanding and proposing corrosion mechanisms. Surface of the alloys were investigated to identify the structure and species that formed after exposure on the surface.

3.6.1 X-ray photoelectron spectroscopy (XPS)

X-ray photoelectron spectroscopy provide information about the chemical species their composition and oxidation state on the surface in a qualitative manner. The sample surface is prepared as the procedure described in specimen preparation for SEM. First, air formed passive layer investigated. Then, the passive layer developed after 2 hours of immersion is investigated. The experimental parameters are given in each chapter. The prepared samples are analyzed within 24 hours after surface preparation and kept in the high purity argon atmosphere. The oxide film investigation was conducted on 2x2 mm scan area with a 60˚ take-off angle. Instrument (SPECS system with PHOIBOS 150 Analyzer, Figure 3.9) chamber pressure was kept below 10-9 mbar and Mg anode was used as the X-Ray source of 300 W. CASA software was utilized for the analysis of XPS data and the background was eliminated using the Shirley function.

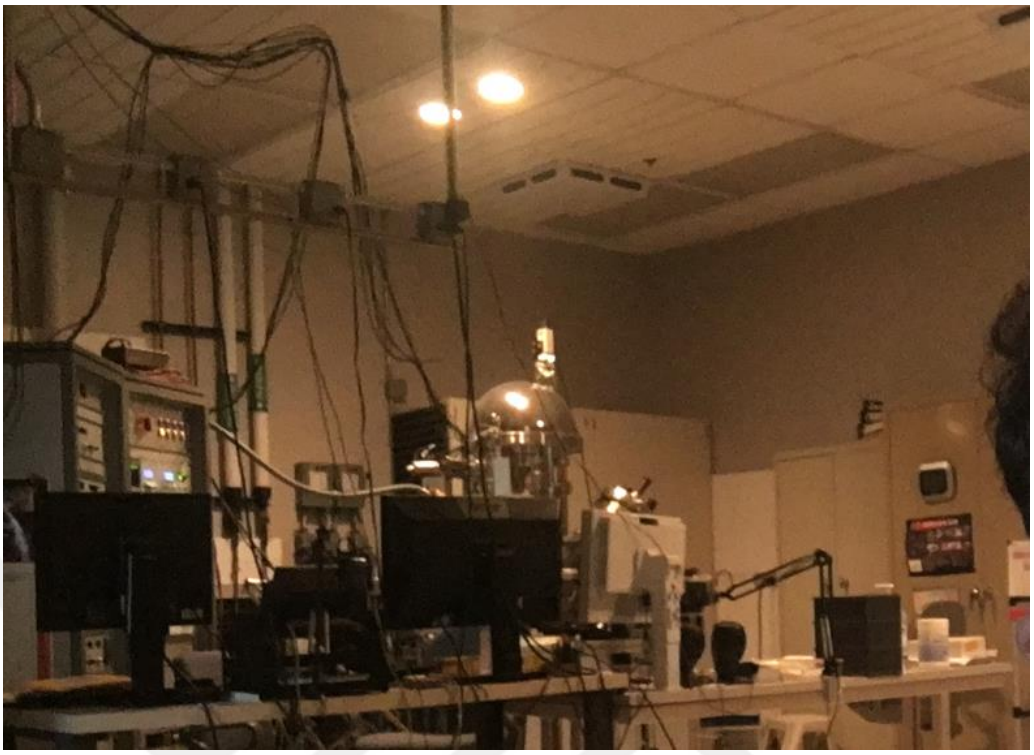

Figure 3.9 SPECS system with PHOIBOS 150 Analyzer

3.6.2 Time-of-Flight Secondary Ion Mass Spectrometer

Secondary ions mass spectrometer (SIMS) is a surface analytical technique that bombards the surface by an ion beam. Secondary ions enable to detect species within a depth profile. Time-of-flight secondary ion mass spectroscopy (ToF-SIMS) was performed in ION-TOF-TOF SIMS[5] (Figure 3.10) to obtain elemental depth profiling on Al-5at%Fe 2hr immersed specimen in 0.1M NaCl solution. Sample preparation steps are kept as same as XPS and SEM sample preparation. The pressure of the main chamber inside the instrument was maintained below 10-9 mbar. Primary ion source of Bi3+ with 25keV and 0.35 pA target current was rastered over 100 x 100 µm area. Cs+ ion beam was used to sputter the surface with 1 keV and 7.2 nA current over 150 x 150 µm area.

Figure 3.10 ION-TOF TOF-SIMS[5]

3.6.3 Surface profilometry

Surface profilometry was performed on a Keyence VKx1100- confocal laser scanning microscope. The samples immersed for different durations were subjected to investigation after surface cleaning. The samples were partially masked with a PTFE tape to create a reference surface for the analysis.

3.7 Hardness

Vickers hardness of the alloys was obtained using a Mutitoyo hardness tester with a 100 g applied load and 10 s of dwelling time. The hardness tests were carried out at least 10 times to calculate average Vickers hardness.

CHAPTER 4

RESEARCH OBJECTIVES & METHODOLOGY

The present work has a broad objective of development and characterization of nanocrystalline aluminum alloys from both engineering and scientific aspects. The engineering aspects focus on filling the gap in producing Al alloys with unconventional techniques. The high-energy ball milling has been reported to provide Al alloy powder that can be consolidated into bulk materials unlike other non-equilibrium techniques. The high-energy ball milling process is not fully understood and promises development of high-strength and corrosion resistant alloys with adequate control of process parameters. The end products being in the form of powder enables its usage in many processing techniques ranging from conventional press and sintering to advanced manufacturing methods.

The scientific aspects mainly focused on proposing the mechanisms that provide superior corrosion resistance and explaining the corrosion behavior. There is no absolute consensus in the literature yet when it comes to supersaturated alloy systems and there is still a remarkable gap in the understanding the corrosion of supersaturated alloys of Al with many combinations since the mechanisms are different in each alloy systems. Therefore, the understanding of the corrosion behavior, especially the Al-Fe system will enable designing novel Al alloys with superior properties.

In order to achieve the main objective of the present work, the paths including the specific objectives are as follows:

1) Processing of commercial age-hardening Al alloys to prepare nanocrystalline alloys of same compositions.

2) Understanding the mechanisms of strength and individual contributions.

3) Tailoring the milling atmosphere to produce an aluminum alloy selected from first step.

4) Tailoring the composition by introduction of V and $CeNO_3$ to a nanocrystalline Al alloys selected from previous step (AA2024).

5) Synthesizing of binary Al alloys by mechanical alloying of Al and Y,Zr,La and Fe.

6) Understanding the mechanism of corrosion in nanocrystalline Al-Fe alloy synthesized in previous step.

This study follows a top-down like approach to develop and characterize nanocrystalline alloys. The nanocrystalline age-hardening commercial alloys is aimed at first to understand the processing response of multi-element containing alloys such as AA2024, AA6061 and AA7075. To the best of author's knowledge, this will be the first work on comparison of corrosion and hardness of age-hardening commercial aluminum alloys where their strength is increased by thermo-mechanical and age hardening treatments. The findings of this part will not only be beneficial to the rest of the study but also will be beneficial itself for both scientific and industrial communities.

AA2024 which has a complex microstructure selected and influence of milling atmosphere on the alloy properties aimed to investigate. Investigation of milling under air atmosphere promise significant gains if it is succeeded. Therefore, successful accomplishment of the high-energy ball milling in air might be beneficial to improve the performance of the Al alloys due to the possible incorporation of oxides or dispersoids. However, the influence of air on the ball milled Al alloys is not known and warrants research attention. The objective for this part is to fill the gap in the research. The modified structure is aimed to demonstrate improved corrosion and hardness along with better thermal stability that will be critical for possible additive manufacturing applications.

The effects of compositional modification on the nanocrystalline AA2024 was aimed to investigate by $CeNO_3$ and V addition. Ce inhibitors has been reported to provide efficiently suppressing the dissolutions. In addition, the research on the nanocrystalline

Al alloys reports the positive influences of vanadium in binary Al-V alloys produced by high energy ball milling. V is reported to provide enhanced corrosion resistance by suppressing cathodic activity of particles. However, role of V is not known for a complex alloy where its microstructure is dominated by cathodic particles. Therefore, the AA2024 alloy that investigated in previous chapters is modified with V and $CeNO_3$ addition.

Finally, the last objective is to synthesize binary Al alloys by mechanical alloying to fill the research gap on binary Al alloys. Four elements have been selected as alloying elements. Considering the performance of rare earth inhibitors, two rare earth elements such as La and Y has been selected. Two transition metal elements such as Fe and Zr which have not been reported in the reviewed literature have been selected. Experimental findings along with engineering importance made Al-Fe alloys to be selected for further investigation. Furthermore, Fe is a residue and undesired elements in almost all Al alloys. The presence of Fe is due to from ore itself or from thermomechanical treatments. In addition, Fe is a limiting factor in many applications that demands Al alloys. For this reason, recycled Al alloys where Fe content accumulates after each processing step is not preferred in many applications. The outstanding properties obtained from Al-Fe nanocrystalline alloy warrant significant research attention and therefore investigation through electrochemical tests along with characterization of passive film structure is aimed to understand and propose the mechanisms.

CHAPTER 5

CORROSION BEHAVIOUR OF AGE HARDENING ALUMINUM ALLOYS PRODUCED BY HIGH ENERGY BALL MILLING VIS-À-VIS COMMERCIAL AGE HARDENING ALUMINUM ALLOYS

5.1 Abstract

The influence of high energy-ball milling (HEBM) on corrosion and hardness of age hardening aluminum alloys was investigated. Nanocrystalline age hardening (AA2024, AA6061 and AA7075) alloys were produced by HEBM of pre-alloyed powder and subsequent cold compaction under uniaxial pressure of 3 GPa. Cyclic potentiodynamic polarization and immersion tests were conducted in 0.6 M NaCl solution which revealed significantly increased pitting and protection potentials in the HEBM alloys compared to wrought alloys of same composition. X-ray diffraction and TEM analysis indicated grain refinement below 100 nm in the ball milled alloys which was the major strengthening mechanism in the age hardening HEBM alloys. The superior corrosion resistance and hardness of the age hardening ball milled alloys were attributed to nanocrystalline structure, extended solid solubility and homogenous microstructure- free from coarse intermetallic phases.

This chapter is partially reproduced from [65] with the license from Elsevier (See appendix).

5.2 Introduction

Aluminum is an active metal and yet corrosion resistant in the pure form due to presence of a protective oxide film (alumina) on the surface [1]. However, most of aluminum alloys exhibit poor corrosion performance owing to the microstructural heterogonies which lead to micro-galvanic interaction [13]. 2xxx, 6xxx and 7xxx series of commercial aluminum alloys are strengthened by age hardening where the

strength and corrosion performance depend upon the composition, crystal structure, size, shape, and distribution of the precipitates [66–68]. The complex microstructures in age hardening alloys incorporate secondary phases comprising of Cu, Zn, Mg, Si as primary alloying elements and Fe, Cr, Ti, Mn as impurities or secondary additives [31]. Secondary phases in aluminum alloys are classified into three main categories; constituent particles, precipitates and dispersoids, which develop during solidification and thermomechanical treatment to obtain desired mechanical properties [30,31]. The effects of secondary phases on the localized corrosion in age hardening aluminum alloys have been widely reported [30,66,69–74].

Localized corrosion in the age hardening aluminum alloys depends on chemical composition, size and spatial distribution of the secondary phases occurred during metal forming and subsequent thermo-mechanical processing. Electrochemical nature of the secondary phases, depending on the composition, could be anodic or cathodic with respect to the matrix. Relatively noble particles like Al_2Cu, AlFeMnSi, AlCuFeSi, AlCuFeMn can act as local cathodes that cause the dissolution of adjacent matrix leading to the pitting corrosion [32,69,70,72,75–80]. Active particles like MgZn2, Mg2Al3 and Mg2Si act as local anodes that cause self-dissolution and forms pits [32,69,70,72,75–77,79–84]. Localized corrosion as well as formation of secondary phases depend upon the initial microstructure, including grain size of the alloys. Physical breakdown of secondary phases and increased passivation ability via grain refinement is attributed to enhanced corrosion resistance [52,85]. On contrary, some studies claim an inverse relationship with grain refinement and corrosion resistance [86]. Microstructure and therefore corrosion of an alloy is highly dependent on the production and post-production processes. Approximately 75 to 80 % of the total aluminum products are comprised of wrought aluminum alloys which are produced from homogenized cast ingots via forging, rolling or extrusion where the secondary phases are broken and dispersed within the alloy during the metal forming processes [1,26]. Moreover, the characteristics of the phases formed during age hardening treatment in the age hardenable alloys dictate the hardness and corrosion resistance [87,88].

The methods providing modified microstructures such as melt spinning, ion implantation, sputter deposition, electrodeposition and mechanical alloying are elicited the remarkable modifications in the mechanical performance and localized corrosion resistance in metastable alloys [38]. Recent literature on Al-Mg alloys showed improvement in the mechanical performance by severe plastic deformation, extrusion and additive manufacturing methods [89–97]. High-energy ball milling (HEBM) is a technique to impart high strength by grain refinement, uniform dispersion of fine ceramic particles and extended solid solubility [98,99]. HEBM in combination with suitable alloying elements has also been reported to corrosion performance of aluminum alloys and the underlying mechanisms are discussed in [6,7,38,100]. Coarse secondary phases are either dissolved or extensively refined during the HEBM [6,39,54,101–104]. Additionally, milling enhances diffusion of the alloying elements and defect concentrations which influences the precipitation [6,105]. Therefore, microstructural evolution and properties of the high-energy ball milled alloys during thermomechanical processing and in service are expected to be different than the commercial alloys of the same chemical composition. [6,103,106,107]. For example; modified grain boundary segregation of Mg in nanocrystalline Al-Mg alloys was observed [44,90]. Moreover, intergranular corrosion (IGC) and stress corrosion cracking (SCC) caused by the precipitation of intermetallic (Mg_2Al_3, when exposed to 50 to 200^{o}C in Al-Mg alloys with more than 3.5 wt.% Mg) can be influenced by the increased diffusivity of Mg as a result of HEBM [6,108,109]. Furthermore, hydrogen embrittlement may also be influenced by the possible enhancement of H diffusivity in Al alloys [6].

Corrosion behavior of commercial Al alloys produced by HEBM of pre-alloyed powder is reported only in a few studies [54,102,110]. Furthermore, the corrosion behavior of age hardening alloys such as 2024, 6061 and 7075 produced by high energy ball milling is not reported in the literature. Therefore, investigation of the corrosion behavior of age hardening nanocrystalline Al alloys such a great merit. In the present study, the hardness and corrosion behavior of AA2024, AA6061 and AA7075 alloys produced by cold compaction posterior to HEBM of pre-alloyed

powder have been investigated. The results were compared with commercially available wrought AA2024-T3, AA6061-T6 and AA7075-T6 alloys.

5.3 Materials and Methods

Gas atomized powders (Commercially available from Valimet, -325 mesh) of AA2024, AA6061 and AA7075 were high energy ball milled in a planetary ball mill (Fritsch Pulverisette 5) for 100 hours at a speed of 280 rpm. The ball to powder weight ratio was selected as 16:1 for 10 mm diameter stainless-steel balls. Stearic acid (1.5 wt.%) was used as process controlling agent to avoid cold welding. The powder loading and sealing of the jars were done in a glove box with high purity argon atmosphere (O_2 < 50 ppm). The HEBM was interrupted for 1 hour after each hour of milling to minimize the overheating. The obtained powders were consolidated under the load of 11840 kg on a 7 mm diameter tungsten carbide die encased in steel core. Consolidation was conducted in ambient laboratory temperature using a dwell time of 10 minutes for each sample. The alloys produced by HEBM and subsequent cold compaction have been termed as HEBM-2024, HEBM-6061, and HEBM-7075 in this study.

Wrought alloys were also investigated to compare the properties. 3 mm thick wrought alloy plates of AA2024-T3, AA6061-T6 and AA7075-T6 (McMaster-Carr) were procured and machined into 12 mm x12 mm coupons. The chemical composition of the as received gas atomized powders, high-energy ball milled and cold compacted samples, and wrought alloys are presented in Table 5.1.

Table 5.1 Composition of the alloys used herein. Composition of the wrought alloys (AA2024-T3, AA6061-T6, AA7075-T6) was provided by the supplier (McMaster Carr). Composition of the as received alloy powder (AA2024, AA6061, and AA7075) was provided by the supplier (Valimet). Composition of the ball milled and subsequently cold compacted alloys (HEBM-2024, HEBM-6061, and HEBM-7075) was determined using EDS area maps.

Alloy	**Concentration (wt.%)**								
	Al	**Cu**	**Mg**	**Mn**	**Fe**	**Si**	**Cr**	**Ti**	**Zn**
AA2024-T3	Bal.	3.8-4.9	1.2-1.8	0.3-0.9	0-0.5	0-0.5	0-0.1	0-0.15	0-0.25
AA6061-T6	Bal.	0.05-0.4	0.8-1.2	0-0.15	0-0.7	0.4-0.8	0.4-0.8	0.0.15	0-0.25
AA7075-T6	Bal.	1.2-2	2.1-2.9	0-0.3	0-0.5	0-0.4	0.18-0.29	0-0.2	5.1-6.1
AA2024	Bal.	3.8-4.9	1.2-1.8	0.3-0.9	0.5 Max	0.5 Max	0.1 Max.	0.15 Max	0.25 Max
AA6061	Bal.	0.15-0.4	0.8-1.2	0.15 Max.	0.7 Max	0.4-0.8	0.04-0.35	0.15 Max	0.25 Max
AA7075	Bal.	1.2-2.0	2.1-2.9	0.30 Max	0.5 Max	0.4 Max	0.18-0.28	0.20 Max	5.1-6.1
HEBM-2024	Bal.	4.35	1.61	0.30	0.36	0.30	0.1	0.1	-
HEBM-6061	Bal.	0.41	1.20	0.15	0.65	0.82	0.25	0.1	-
HEBM-7075	Bal.	1.85	2.84	0.2	0.45	0.22	0.2	0.1	5.78

5.3.1 X-Ray Diffraction

The x-ray diffraction experiments were conducted in the Rigaku SmartLab equipped with graphite monochromator and Cu Kα radiation (λ=0.154056 nm) with a step size of 0.01° at a scanning speed of 1°/min within the range of 25° to 85°. The mean crystallite size and lattice strain were calculated by Rietveld method [47,48] after determining the contribution of instrumental broadening using LaB6 standard.

5.3.2 Hardness Test

Vickers hardness of the alloys was collected using a Wilson-Tukon hardness tester by applying of 50 g load for 10 seconds. The alloys were ground to 1200 grit SiC paper

finish and ultrasonicated in ethanol. The hardness tests were repeated at least 10 times for each sample to calculate average Vickers hardness.

5.3.3 Electrochemical tests

Electrochemical tests were conducted using a conventional three-electrode flat-cell. Cyclic potentiodynamic polarization (CPP) were performed in 0.6 M NaCl. The copper tape was attached to back of the samples, which were cold mounted into epoxy resin. The samples were ground up to 1200 SiC grit under ethanol following 800, 600 and 400 under running water. The interface between the metal and epoxy was covered with quick set epoxy resin (Araldite) to avoid possible crevice corrosion. The samples were stored in a fume box for 24 hours after application of epoxy.

A multichannel potentiostat (Biologic VMP-300) with EC-lab software was used for the electrochemical tests. Samples were the working electrodes. A platinum mesh was used as the counter electrode and the reference electrode was a saturated calomel electrode (SCE). The open circuit potential (OCP) was measured 0.5 h in order to obtain stabilized electrodes. The CPP curves were obtained with a scan rate 1 mV/s from 0.1 VSCE below the corrosion potential (E_{corr}) until the current density reached 1 mA/cm2 at which point the direction of scan was then reversed thereafter. Potentiostatic polarization curves were obtained by applying a constant anodic potential (150 mV above open current potential) in 0.6 M of NaCl solution. The potentiostatic polarization tests were initiated after stabilization of open circuit potential for 30 minutes.

5.3.4 Scanning Electron Microscopy (SEM) and Transmission Electron Microscopy (TEM) Characterization

Samples were brought to 0.05 µm surface finish using diamond suspension and cleaned in ultrasonic ethanol bath for 5 minutes before SEM analysis. The SEM studies were performed in a FEI Verios 460L field emission SEM with an Oxford energy dispersive X-ray spectrometer (EDS) with an electron landing energy of 20 kV.

Specimen for TEM investigation was prepared in a ThermoFisher Quanta 3D FEG, a Focused Ion Beam and Scanning Electron Dual-beam Microscope (FIB-SEM). Specimen was protected with platinum deposition to avoid surface damage due to ion beam. 30 kV of landing voltage with different beam currents was utilized to monitor the specimen with minimum ion beam damage. In-situ lift-out of the cross section with an approximate thickness of 1-2 μm of lamella was carried out with an omniprobe manipulator. This lamella was placed on a TEM grid for further thinning and cleaning from Ga contamination (Figure 5.1). TEM specimen (HEBM-2024) was kept under vacuum after final polishing until TEM investigation for sub-surface morphology investigation in a Thermofisher Talos F200X Field Emission Gun Scanning Transmission Electron Microscope (S/TEM) operated at 200 kV.

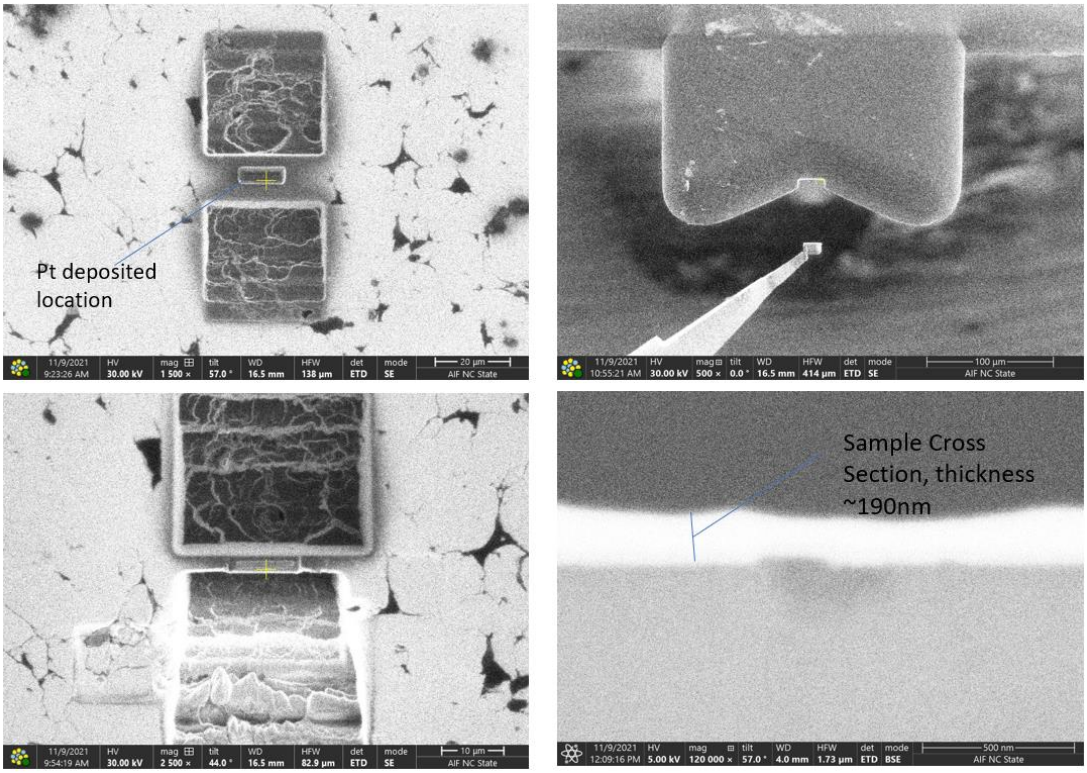

Figure 5.1 TEM sample preparation steps, performed in FIB

5.4 Results and Discussion

5.4.1 Microstructural characterization

Representative backscattered electron image (BSE) of the high energy ball milled powders of alloy 2024, 6061, 7075 and corresponding particle size distribution are shown in Figure 5.2. The mean particle size of the HEBM-2024 powder, HEBM-6061 powder and HEBM-7075 powder was measured as 13.63 (±6.7) µm, 34.65 (±13.34) µm and 9.77 (±6.54) µm respectively. The ball milled powder were produced by the HEBM of gas atomized powder. Gas atomization is the process of breaking molten metal with a high-speed inert gas stream that provides rapid solidification of the droplets. In aluminum alloys, shape of the gas atomized powder particles is primarily spherical [111]. The 320-mesh gas atomized powders were spherical prior to milling while high energy ball milled powders were more irregularly shaped. The irregularity in the size and variation in the particle size are of the alloys can be attributed to the repetitive welding, fracture and re-welding phenomenon during HEBM [112].

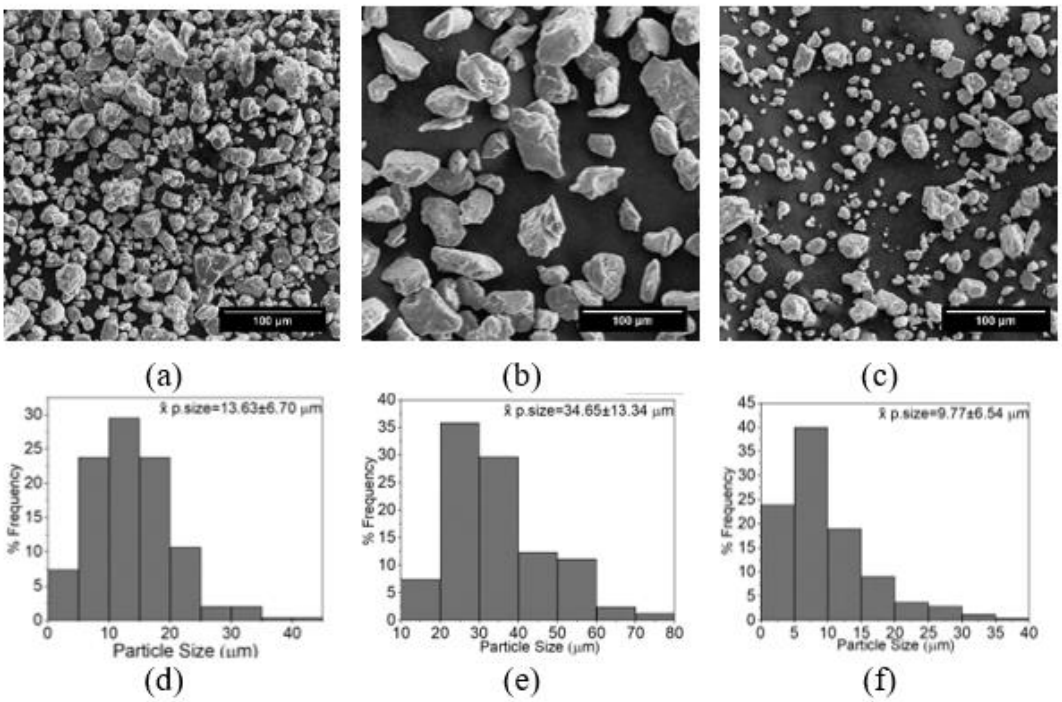

Figure 5.2 Back scattered electron images for (a) HEBM-2024 powder, (b) HEBM-6061 powder, (c) HEBM-7075 powder. Distribution of the particle size for (d) HEBM-2024 powder, (e) HEBM-6061 powder, and (f)HEBM-7075 powder.

Figure 2 shows the BSE images of the ball milled and subsequently consolidated alloys (HEBM-2024, HEBM-6061, HEBM-7075) and wrought alloys (AA2024-T3, AA6061-T6 and AA7075-T6). The HEBM alloys, presented in Figure 5.3, indicated a homogenous microstructure, free from coarse intermetallics that were detected in the wrought alloys (Figure 5.3). The microstructure of the HEBM alloys demonstrated porosity on the surface which is inherent to the cold compaction process and can be attributed to the highly hardened and irregularly shaped particles. Coarse intermetallic particles were observed in the wrought alloys and EDS analysis indicated presence of mainly Al_2CuMg and AlFeMnMg in AA2024-T3; Mg_2Si and AlFeSi in AA6061-T6, Mg_2Si and Al_7Cu_2Fe compounds in AA7075-T6. BSE images of HEBM alloys indicated matrix with uniformly distributed fine bright particles (below 200 nm) and dark particles (below 80 nm) in each case. EDS analysis indicated that the bright particles contain Fe and Cr, and therefore can be attributed to the abrasion of stainless

steel which is the material of milling media. The dark particles could be considered as pores or oxides or nitrides that might be incorporated from the milling atmosphere or stearic acid which was used as process controlling agent (PCA). Use of PCA might not be very attractive for HEBM due to the possible decomposition and therefore contamination during the process [113]. However, characteristics of the ball milled powder such as the shape, size, purity, chemical and thermal stability are highly dependent to the type and amount of PCA [114].

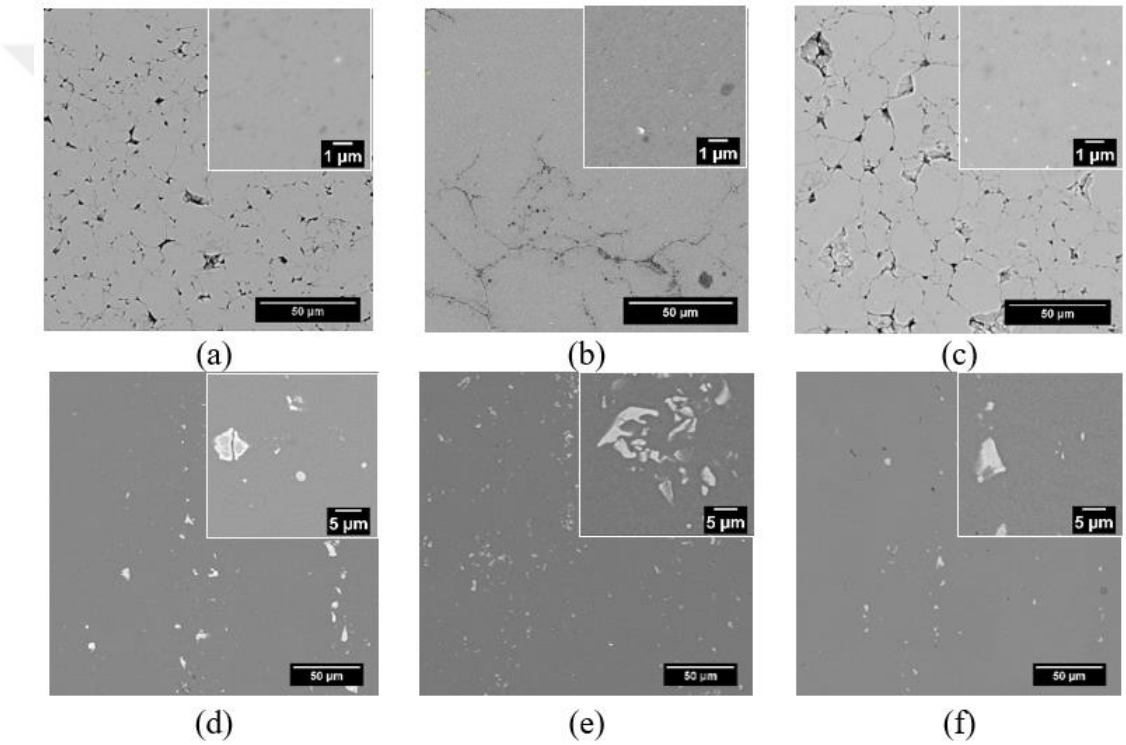

Figure 5.3 Back scattered electron images for (a) HEBM-2024, (b) HEBM-6061, (c) HEBM-7075, (d) AA2024-T3, (e) AA6061-T6 and (f) AA7075-T6. Corresponding high magnification images are shown in the inset.

X-ray diffraction (XRD) patterns for both HEBM and wrought alloys are presented in Figure 5.4. XRD spectra of all alloys was mainly comprised of Al peaks. When compared to wrought alloys, all HEBM alloys demonstrated significant peak broadening which is the indicator of grain refinement. The peak broadening of the Al

peaks (considering the contribution of instrumental broadening) was employed to calculate the grain size and lattice strain via Rietveld method [115]. The grain size of the HEBM-2024, HEBM-6061, HEBM-7075 were calculated respectively as 29 (±5) nm, 38 (±6) nm and 28 (±4) nm.

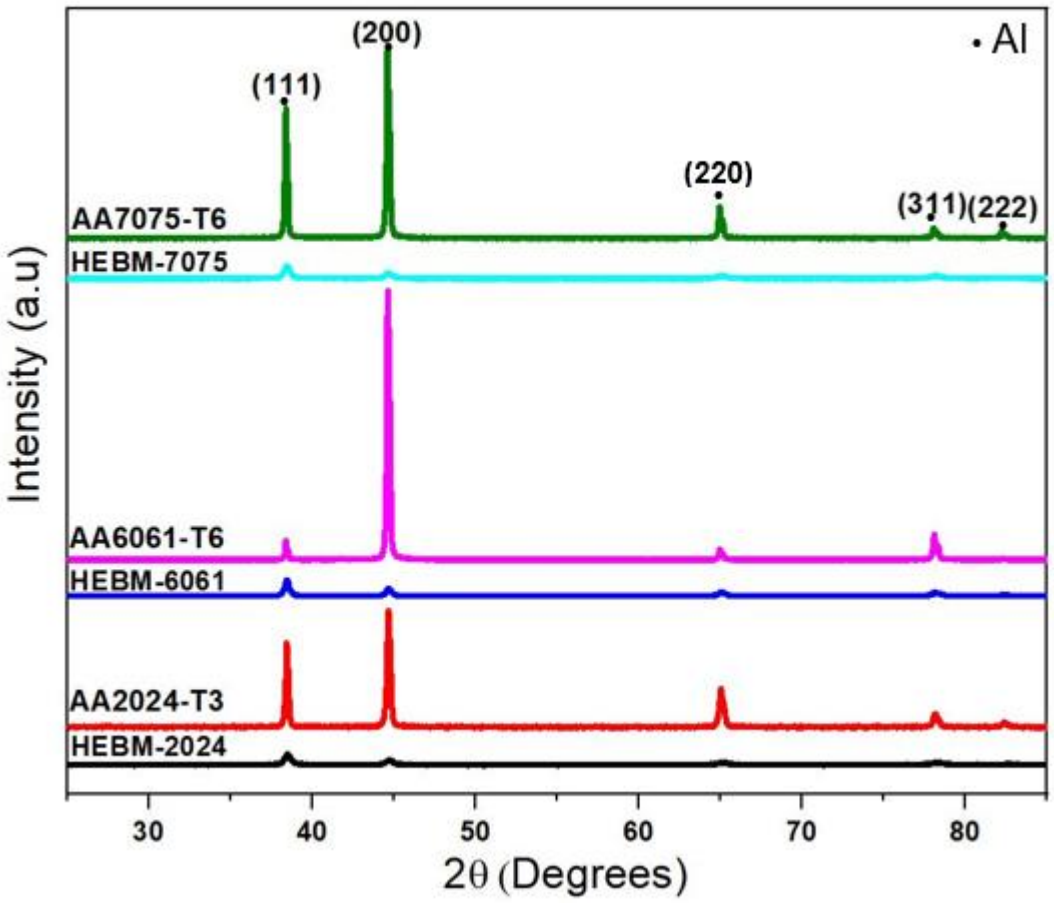

Figure 5.4 XRD patterns of AA2024-T3, AA6061-T6, AA7075-T6 and HEBM-2024, HEBM-6061, HEBM-7075

Figure 4 shows TEM images of the HEBM-2024. The bright field (BF) and dark field (DF) images (Figure 4a and 4b) show the existence of fine grains that further confirmed by the selected area diffraction pattern (SADP) presented in Figure 4c. Comparison of SADP pattern with theoretical values obtained from Powder Diffraction File™ (PDF®) databases (PDF Card -00-004-0787_Al) revealed that the

pattern belongs to Al-FCC with approximate lattice parameter of 4.07013 ± 0.00426 Å [116]. The grain size and its distribution within the DF image in Figure 4b is presented in Figure 4d. The average grain size for HEBM-2024 was determined as 27.5 (±12.5) nm which are in close agreement with the grain size calculated via XRD analysis.

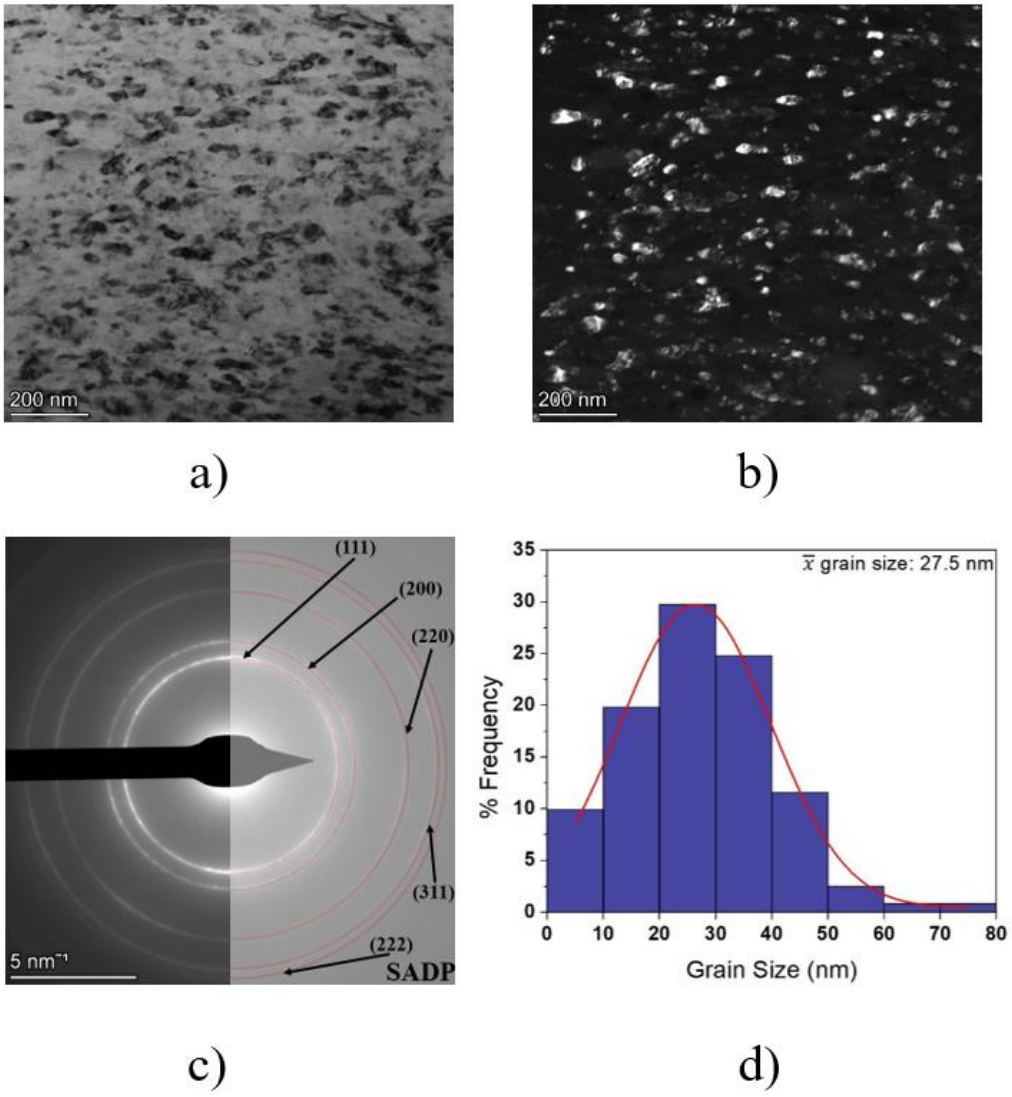

Figure 5.5 TEM micrographs of HEBM-2024; a) BF image b) DF image c) SADP. d) Grain size and its distribution within the DF micrograph in b).

5.4.2 Corrosion behavior of the alloys

The cyclic potentiodynamic polarization (CPP) curves for HEBM-2024, HEBM-6061, HEBM-7075 along with AA2024-T3, AA6061-T6, AA7075-T6 are presented in Figure 5.6. Polarization curves demonstrate the influence of HEBM on the corrosion behavior. The corrosion potential (E_{corr}), corrosion current density (i_{corr}), pitting potential (E_{pit}) and protection potential (E_{prot}) were determined from the CPP graphs and are presented in

Table 5.2. The wrought alloys demonstrated no clear breakdown potential in the anodic branch which has been reported in the literature due to the occurrence of the pitting below the open current potential (OCP) [34,66,117]. A clear passive region was visible in the CPP curves for the ball milled alloys. Curves show absence of metastable pitting and evidence of passivity breakdown (pitting potential). Anodic polarization produces an increase in measured current density with increasing potential, as alloys are oxidized and ions transport through the oxide. The increase seems to be relatively comparable between the three experimental alloys, suggesting oxide films of similar thickness and/or growth rate during anodic polarization. The pitting potential of the ball milled alloys were significantly more positive than open current potential. HEBM alloys exhibited a wide passive window (E_{corr}-E_{pit}) whereas no passive window was visible for the wrought alloys. E_{corr} of the HEBM alloys were lower than the wrought alloys and this phenomenon can be attributed to the lower cathodic current density caused by the refined intermetallics. i_{corr} which is also calculated by Tafel extrapolation method indicated that i_{corr} of the HEBM alloys significantly lower than the wrought alloys. In addition, HEBM alloys indicated pit transition potential (E_{ptp}) and protection potential (E_{prot}) in all cases that the combination of all contributions can be interpreted as HEBM alloys have superior corrosion resistance among the investigated alloys.

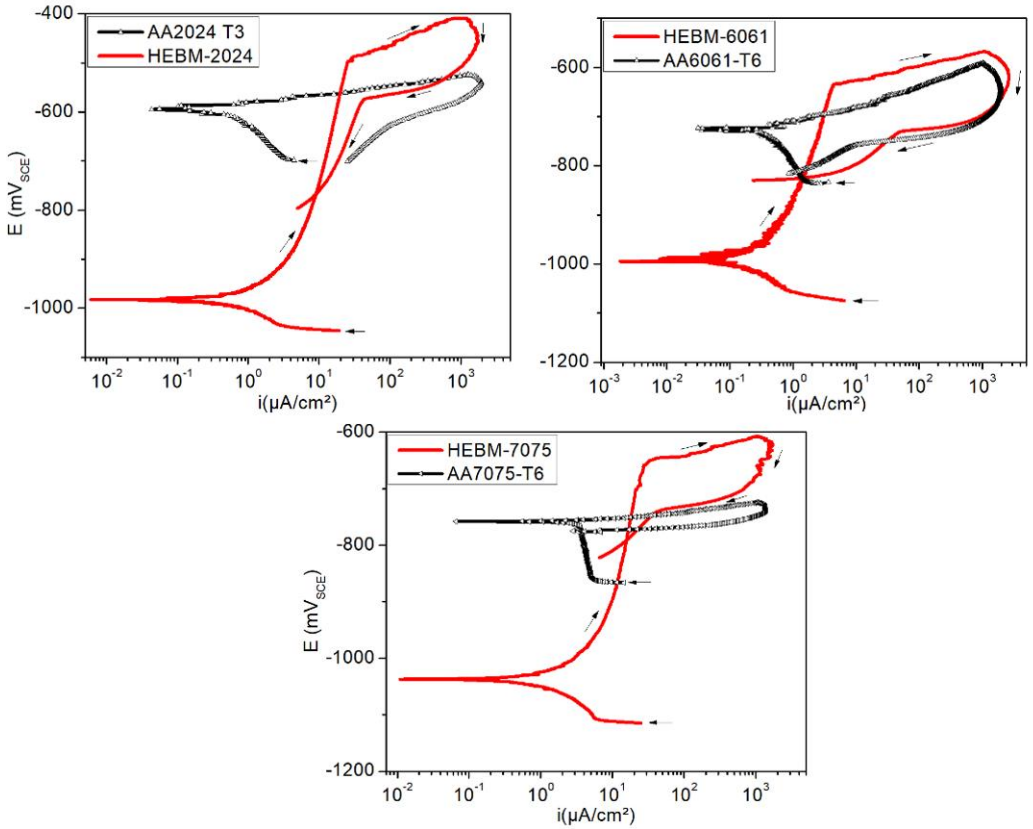

Figure 5.6 Cyclic Potentiodynamic Polarization curves of a) HEBM-2024 and AA2024-T3, b) HEBM-6061 and AA6061-T6, and c) HEBM-7075 and AA7075-T6

Table 5.2 The average electrochemical parameters and corresponding standard deviations of alloys determined from CPP curves in 0.6 M NaCl at room temperature.

	E_{corr}	i_{corr}	E_{pit}	E_{ptp}	E_{prot}
	(mV_{SCE})	($\mu A/cm^2$)	(mV_{SCE})	(mV_{SCE})	(mV_{SCE})
HEBM-2024	-984 (±82)	0.14 (±0.06)	-477 (±20)	-572 (±6)	-736 (±10)
AA2024-T3	-585 (±23)	0.38 (±0.02)	<E_{corr}	-627 (±8)	-
HEBM-6061	-990 (±133)	0.06 (±0.02)	-623 (±18)	-730 (±8)	-824 (±12)
AA 6061-T6	-722 (±85)	0.22 (±0.08)	-710 (±19)	-755 (±3)	-

HEBM-7075	-1035 (±76)	0.15 (±0.08)	-654 (±12)	-738 (± 2)	-789 (±13)
AA7075-T6	-757 (±43)	3.36 (±0.32)	$<E_{corr}$	-	-

Figure 5.7 shows the current density versus time graph for the wrought and ball milled alloys in 0.6M NaCl. The applied potential was 150 mV above the open circuit potential. The ball milled alloys shows a continuous decrease in the current density and currents reached less than 1 $\mu A/cm^2$ which shows strongly passive nature of the alloys. On contrary, wrought alloys showed high current density, exceeding 1 mA/cm2 in a few minutes Figure 5.7. Current density versus time graphs (Figure 5.7) corroborated the conclusions from the CPP data (Figure 5.6).

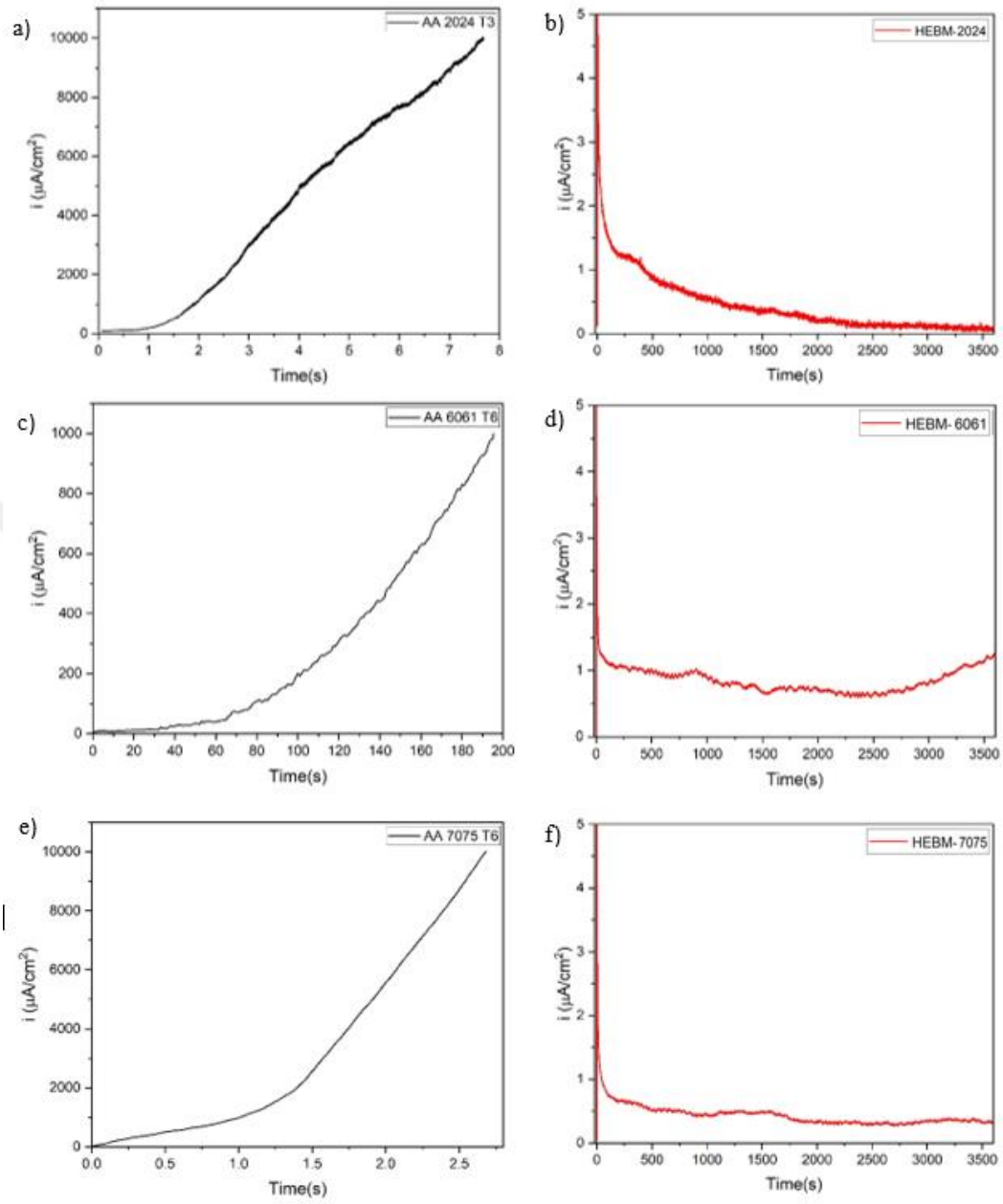

Figure 5.7 Potentiostatic polarization in 0.6M NaCl at an applied potential of 150 mV above open circuit potential for a) AA 2024 T3, b) HEBM-AA 2024, c) AA 6061 T6, d) HEBM-AA 6061, e) AA 7075 T6 and, b) HEBM-AA 7075.

Figure 5.8 indicates areas of the specimens that immersed in the 0.6 M NaCl solution for 1 h. It is observed that the corrosion in the wrought alloys was associated primarily with the constituent particles in the sample surface (Figure 5.8). The BSE image indicated that the pitting that formed as trenches and dissolution of the intermetallic

particles on the sample surfaces. EDS analysis verified that the secondary phase particles had galvanic interaction with the matrix. Al, Cu, Fe, and Mn containing particles were found to initiate the dissolution of matrix by leaving trenches at their surroundings. The dissolved particles were found Cu enriched (Figure 5.8), and Fe and Si enriched in Figure 7e. The BSE images of HEBM-2024, HEBM-6061 and HEBM-7075 immersed for 1 hour in 0.6 M NaCl are shown in (Figure 5.8). The homogenous microstructure due to the refined or dissolved secondary phase particles led significant decrease in the size and number of pits observed in HEBM alloys. The EDS analysis indicated the particles responsible for the corrosion initiation as trenches in HEBM alloys contained Fe and Cr which are originated due to abrasion of milling media.

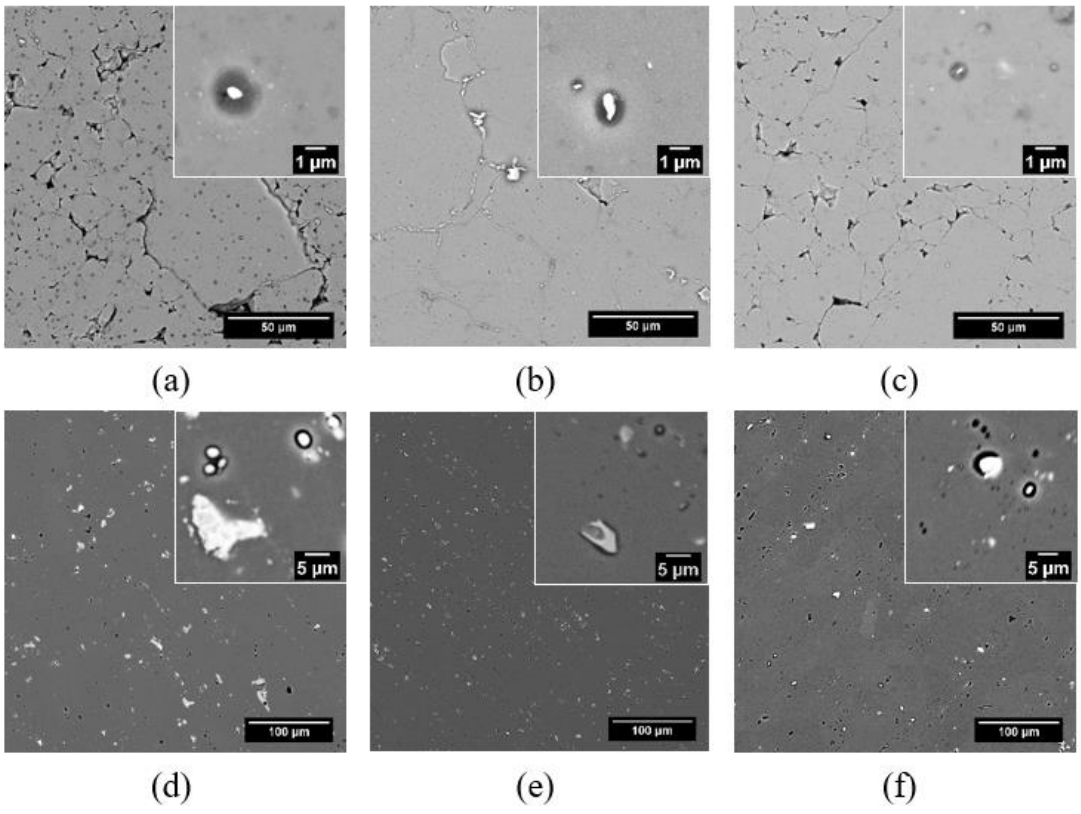

Figure 5.8 SEM micrographs after 1 hour of immersion in 0.6 M NaCl (a) HEBM-2024, (b) HEBM-6061, (c) HEBM-7075, (d) AA2024-T3, (b) AA6061-T6 and (c) AA7075-T6 without removing the corrosion products. Corresponding high magnification images are shown in the inset.

Figure 5.9 shows the morphology of alloys that immersed in 0.6 M NaCl for 14 days after removing the corrosion products in 30 vol% of HNO3. The effects of prolonged immersion were apparently revealed in wrought alloys (Figure 5.9 8d-8f). The BSE images indicated significantly larger pits that primarily associated to the dealloying of the constituent particles. The BSE images of HEBM-2024, HEBM-6061 and HEBM-7075 are presented in Figure 5.9 8a-8c. The lack of coarse constituent particles and homogenous microstructures led sustainability of superior corrosion performance in the high-energy ball milled alloys.

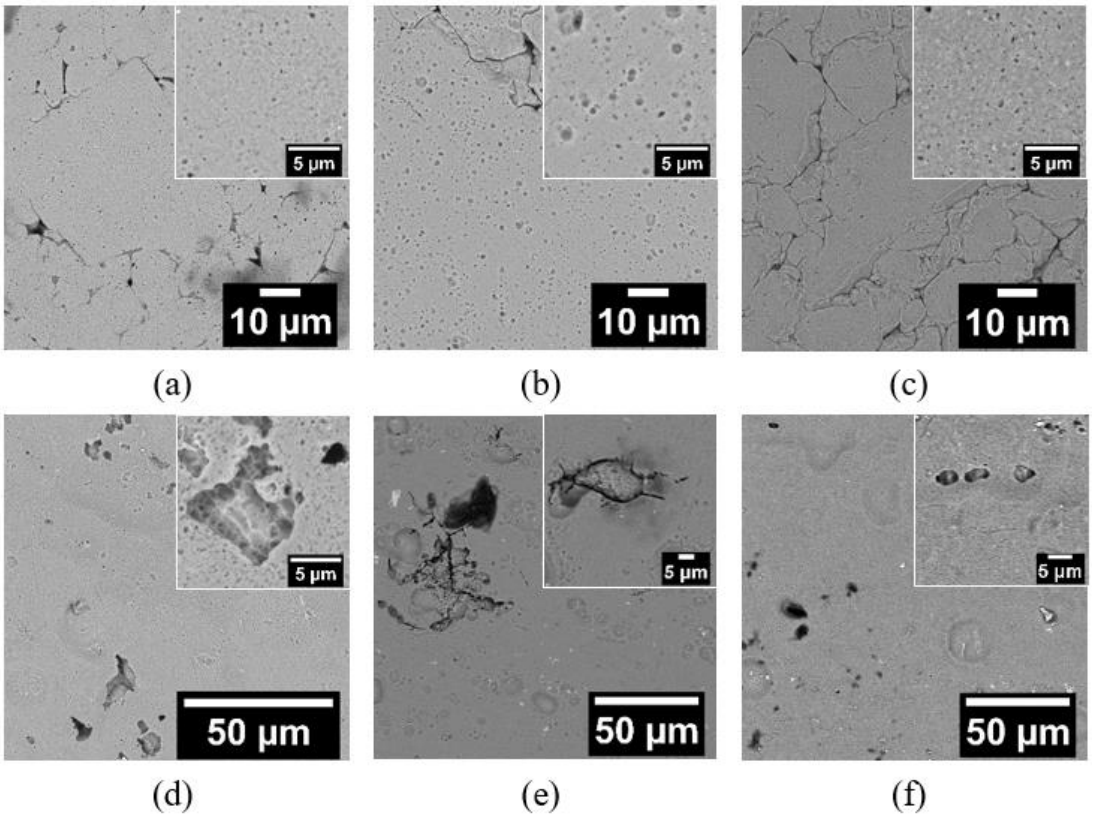

Figure 5.9 SEM micrographs after 14 days of immersion in 0.6 M NaCl (a) HEBM-2024, (b) HEBM-6061, (c) HEBM-7075, (d) AA2024-T3, (e) AA6061-T6 and (f) AA7075-T6 after removing the corrosion products. Corresponding high magnification images are shown in the inset.

5.4.3 Hardness of the ball-milled alloys

Average Vickers microhardness of HEBM alloys and wrought alloys are presented in **Figure 5.10**. Average Vickers hardness values were ~240 HV, ~185 HV and ~269 HV for HEBM-2024, HEBM-6061 and HEBM-7075 while the values for wrought AA2024-T3, AA6061-T6 and AA7075-T6 were ~137 HV, ~108 HV and ~176 HV. HEBM alloys indicated a significant increase in the hardness values which is consistent to the reported literature on the nanocrystalline aluminum alloys [9,36,55,102]. The high strength of the HEBM alloys was attributed to the joint influence of grain refinement, solid solution strengthening and uniform dispersion of fine intermetallics [118]. The individual elements of the various strengthening mechanisms were quantified in several studies that reviewed in [118].

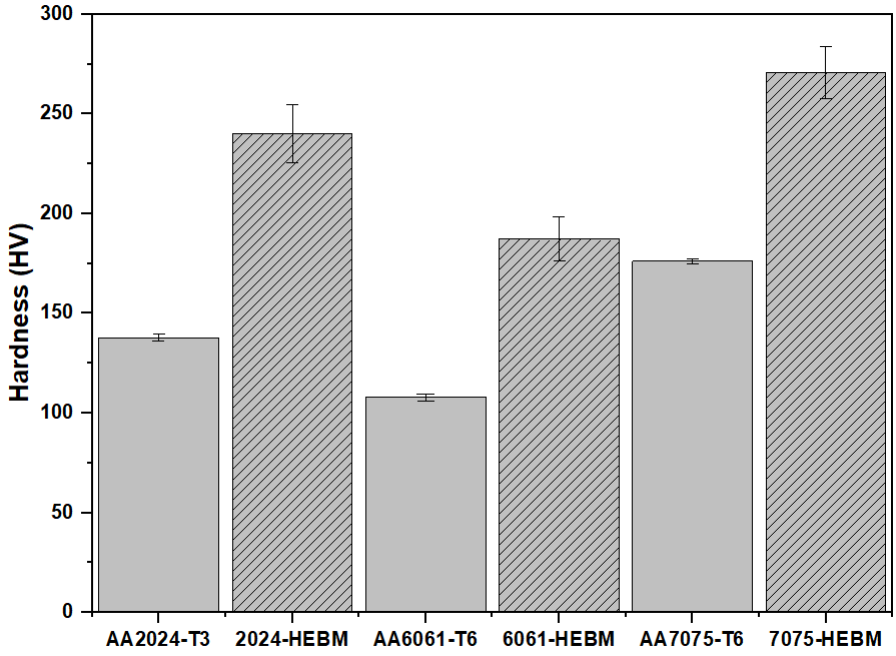

Figure 5.10 Vickers hardness measured for AA2024-T3, AA6061-T6, AA7075-T6 and HEBM-2024, HEBM-6061, HEBM-7075

The total yield strength of the alloy can be quantified as:

$$\sigma_y = \sigma_o + \sigma_{gb} + \sigma_d + \sigma_{ss} + \sigma_{pp} \quad (1)$$

where, σ_o is the yield strength of base metal (17 MPa) [119]. σ_{gb} is the strength contribution by grain boundaries, σ_d is the yield strength contribution by dislocations, σ_{ss} is the yield strength contribution by solute atoms and σ_{pp} is the yield strength contribution by precipitates.

The yield strength of the HEBM alloys were predicted by Tabor's rule [120] to estimate individual strength contributions.

$$\sigma_y \approx H * \frac{1}{3} \quad (2)$$

Where H is the microhardness value in MPa. The estimated yield strengths of the alloys were calculated as 784.56 MPa, 604.64 MPa and 879.36 MPa for HEBM-2024, HEBM-6061 and HEBM-7075 respectively.

The estimation of the strength contribution by grain boundaries (σ_{gb}) were calculated by the Hall-Petch equation [119]:

$$\sigma_{gb} \approx k(d)^{1/2} \quad (3)$$

where, k is the Hall-Petch coefficient 0.09 $MPa^{1/2}$ [6,121,122] and d is the grain size. The estimated contributions of σ_{gb} were calculated for 528.49 MPa, 455.7 MPa and 569.20 MPa for HEBM-2024, HEBM-6061 and HEBM-7075 respectively. Calculations indicated that the major contribution to the yield strength was by grain boundaries.

The contribution of dislocation strengthening (σ_d) is obtained by Bailey-Hirsch equation [123,124]:

$$\sigma_d = \underline{M}\alpha G b \rho^{\frac{1}{2}} \quad (4)$$

Where $\underline{M}$ is average orientation factor (3.06), α is constant (0.2), G is shear modulus (26 GPa), b is burger's vector (0.286 nm) and ρ is the dislocation density that calculated by:

$$\rho = \frac{2\sqrt{3}\varepsilon}{Db} \qquad (5)$$

Where ε is lattice strain and D is grain size that are calculated from XRD data.

The increment in the strength caused by dislocation strengthening was calculated as 165.96 MPa, 119.36 MPa and 170.33 MPa for HEBM-2024, HEBM-6061 and HEBM-7075 respectively. Calculations indicated that the dislocation strengthening was secondary contribution in HEBM alloys after strength contribution by grain boundaries.

The strength contribution by solute atoms (σ_{ss}) were calculated by following equation [123,125]:

$$\sigma_{ss} = \underline{M} G b \varepsilon^{\frac{3}{2}} c^{\frac{1}{2}} \qquad (6)$$

where c is the solute concentration with the power that assumed as 0.5 [123]. Solute contribution is dependent to the lattice strain which arises from the difference between solute and solvent atom size. Table 3 shows primary solute atoms in the commercial aluminum alloys and theoretical contributions to yield strengths using the data on high-purity binary alloys [33]. Assuming complete solubility of all solute atoms with the HEBM process would enable to calculate maximum theoretical contribution by solute solution strengthening. Therefore, maximum theoretical contribution of σ_{ss} was calculated as 102.56 MPa, 39.75 MPa and 103.5 MPa for HEBM-2024, HEBM-6061 and HEBM-7075 respectively. Considering the theoretical maximum as free of possible secondary phases that consist of the compounds of solutes are not dissolved in the solvent, the actual contribution values must be less and thus it can be concluded that the contribution of the solute atoms to strengthening was not significant.

Experimental value of yield strength (calculated by Tabor's rule) and calculated individual contributions of grain boundary strengthening, solid solution strengthening and dislocation strengthening to the estimated theoretical yield strength are shown in Figure 5.11. Grain refinement contribution was in in between 65 to 74% of the total estimated strength of the HEBM alloys. Therefore, grain refinement could be agnominated as dominant mechanism in the enhanced strength. Contribution by precipitates and dispersoids can be estimated by Orowan strengthening (σ_{Or}) [122] which is dependent to radius of the precipitates. SEM analysis did not provide enough data about the size and shape of precipitates in HEBM alloys. However, σ_{Or} were reported to have minor contributions in the high-energy ball milled alloys despite the Orowan strengthening has accountable contribution in precipitation hardened alloys [121,126–128].

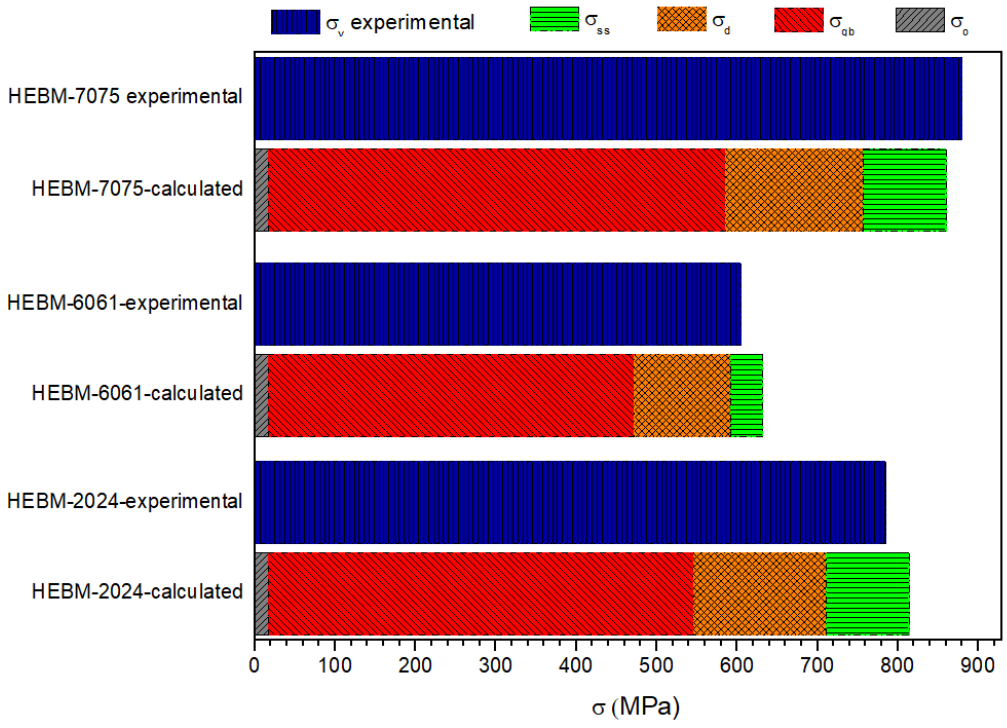

Figure 5.11 Experimental yield strength (σ_y, calculated by Tabor's rule) and calculated contributions of base metal (σ_o), grain boundary strengthening (σ_{gb}), dislocation strengthening (σ_d), solid solution strengthening (σ_{ss}) to overall yield strength for HEBM-2024, HEBM-6061, HEBM-7075

5.5 General discussion

Constituent particles which include active alloying elements found in the investigated wrought alloys were highly associated to localized corrosion. AA2024-T3 indicated a high Al_2CuMg content which was reversed from more noble to less-noble particles by dealloying and incongruent dissolution when exposed to 0.6 M NaCl solution [30]. Corrosion is mainly attributed to S-phase particles together with Fe containing particles which were responsible for the dissolution of matrix of 2024-T3 [70,79,117,129,130]. In addition to Cu containing phases, Zn containing particles such as $MgZn_2$ were mainly attributed to the anodic dissolution or peripheral pitting depending on the electrochemical activity of the secondary phase respect to the matrix in AA7075-T6 [30]. Al-Si-Fe-containing cathodic particles and Mg_2Si could be attributed to the matrix dissolution in AA6061-T6 [131].

Corrosion behavior of the aluminum alloys mainly associated to characteristics of secondary phase particles and their interaction with the matrix. The modification in the corrosion behavior of HEBM alloys could be attributed to the HEBM process which is known to provide nanocrystalline structures with enhanced diffusivity and free energy, formation of super saturated matrix and metastable phases, and increased homogeneity in the microstructure [9,47,54,58,102]. Furthermore, significant refinement of Fe and Cu rich intermetallics by the HEBM process (seen in Figure 2) is expected to decrease the cathodic sites and therefore overall cathodic reaction rate which is oxygen reduction reaction for the corrosion of aluminum alloys [132]. A decrease in the cathodic reaction due to refined microstructure could be attributed to high corrosion resistance in the ball milled alloys.

This study indicated that hardness and corrosion performance of the age hardening commercial alloys could be significantly enhanced by the high-energy ball milling. The powder obtained by high energy ball milling is a promising feedstock material for possible applications of several additive manufacturing and surface modification techniques.

5.6 Conclusions

The influence of high-energy ball milling on the corrosion and hardness of the AA2024, AA6061 and AA7075 were investigated in this work. Main conclusions can be summarized as follows:

- Homogenous microstructure, free from coarse secondary phases, and significant grain refinement (below 100 nm) were achieved after high-energy ball milling of pre-alloyed powders.
- High-energy ball milled age hardening alloys exhibited significantly enhanced corrosion resistance as represented by higher pitting and protection potentials, and lower corrosion current densities. High corrosion resistance is attributed mainly to absence of coarse intermetallics, possible incorporation of impurity elements in solid solution, and grain refinement below 100 nm.
- The hardness of the HEBM alloys showed remarkable increase which was attributed to the combined effect of nanocrystalline structure, work hardening and extended solid solubility of the alloying elements in Al matrix. The predominant contribution to the strengthening in the HEBM alloys was by grain refinement which was predicted to between 67 to 75% of total estimated yield strength.
- Hardness and corrosion performance of the age hardening aluminum alloys were enhanced simultaneously by HEBM that can be employed in the production of high strength and corrosion resistant Al alloys.

CHAPTER 6

INFLUENCE OF HIGH ENERGY BALL MILLING ATMOSPHERE ON THE CORROSION OF NANOCRYSTALLINE ALUMINUM ALLOYS

6.1 Abstract

This chapter compares the corrosion behavior and hardness of an Al alloy (AA2024) produced by high-energy ball milling in air and high purity Ar. The pre-alloyed AA2024 powder was milled in Ar and air atmospheres and the produced powder was successfully consolidated to investigate the hardness and corrosion performance. Cyclic potentiodynamic polarization tests revealed higher pitting potential for the alloy milled in air. Additionally, milling in air resulted in higher hardness and thermal stability after a one-hour isothermal heat treatment at 400 and 500 °C. Our results demonstrate that a high purity Ar atmosphere is not a requirement for all applications and milling in the air can lead to excellent properties. The findings of this chapter is published in [133] and reproduced with a licence provided with Springer Nature (see Appendix).

6.2 Introduction

Due to the increasing demand for lightweight and high-strength materials, calls for a longer service life of aluminum alloys are increasingly being voiced for environmental concerns [7,35]. Aluminum alloys are used in many fields such as aerospace and automotive due to their excellent properties [1,17]. However, high-strength aluminum alloys, where high strength leads to corrosion problems, have limited use in many applications [22,55]. Non-conventional processing techniques have shown that the properties of Al alloys can be significantly enhanced [35,38,46].

High-energy ball milling (HEBM) of Al alloys has been reported to enhance the properties beyond conventional limits [6,9,38,47,48,55,126]. Extended solid

solubility, nanocrystalline structure and uniformly distributed fine secondary phases have been attributed to enhanced corrosion resistance and strength of the ball milled Al alloys. The alloy powder produced by HEBM is influenced by several parameters such as the nature of material, the size of the starting powder, the milling media, the milling time, the milling speed, the milling temperature, and the milling atmosphere [6,114,134]. The influence of these parameters on HEBM of Al alloys has been reviewed recently [6]. HEBM of aluminum alloys is commonly performed in an inert atmosphere (high purity argon or nitrogen) to avoid oxidation of aluminum. Therefore, majority of the research on HEBM reports the use of inert gases or vacuum during milling [6,114,135]. Some studies even reported conducting entire milling process inside the glove box [114]. However, necessity of an inert atmosphere in maintaining acceptable properties of the aluminum alloys has not been reported in literature and therefore it is of great merit to investigate the influence of the milling in air.

A hypothesis along with the experimental validation that HEBM in air may be advantageous and high purity Ar may not be required for HEBM of Al alloys is presented herein. The formation of any oxides during HEBM could be envisaged to cause dispersion strengthening [2,136] and incorporation of oxygen into the solid solution could enhance the corrosion resistance [2,137,138]. Superior corrosion resistance in sputter deposited Al has been reported when sputtering was performed in poor vacuum and incorporation of oxygen into Al has been associated with increased corrosion resistance [139]. Moreover, the thermal stability of the high-energy ball milled alloys has been reported to be higher than that of nanocrystalline alloys prepared by other methods, which is attributed to introduction of impurities from the milling environment that retards the grain coarsening when exposed to high temperature [140,141]. Therefore, successful accomplishment of the HEBM in air might be beneficial to improve the thermal stability of the Al alloy due to the possible incorporation of oxides or dispersoids. However, the influence of air on the ball milled Al alloys is not known and warrants research attention. This article compares the influence of HEBM performed in air and Ar on the corrosion, hardness, and thermal stability of AA2024.

6.3 Experimental

AA2024 powder (Valimet, AM2024) was ball milled in a planetary high-energy ball mill for 100 hours. AA2024 powder, stearic acid (1.5 wt.%) as a process controlling agent (PCA), and stainless-steel balls (16:1, ball to powder weight ratio) were placed in hardened stainless-steel vials and sealed in two different atmospheres: High purity Ar (O_2 < 25 ppm) in a glove box and air in ambient laboratory atmosphere. HEBM was interrupted for one hour after each hour of milling to avoid overheating. Milled AA2024 powder was cold compacted under uniaxial pressure of 3GPa. The Consolidated alloys of Ar milled and air milled AA2024 powder have been termed as HEBM-2024-Ar and HEBM-2024-Air, respectively. A commercial AA2024-T3 alloy (McMaster-Carr) was used for comparison. Heat treatment was carried out in a muffle furnace equipped with a type R thermocouple. HEBM-2024-Ar and HEBM-2024-Air were placed in furnace preheated to 400 and 500°C and heat treated for 1 hour, then subsequently removed from the furnace and quenched in water to cool down.

X-ray diffraction (XRD) analysis was carried out in Rigaku SmartLab diffractometer ($\lambda_{CuK\alpha}$=0.154056 nm) at a scan speed of 1°/min and a step size of 0.01 to scan the 2θ range of 25-85°. The grain size was calculated using the Scherrer's equation [142] after determining the contribution of instrumental broadening using LaB_6. Secondary electron (SE) and backscattered electron (BSE) images were obtained at 20 kV acceleration voltage, using FEI Verios 460L field emission scanning electron microscopy (SEM) equipped with an Oxford energy dispersive X-ray spectrometer (EDS). Final polishing of the specimens for SEM investigation was performed using 0.05 µm colloidal silica suspension. Specimens were rinsed and dried after cleaning in an ultrasonic ethanol bath for 5 min.

Micro-hardness was measured using a Mitutoyo SM Vickers hardness tester. A 100g of load was applied for a dwelling time of 10 s. Grinding was performed until 1200 grit before hardness measurements. Measurements were repeated at least ten times.

Cyclic potentiodynamic polarization (CPP) tests were performed using a VMP-300 potentiostat. Epoxy mounted samples were ground to 1200 grit under ethanol and ultrasonicated for surface cleaning. CPP tests were conducted in a conventional three-electrode flat-cell where platinum was the counter electrode, and saturated calomel electrode (SCE) was the reference electrode. The CPP curves were recorded at 1 mV/s scan rate in 0.6 M NaCl electrolyte until the current density of 1 mA/cm^2 was reached, at which the scan direction was reversed. The cathodic polarization curves were recorded from +5 mV to -1.5 V with respect to OCP.

Polarization tests performed at least three times to ensure reproducibility. Immersion tests were performed in 0.6 M NaCl for 1 h and 14 days. Prolonged immersion samples were ultrasonicated in dilute HNO_3 solution (30 vol%,) for one minute to remove the of corrosion products formed on surface. Cleaned samples were investigated in a Keyence VKx1100 confocal laser scanning microscopy.

X-ray photoelectron spectroscopy (XPS) analysis was performed to evaluate the chemical composition of the surface film developed on the alloy surface. Samples were polished to 0.05 µm and the air-formed oxide film investigation was performed on the scan area of 2x2 mm with a take-off angle of 60˚. Chamber pressure was kept below 10^{-9} mbar. Range of 0-1100 eV (binding energy) was scanned for survey scan to detect surface elements. Composition of the passive film and oxidation states of the elements were determined high-resolution spectra. The XPS data analysis was conducted by CASA software.

6.4 Results and discussion

The morphology of AA2024 powder, along with the corresponding distribution of particle size after HEBM is presented in Figure 6.1. The shape and mean particle size of the powder produced in both atmospheres were similar (Figure 6.1 and b). The particle size distribution chart indicated a similar skew in both materials (Figure 6.1 c and d).

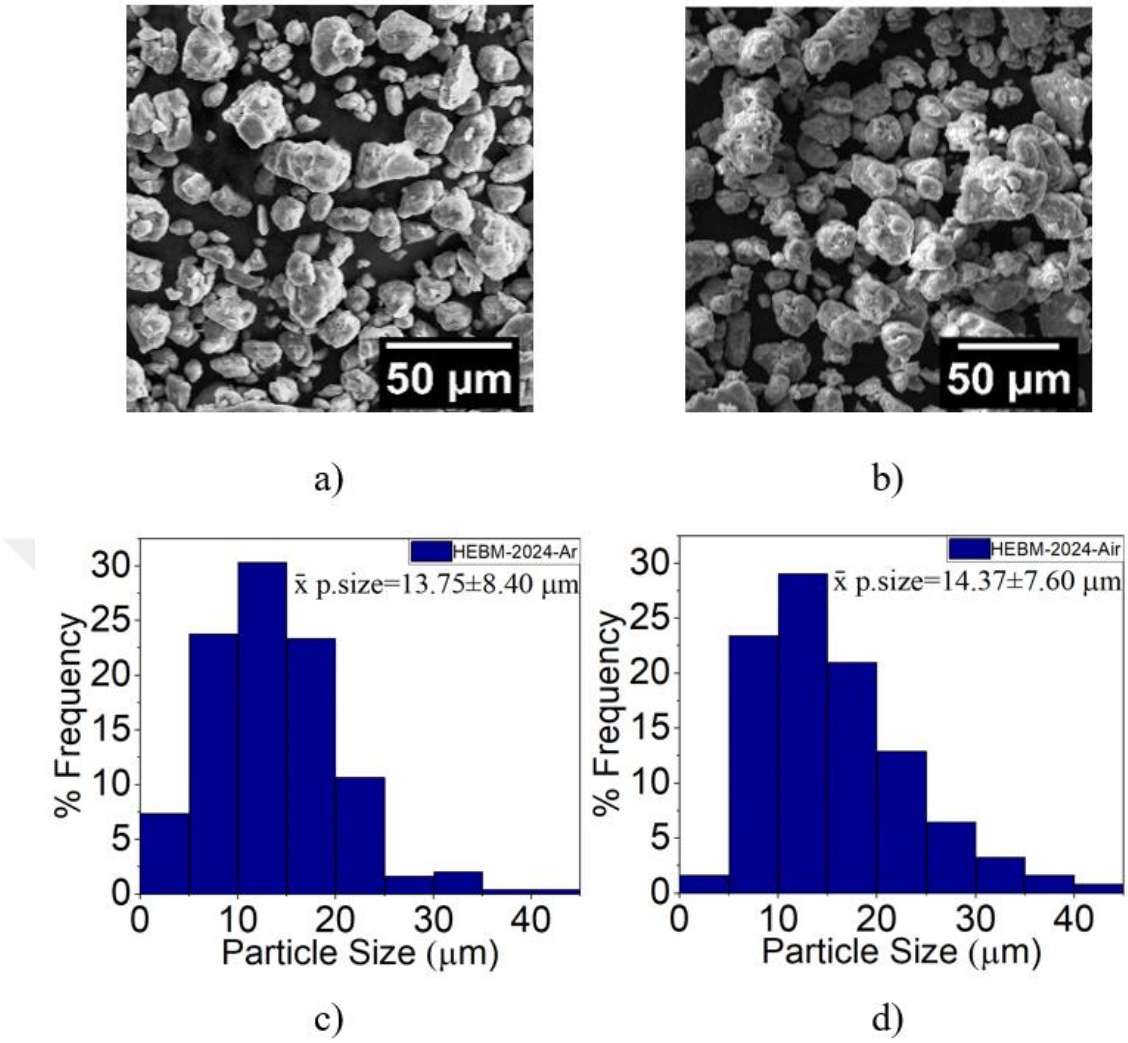

Figure 6.1 . Backscattered electron (BSE) images for powders of (a) HEBM-2024 powder milled in Ar, (b) HEBM-2024 powder milled in Air. Particle size distribution for c) HEBM-2024 powder milled in Ar and d) HEBM-2024 powder milled in Air.

The microstructure of the HEBM-2024-Ar, HEBM-2024-Air and AA2024-T3 is presented if Figure 6.2. The microstructures of HEBM-2024-Ar and HEBM-2024-Air were free of coarse intermetallics (Figure 6.2 2a and 2b), which were observed in AA2024-T3 (Figure 6.2 2c). The absence of coarse intermetallics is attributed to HEBM and is consistent with the literature [6,65,102,143].

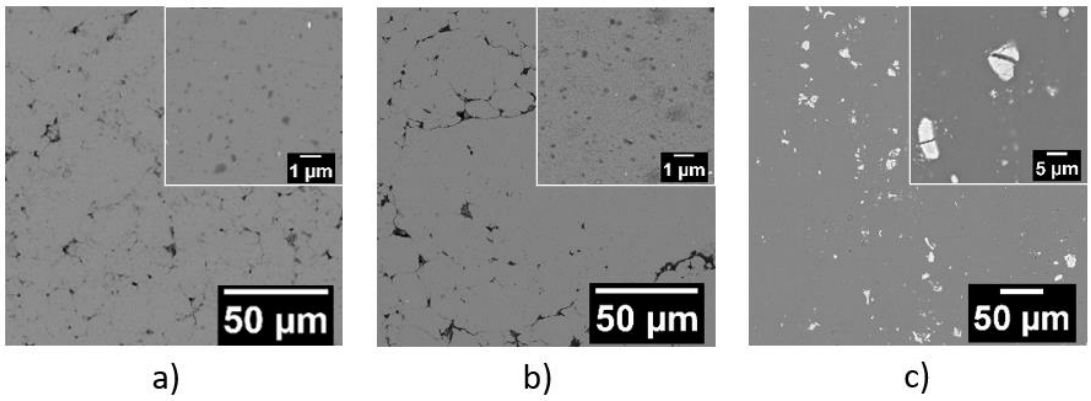

Figure 6.2 BSE images for a) HEBM-2024-Ar and b) HEBM-2024-Air; c) commercial wrought AA2024-T3. Corresponding high magnification images are shown in the inset.

The XRD patterns of the ball milled alloys along with AA2024-T3 are presented in Figure 3. XRD pattern of the ball milled alloys showed significant peak broadening due to the grain refinement in comparison to AA2024-T3. The average grain size calculated from XRD was 26.5 ± 8 nm for HEBM-2024-Ar and 23.5 ± 9 nm for HEBM-2024-Air. Decrease in the grain size due to HEBM in Air could be attributed to the incorporation of oxygen in Al as oxide or solid solution.

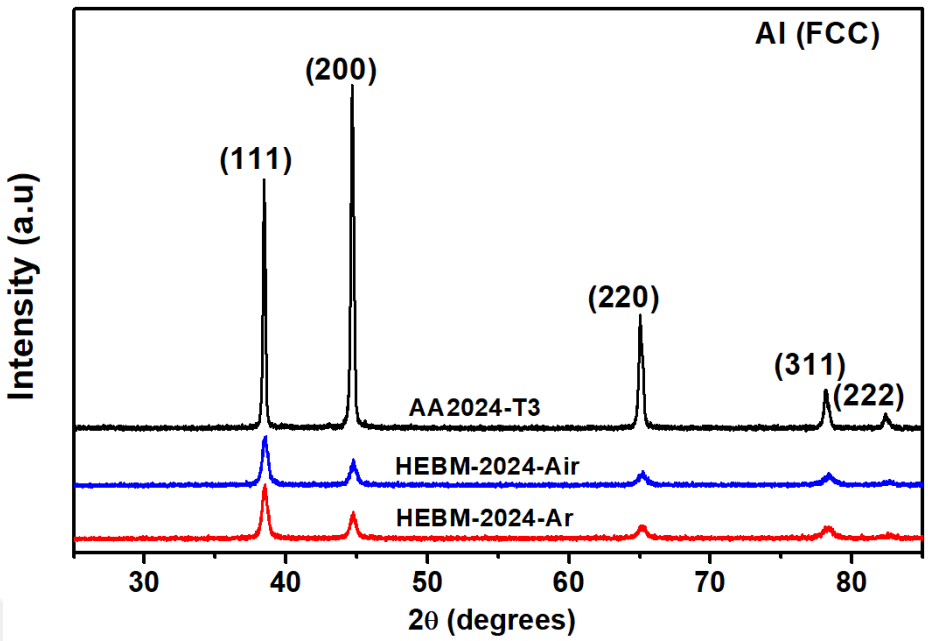

Figure 6.3 XRD pattern of HEBM-2024-Air, HEBM-2024-Ar and AA2024-T3.

The Vickers hardness and density of the alloys are shown in **Figure 6.4**. HEBM resulted in a significant enhancement in the hardness as compared to AA2024-T3, which could be attributed to the grain refinement and is consistent with the reported literature on the effect of grain refinement on hardness [118]. The strengthening mechanisms and calculations showing contribution of individual strengthening mechanisms are as follows,

The total yield strength of the HEBM alloys is estimated using Tabor`s rule by assumption of yield strength is approximately one third of the hardness [120].

The total strength of the HEBM-2024-Ar and HEBM-2024-Air was calculated as 785 MPa and 837 MPa respectively.

Grain boundary strengthening was calculated by Hall-Petch equation [144];

$$\sigma_{gb} = k * d^{-\frac{1}{2}}$$

where k is the Hall-Petch coefficient which is assumed as 0.09 $MPa^{1/2}$ [122], and d is the grain size.

Grain boundary strengthening (σ_{gb}) contribution calculated as 552 MPa for HEBM-2024-Ar and 587 MPa for HEBM-2024-Ar.

Total strength of the alloy can be estimated by considering a simple rule of mixture,

$$\sigma = \sigma_0 + \sigma_{gb} + \sigma_{ss} + \sigma_{or} \quad \text{(Eq 2)}$$

Where σ_0 is the strength contribution by pure metal; ~20 MPa for Al [9,121], σ_{ss} is the contribution by solid solution strengthening and defined by Eq 3; $\sigma_{or}$is the strength contribution by Orowan strengthening [145] defined by Eq 4.

$$\sigma_{ss} = HC^{\alpha} \quad \text{(Eq 3)}$$

Where H and α is material constants and C is the concentration of solute atoms.

$$\sigma_{or} = \left(\frac{\sqrt{3}Gblnln\,(d)}{2\pi(d)}\left(\frac{lnln\,(2r)}{lnln\,(d)}\right)^{3/2}\right) \quad \text{(Eq 4)}$$

Where G and b is the material constants, shear modulus and burger's vector respectively. d is interparticle distance and r mean radius of particles.

Cumulative contribution of solid solution and dispersion strengthening can be estimated by reorganizing Eq 2.

$$\sigma_{ss} + \sigma_{or} = \sigma - \sigma_0 - \sigma_{gb}$$

The cumulative contribution of solid solution strengthening, and dispersion strengthening was estimated as 213 MPa and 230 MPa for HEBM-2024-Ar and HEBM-2024-Air respectively.

HEBM-2024-Air exhibited a 6.6% increment in estimated overall strength compared to HEBM-2024-Ar, where grain refinement was estimated to contribute only 4.2% to the increase. Therefore, the higher hardness of HEBM-2024-Air could be due to the combined effect of grain refinement, incorporation of oxygen into solid solution, and possible dispersion of oxides formed in-situ, which fall beyond the detection limit of XRD.

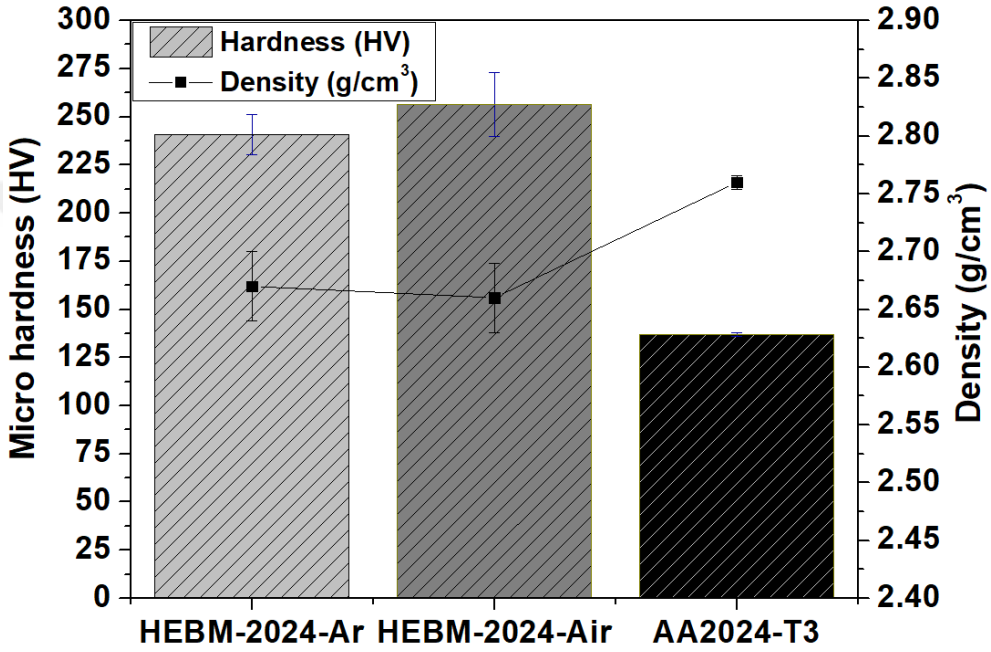

Figure 6.4 Hardness and density of HEBM-2024-Ar, HEBM-2024-Air and AA2024-T3

Cyclic potentiodynamic polarization curves are presented in Figure 5a. The pitting potential (E_{pit}), transition potential (E_{tr}), corrosion potential (E_{corr}) and corrosion current density (i_{corr}) obtained from CPP are presented in Figure 5b. The ennoblement in E_{pit} indicates higher pitting corrosion resistance and E_{tr} indicates repassivation ability. Comparing CPP curves, E_{pit}, E_{tr}, i_{corr} (Figure 5b) revealed that the corrosion performance of ball milled alloy, irrespective to milling atmosphere, was significantly higher than AA2024-T3. Ball milled AA2024, in both milling atmospheres, showed a wide passive window which was not observed in AA2024-T3. The lack of passive window in AA2024-T3 is consistent with the literature [13,65,146]. Milling in air provided ennoblement of the E_{pit} and E_{tr} compared to HEBM-2024-Ar The i_{corr} values

of the HEBM-2024-Ar and HEBM-2024-Air were similar and significantly less than AA2024-T3 which has a complex microstructure dictated by coarse particles that are cathodic to Al matrix.

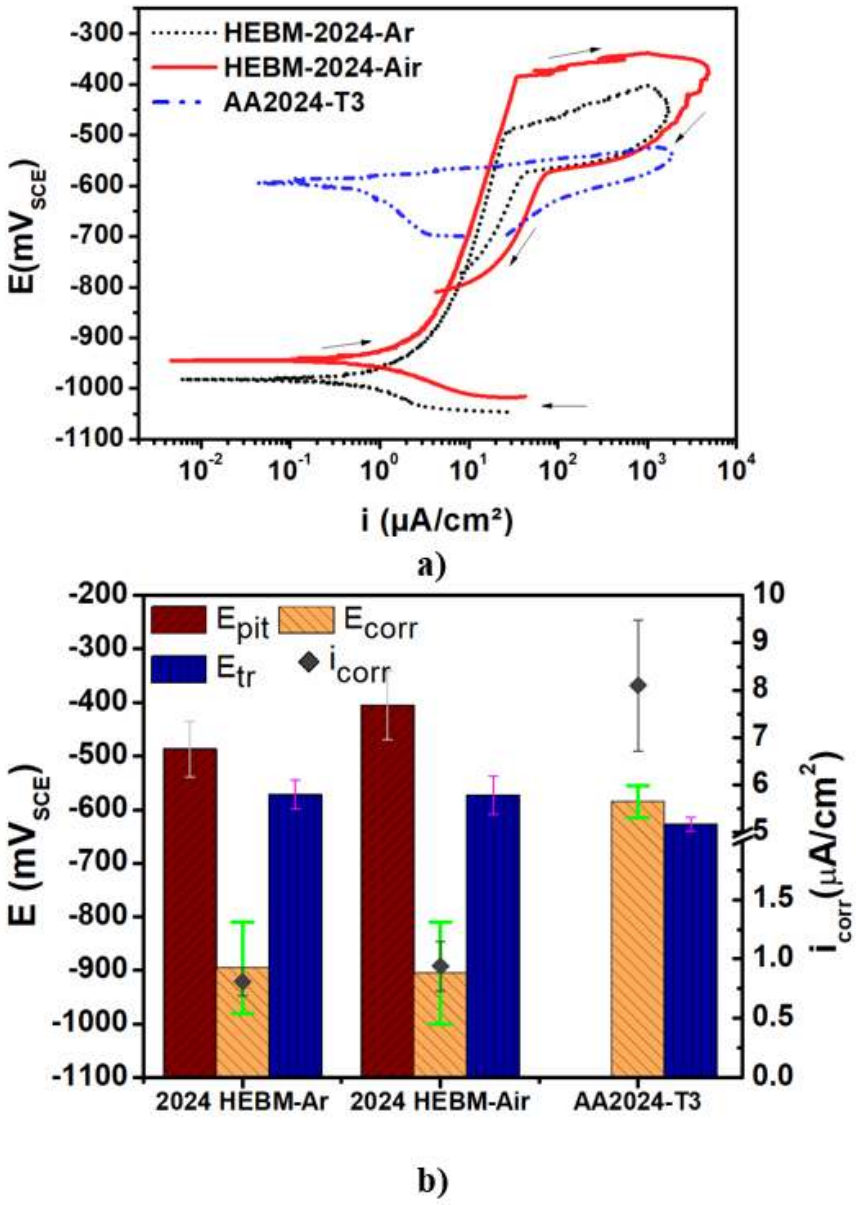

Figure 6.5 . (a) Cyclic Potentiodynamic polarization curves of HEBM-2024-Ar. HEBM-2024-Air and AA2024-T3 in 0.6 M NaCl (b) E_{pit}, E_{corr}, E_{tr} and i_{corr} for the HEBM-2024-Ar, HEBM-2024-Air and AA2024-T3

Cathodic polarization curves of the HEBM-2024-Ar, HEBM-2024-air along with AA2024-T3 are presented in Figure 6. Cathodic current densities for the HEBM-2024-Ar, HEBM-2024-air were significantly lower than that of AA2024-T3 which could be attributed to the decrease in the fraction of cathodic particles. Moreover, cathodic current density for HEBM-2024-air was slightly higher than that for HEBM-2024-Ar whereas the E_{corr} were similar. This indicated the corrosion to be dominated by decrease in anodic reaction kinetics due to the milling in air. This behaviour of decrease in anodic current density and ennoblement of pitting potential is similar to work of Frankel et al [139].

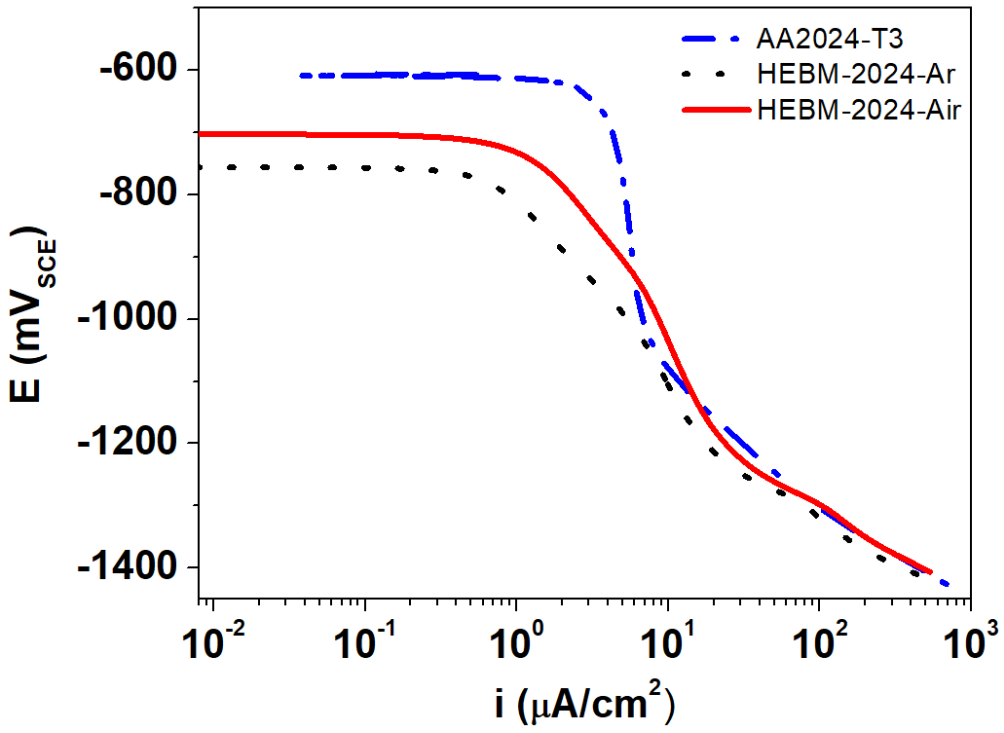

Figure 6.6 Cathodic polarization curves of AA2024-T3, HEBM-2024-Ar and HEBM-2024-Air tested in 0.6 M NaCl

The improved corrosion behavior of the ball milled AA2024 was further verified by surface analysis after immersion tests in 0.6 M NaCl. Figure 6.7 shows the BSE images of the alloys immersed in 0.6 M NaCl for 1 hour. The corrosion initiated at the interface of secondary phase particles and the matrix. The AA2024-T3 (Figure 6.7 7c) showed

large number of pits and dealloying even after 1 hours of immersion while ball milled alloys (Figure 6.7 7a and b) corrosion initiation at the interface of significantly refined particles and the matrix.

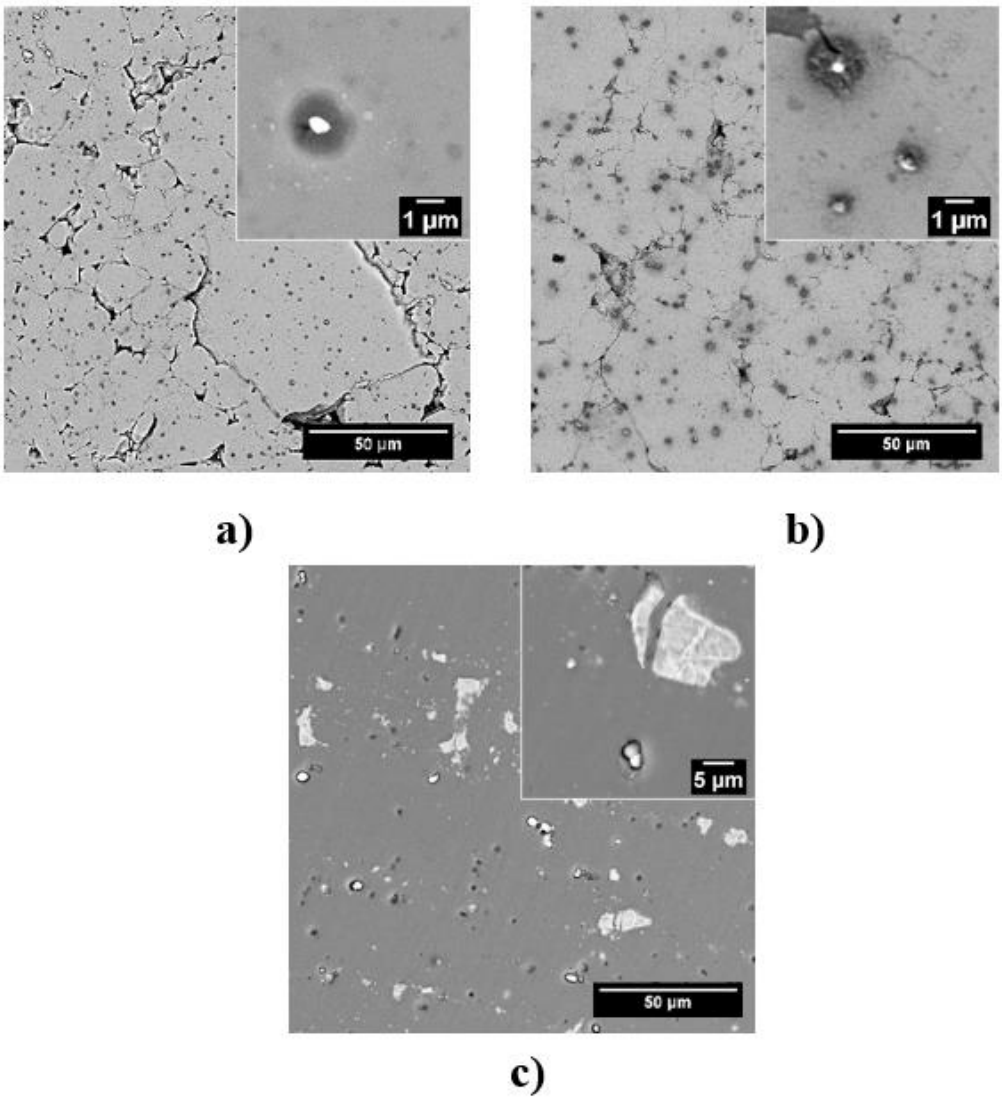

Figure 6.7 BSE images of a) HEBM-2024-Ar b) HEBM-2024-Air after immersion in 0.6 M NaCl solution for 1 hour.

Figure 6.8 shows the optical profilometry images of the alloys immersed in 0.6 M NaCl for 14 days, after removal of the corrosion products. The ball milled alloys showed significantly lower average pit depth (Figure 6.8a and b) as compared to AA2024-T3 (Figure 6.8c). Besides, the average pit depth in the HEBM-2024-Air alloy was lower than that HEBM-2024-Ar. The high corrosion resistance of ball milled

alloys could be attributed to the combined effect of grain refinement and elimination of coarse intermetallic particles [38,46,55,65].

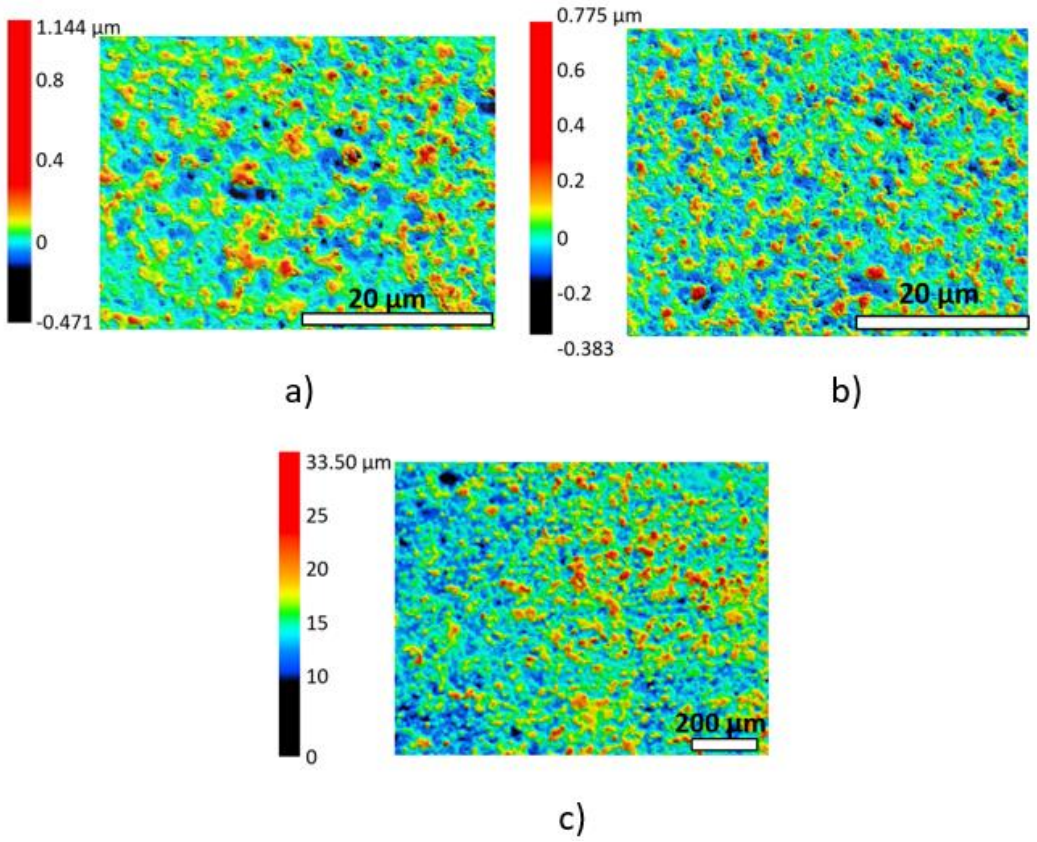

Figure 6.8 . Optical profilometry images of samples immersed in 0.6 M NaCl for 14 days (a) HEBM-2024-Ar (b) HEBM-2024-Air and (c) AA2024-T3

High resolution XPS spectra of Al2p and O1s peaks of HEBM-2024-Ar and HEBM-2024-Air are presented in Figure 6.9. Both alloys demonstrated peaks of Al^{0} and Al^{+3} which are associated to the metallic and oxidized aluminum, respectively [147,148]. The O1s spectra was deconvoluted into O-1 and O-2 peaks, where O-1 corresponds to contribution from oxide, while O-2 corresponds to hydroxide and/or oxygen bonded to the carbon contamination on the surface. Concentration (at. %) of elements is presented in Table 6.1. Al^{+3}/Al^{0} ratio for HEBM-2024-Air was higher than that for HEBM-2024-Ar. Furthermore, the oxygen content in HEBM-2024-Air was higher than HEBM-2024-Ar which could be attributed to increased oxygen content due to milling in air and the formation of a thicker passive film.

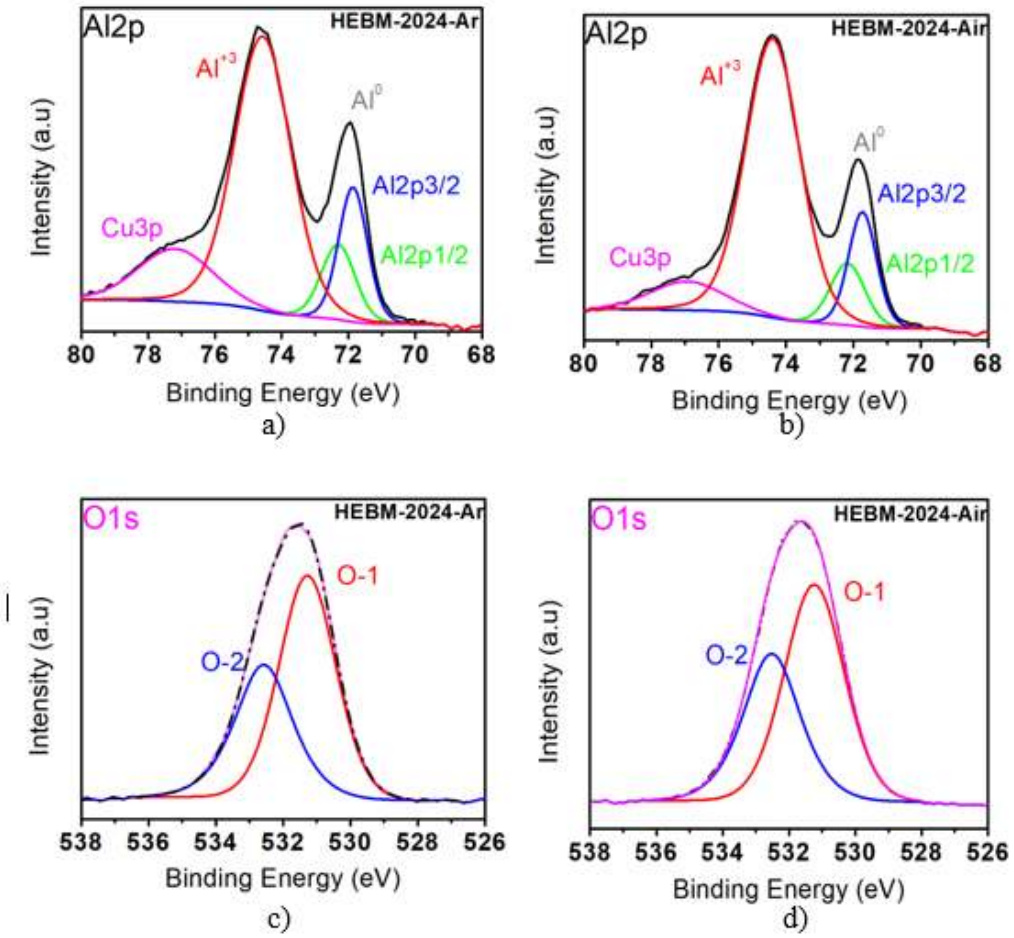

Figure 6.9 XPS high-resolution spectra of Al 2p for a) HEBM-2024-Ar, b) HEBM-2024-Air and O1s for c) HEBM-2024-Ar, d) HEBM-2024-Air

Table 6.1 Atomic concentration of elements on the surface of HEBM-2024-Ar and HEBM-2024-Air

Alloy	Concentration (at. %)		
	Al2p	O1s	Cu2p3/2
HEBM-2024-Ar	46.99	51.99	1.01
HEBM-2024-Air	38.83	60.68	0.49

Ball milled alloys were isothermally heat treated at 400 °C and 500 °C for 1 hour to investigate influence of milling atmosphere on thermal stability. Nanocrystalline materials due to the large driving force arising from the disordered grain boundaries, are prone to grain growth [149]. However, ball milling is reported to provide significant resistance to growth of nano-scale grains, which is attributed to mechanisms such as the effect of pinning forces caused from impurities or the formation of fine precipitates during ball milling or heat treatment steps [35]. XRD patterns of the HEBM-2024-Ar and HEBM-2024-Air after heat treatment are presented in Figure 6.10. Diffraction peaks that are apart from Al, such as Al_2Cu and Al_2CuMg were visible after 400 °C treatment. The zoomed (111) plane of the XRD patterns of the heat treated HEBM-2024-Ar and HEBM-2024-Air are presented in Figure 6.11. In both milling atmospheres, the 111 peak is shifted to lower 2θ values with the heat treatment, which implies the increase in the lattice parameter. The 111 peak of the HEBM-2024-Air showed more broadening as compared to HEBM-2024-Ar. The improved thermal stability is attributed to formation of impurities such as Al oxide, which hinder grain growth when exposed to high temperature [40,150].

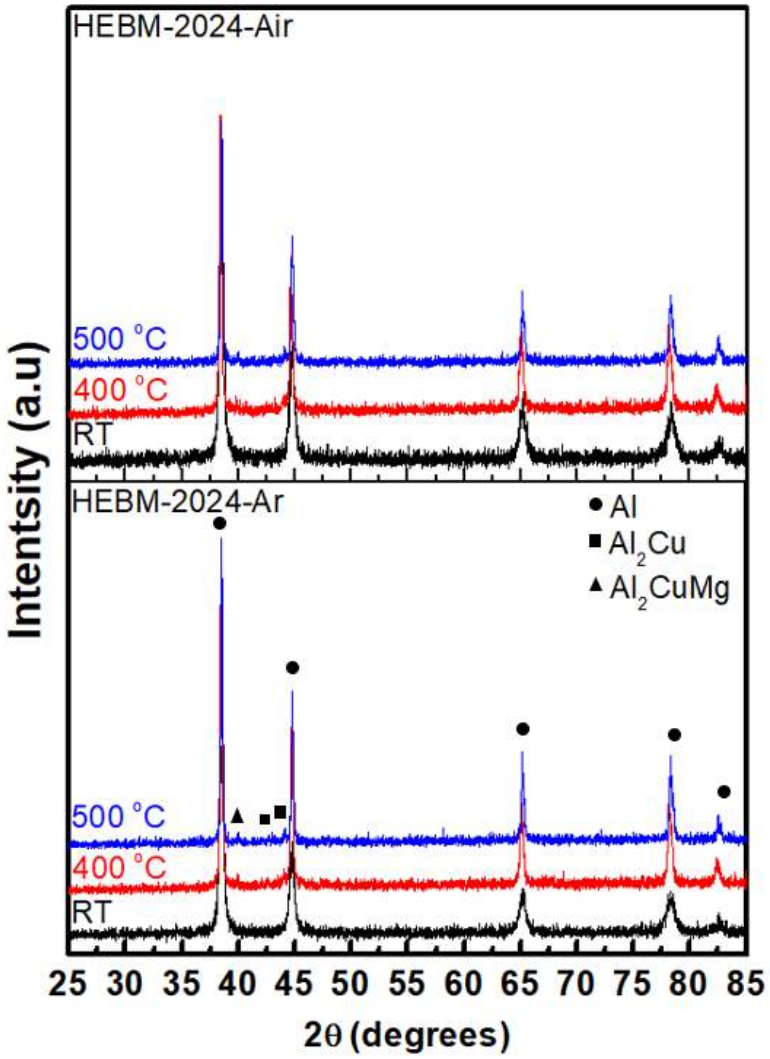

Figure 6.10 XRD scan of a) HEBM-2024-Ar and HEBM-2024-Air after 1 hour heat treatment at 400°C b) HEBM-2024-Ar and HEBM-2024-Air after 1 hour heat treatment at 500°C

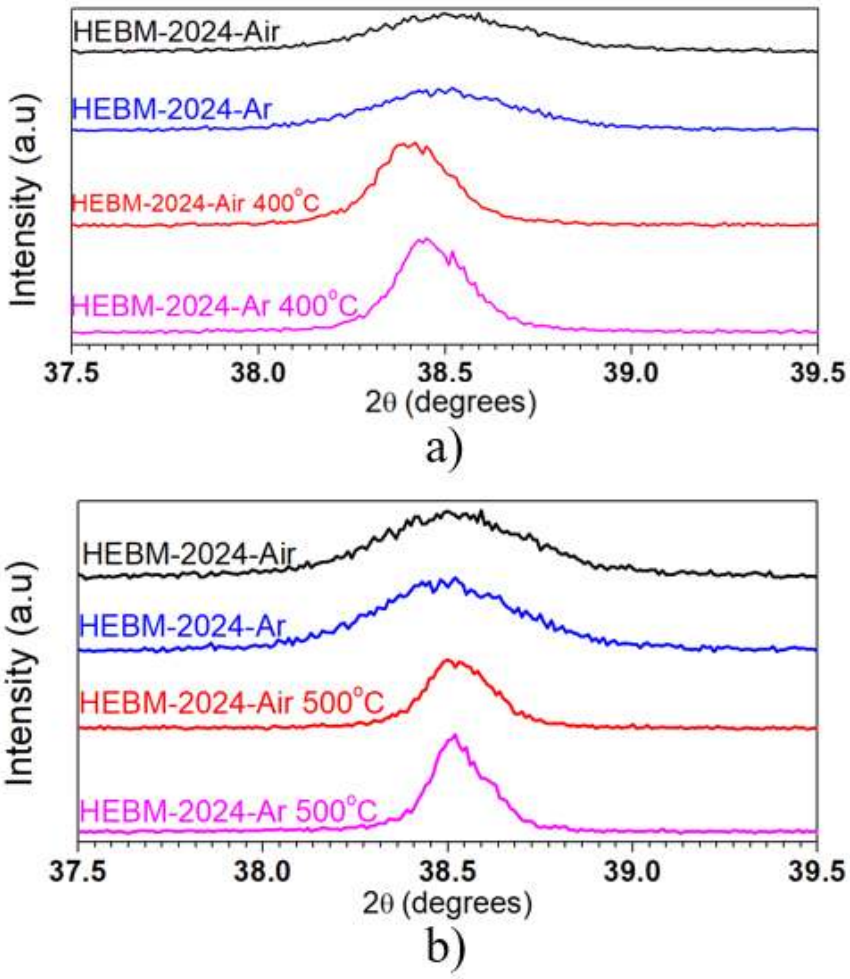

Figure 6.11 Zoomed (111) plane of the XRD scan of a) HEBM-2024-Ar and HEBM-2024-Air after 1 hour heat treatment at 400°C b) HEBM-2024-Ar and HEBM-2024-Air after 1 hour heat treatment at 500°C

Figure 6.12 shows the hardness of HEBM-2024-Ar and HEBM-2024-Air tested after heat treatment at 400 °C and 500 °C for one hour. HEBM-2024-Air maintained the higher hardness than HEBM-2024-Ar at both heat treatment temperatures, which could be considered as further evidence of the higher thermal stability of HEBM-2024-Air due to impeded grain growth by the formation of impurities or dispersoids, which requires further research.

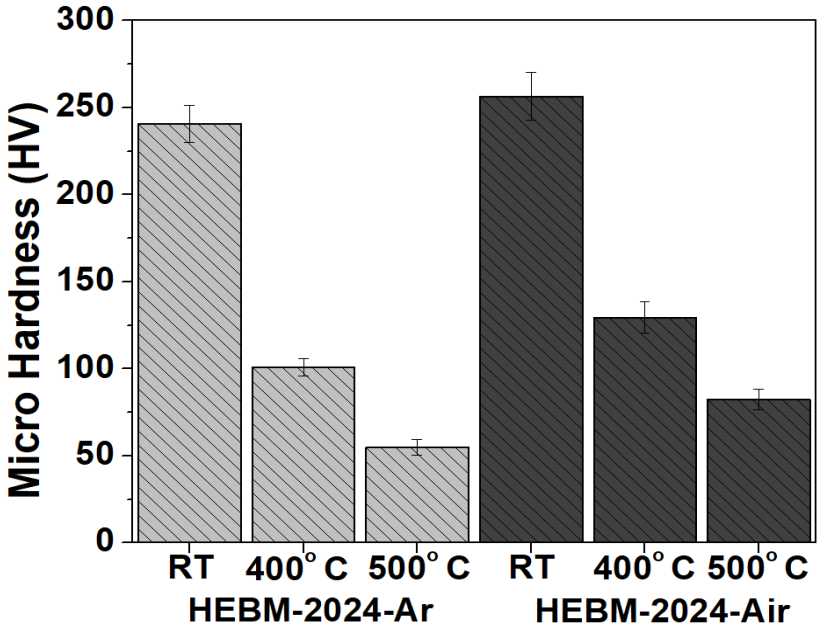

Figure 6.12 Hardness of HEBM-2024-Ar, HEBM-2024-at room temperature (RT), after 1 hour heat treatment at 400°C and 500°C

6.5 Conclusions

High-energy ball milling of AA2024 was successfully performed under Ar and air atmospheres. The hardness and corrosion resistance of AA2024 milled in Ar and air was higher than that of commercial AA2024-T3, which was attributed to the refined microstructure. HEBM in air resulted in higher hardness and corrosion resistance than that in Ar. HEBM in air exhibited improved thermal stability after an isothermal heat treatment at 400 °C and 500°C for one hour. Therefore, high purity milling atmosphere is not necessary to achieve superior hardness and corrosion performance for Al alloys.

CHAPTER 7

INFLUENCE OF COMPOSITIONAL MODIFICATION ON THE CORROSION BEHAVIOR

Present chapter includes the influence of compositional modification by high-energy ball milling. For this purpose, AA2024 which is investigated in previous chapters has been selected. The compositional modifiers are selected for following considerations.

1. The reviewed literature on the corrosion of AA2024 extensively reports the positive influence of corrosion inhibitors. Common examples to corrosion inhibitors used in Al alloys can be given as chromates that provides inhibiting pit initiation by anodic inhibition, and vanadates which are more environmentally friendly compounds and salts of rare metals [151–156].

2. The reviewed literature on high energy ball milled alloys demonstrated that mechanical alloying of Al and V provides outstanding properties such as mutual existence of superior hardness and corrosion performance [9,148].

High-energy ball milling of modified AA2024 with 2 wt.%V and with 2 wt.% $CeNO_3$ is carried out in this chapter.

7.1 Corrosion and hardness of high-energy ball milled modified AA2024 with 2wt.% $CeNO_3$

The Ce in the ion state has an ability to create hydroxide caps on the surfaces where corrosion is occurring. These caps have good coating performance and not easy to eliminate unless an abrasion or chemical dissolution take place [66,151]. In addition, the rate of the dissolved oxygen transportation is restricted due to the abovementioned caps [152].

AA2024 and $CeNO_3$ (2wt%) is high energy ball milled. The $CeNO_3$ (Cerium(III) nitrate hexahydrate) AA2024 and stearic acid is high energy ball milled. The

parameters of milling are kept same as in Chapter 3. Figure 7.1 shows the CPP results of high-energy ball milled AA2024 with and without +2wt%$CeNO_3$.

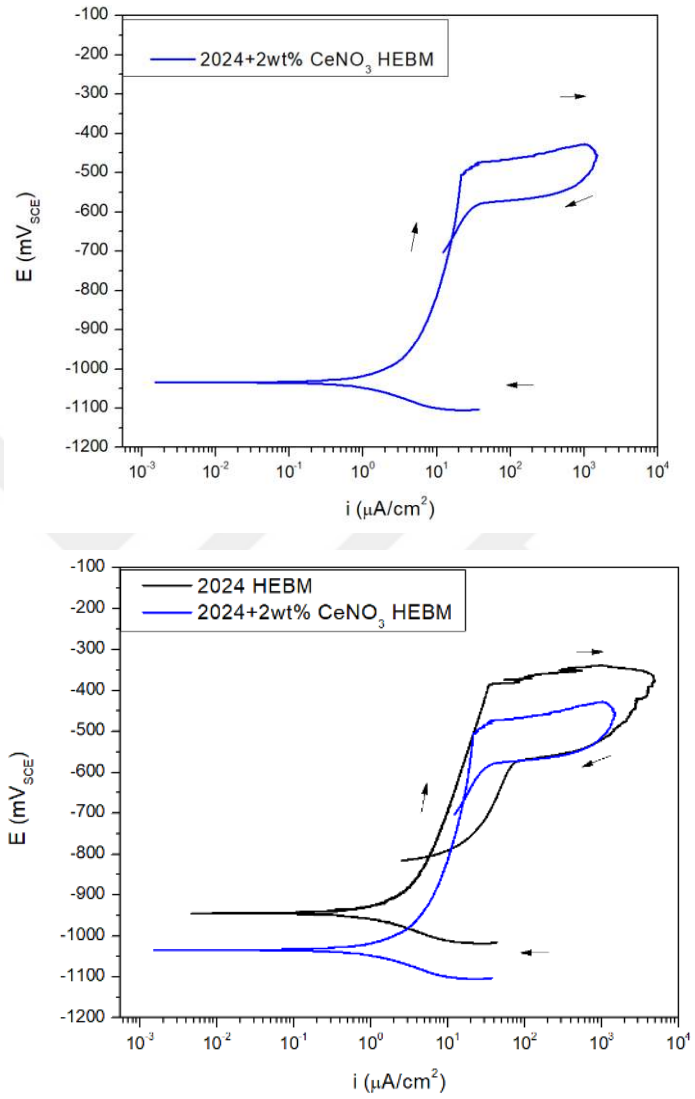

Figure 7.1 CPP results of high-energy ball milled AA2024 with and without +2wt%$CeNO_3$

As it can be seen from Figure 7.1, $CeNO_3$ was not improved the corrosion resistance by means of pitting potential. On the contrary, it deteriorated the pitting response. This is attributed to the chemical form of $CeNO_3$ which was not anhydrous. Therefore, the experiment should be performed with an anhydrous compound which is the scope of future work. However, V addition exhibited a significant increase in the corrosion resistance (Figure 7.2) and especially exhibited repassivation which is quite interesting

and warrants the research attention. Therefore, rest of this chapter focuses on the influence of V addition on corrosion and hardness of high energy ball milled AA2024.

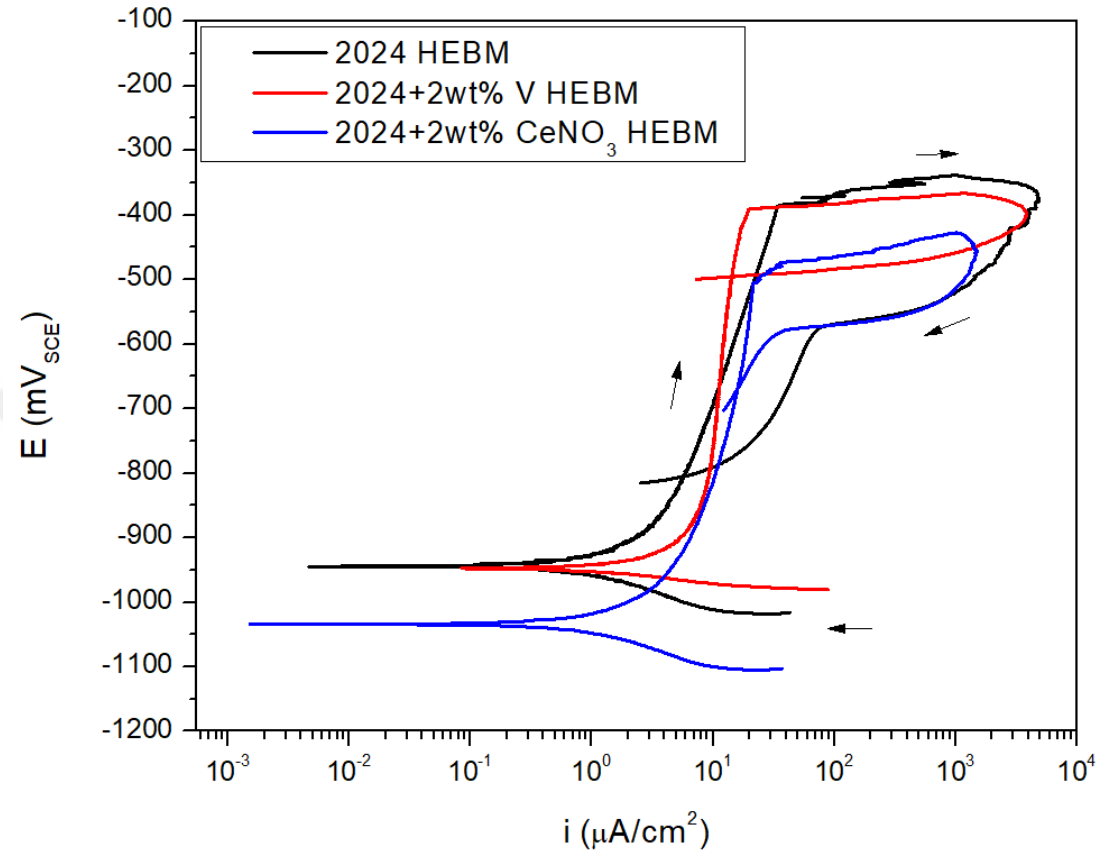

Figure 7.2 CPP graphs for comparison of the influence of compositional modification with V and $CeNO_3$

7.2 Abstract

The effect of V addition on the hardness and corrosion of aluminum alloy 2024 (AA2024) produced by high energy ball milling has been investigated. High-energy ball-milled alloys exhibited enhanced solid solubility of alloying elements and ultrafine grains. The addition of V improved the corrosion resistance of AA2024 alloy, which was attributed to an inhibitory effect caused by the redeposition of V on the cathodic particles in the microstructure. The following part is reproduced in part from [157] with the license provided from John Wiley and Sons.

7.3 Introduction

The combination of high strength and low density makes 2xxx series aluminum alloys critical in many applications, including the automotive and aerospace industries [1,112]. In light of advancing technologies and sustainability concerns, much more is expected from aluminum alloys than just a good strength-to-weight ratio. However, corrosion resistance of high strength Al alloys such as 2xxx alloys degrades after undergoing age-hardening to increase strength [17,22]. Efforts to improve the properties of aluminum alloys by various non-conventional methods that produce a nanocrystalline structure have been reviewed [6,26,38,39,118,158]. Aluminum alloys produced by techniques such as rapid solidification, sputter deposition, ion implantation, high energy ball milling (HEBM), etc., exhibit significantly enhanced properties [6,38].

The HEBM process is known to provide nanocrystalline alloys in powder form that can be consolidated into bulk structures, unlike other processes. Esquivel and Gupta reported significant simultaneous improvements in binary Al alloys with Cr, Mo, Ti, V, etc. as alloying elements [9,47]. The improved properties are attributed to the significant grain refinement and extended solid solubility of the alloying elements, which exhibit extremely low solubility. The proposed mechanisms resulting from the extended solid solubilities are attributed to enrichment of alloying elements in the passive film, increased propensity for re-passivation, release of compounds such as molybdates and vanadates, and reduced galvanic activity between secondary phases and the interacting matrix [9,148].

Corrosion studies on binary Al alloys have shown that V provides an excellent combination of strength and corrosion resistance, so further research has been conducted to investigate the role of vanadium in Al alloys [9,134,148,159]. Most of the work has focused on binary alloys to characterize the influence of alloying elements on corrosion behavior. However, the complex alloy systems are expected to demonstrate dissimilar properties. Esteves et al. investigated the effects of V on the corrosion behavior of high-energy ball-milled AA5083 and reported the positive influence of V addition, which was evident in high pitting and re-passivation potentials

[110]. However, the role of V in alloys in complex microstructures containing a large papulation of cathodic particles has not been investigated yet [65,69,129].

Aluminum alloy 2024 (AA2024) has widely been used in aerospace applications and known to exhibit poor corrosion resistance due presence of cathodic precipitates and constituent particles. Conversion coatings and coating containing corrosion inhibitors such as vanadates have been reported to improve the corrosion performance of AA2024 [24,83,160]. V as an alloying element was detected in AA2219 only in very small amounts (0.05 to 0.15 wt.%) and is considered less effective than zirconium and titanium as grain refining elements [13,17]. On other hand several studies [9,62,134,148] have reported success in producing corrosion resistant Al alloys with high solid solubility of V. Ability of V in suppressing the cathodic activity of Fe rich and C rich particles was attributed to enhanced corrosion resistance [148,161] . Therefore, high energy ball milling of AA2024 alloy with V addition is promising in enhancing the corrosion resistance. In the present study, the microstructure, hardness, and corrosion of the V added high-energy ball milled AA2024 alloy have been investigated.

7.4 Materials and Methods

7.4.1 Material preparation

AA2024 master alloy powder (Valimet, 325 mesh), vanadium powder (325 mesh, 2 wt.%), and stearic acid (1.5 wt.%) as process control agent (PCA) were mixed and placed in a stainless-steel vessel along with stainless steel balls at a ball to powder weight ratio of 16:1. The powder mixture was subjected to high energy ball milling (HEBM) in a Fritsch Pulverizette 7 ball mill for 100 hours at a milling speed of 280 rpm. The milling process was interrupted for 1 hour after each hour of milling in order not to expose high temperatures due to friction. The milling status was checked after each quartet of the milling process. The obtained powder was compacted in a Carver hydraulic laboratory press under 3 GPa of pressure. The diameter of the cold compacted cylindrical samples was 7 mm. The high energy ball milled AA2024 powder and the AA2024 powder with 2 wt.% V are referred to as HEBM-2024 and

HEBM-2024-2V, respectively. Commercial AA2024-T3 alloy were cut into coupons for tests and used for comparison.

7.4.2 Characterization of the microstructure

X-ray diffraction experiments were performed using a Rigaku SmartLab diffractometer. Cu Kα radiation (λ=0.154056 nm) and a graphite monochromator were used for diffraction. The step size was 0.01° and the scan speed was 1 °/min for the scan range from 25° to 85°. The average crystallite size and was calculated after removal of instrumental broadening using the Scherrer equation [162], which was determined using the LaB6 standard. The samples were ground to 1200 grit and polished with a colloidal silica suspension to a surface finish of 0.05 µm. They were then rinsed with ethanol in an ultrasonic bath to clean the surface before being examined at SEM. The SEM investigation was performed in a FEI Verios 460L field emitted SEM equipped with and Oxford energy dispersive X-ray spectrometer (EDS) with an electron landing energy of 20 kV.

7.4.3 Hardness testing

The Vickers hardness of the consolidated alloys was measured using a Mitutoyo hardness tester under a load of 100 g and a dwell time of 10 seconds. The measurements were repeated at least 10 times.

7.4.4 Electrochemical tests

The electrochemical test samples were prepared by cold mounting of copper tape attached consolidated alloys into epoxy resin. The surface of the samples was prepared by grinding to a grit size of 1200 under ethanol. The interface between the sample and epoxy resin was sealed with a fast-curing resin and left in the fume hood for 24 hours to ensure complete cure. Samples were investigated in a Biologic VMP-300 potentiostat using a three-electrode flat- cell, in where the samples as working electrodes, a platinum mesh as counter electrode, and a saturated calomel electrode (SCE) as reference electrode. Cyclic potentiodynamic polarization (CPP) experiments were performed after measuring the open current potential (OCP) for 30 min in 0.6 M

NaCl solution. Polarization curves were retrieved with a scan rate of 1 mV/s from 0.1 V_{SCE} below the corrosion potential (E_{corr}), and the direction of the scan was reversed when the current density reached 1 mA/cm2. The cathodic polarization curves were obtained from +5 mV to -1.5 V with respect to OCP.

7.5 Results and Discussion

7.5.1 Analysis of ball milled powder and alloy microstructure

Backscattered electron (BSE) images of HEBM-2024 powder and HEBM-2024-2V powder are shown in Figure 7.3 a. and Figure 7.3 b., respectively. The particle size distribution of HEBM-2024 powder and HEBM-2024-2V powder are shown in Figure 7.3.c and Figure 7.3.d, respectively. The mean particle sizes were measured to be 15.55 ± 7.76 µm and 8.9 ± 5.65 µm for HEBM-2024 and HEBM-2024-2V, respectively. The morphology of the particles, which was spherical in the initial state, transformed to irregularly shaped particles for both powders due to the HEBM. The addition of V affected the size and distribution of the milled powder. Finer particles are observed with the addition of V, which can be attributed to the increased hardness due to work hardening [126]. Figure 7.3.e and f show the consolidated alloys HEBM-2024 and HEBM-2024-2V, respectively. Apart from the pores, the consolidated alloys exhibit a homogeneous microstructure (higher magnification images are presented in inset), free of coarse intermetallics of both V and other alloying elements of AA2024.

The X-ray diffraction patterns of HEBM-2024 and HEBM-2024-2V are presented in Figure 7.4, which show only the peaks corresponding to FCC Al. Intermetallic peaks of alloying elements or V are not observed, which can be attributed to the extended solubility of alloying elements and the formation of a solid solution. The average grain size of the alloys calculated using the Scherrer equation [162] showed a slight decrease from 26 (±6) nm to 23 (±5) nm with the addition of V, which can be attributed to the inhibited recovery due to the increased solute content [39,126,128]. **Figure 7.5** shows zoomed in regions of the peaks corresponding to (111) plane. The (111) plane of the HEBM-2024-2V shows a shift to higher 2Θ values and thus a change in the solute content of the solid solution. This shift could be due to the difference in the effective

atomic radius of V (134.1 pm) and Al (142 pm). The presence of the smaller V atoms in the solid solution causes contraction of the lattice [163]. The amount of V in the solid solution is calculated by change in the lattice parameter and a constant, which is the lattice parameter change per atomic percent solute in the solid solution. However, this constant is different for each alloy system due to differences in the structure, size, and electronegativity of the atoms. Therefore, the solid solubility of V in AA2024 cannot be calculated because of the large number of alloying elements.

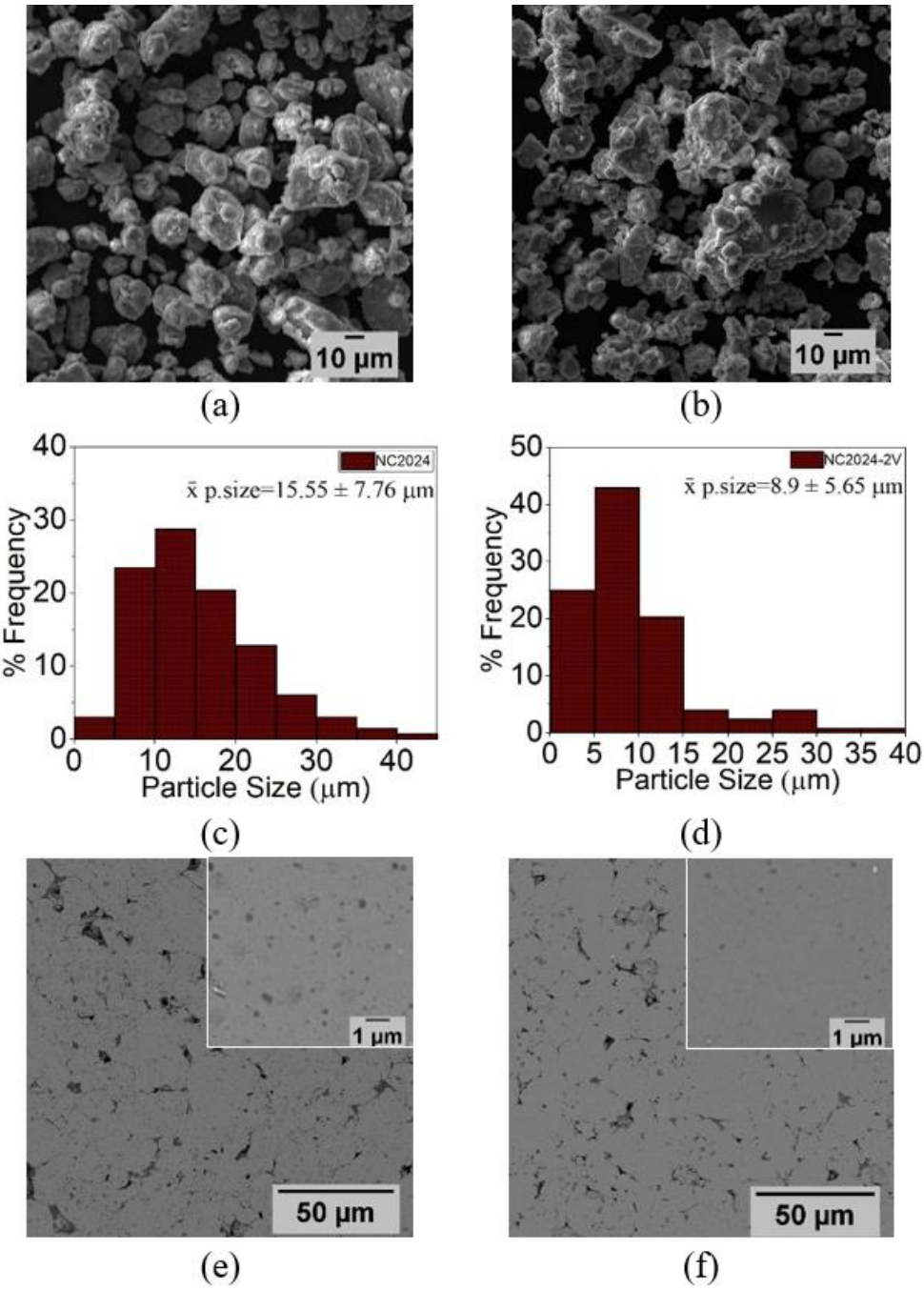

Figure 7.3 Back scattered electron images for (a) HEBM-2024 powder, (b) HEBM-2024-2V powder. Distribution of particle size for c) HEBM-2024 powder and d) HEBM-2024 powder. Back scattered electron images for (e) HEBM-2024, (f) HEBM-2024-2V; corresponding high magnification images are shown in the inset.

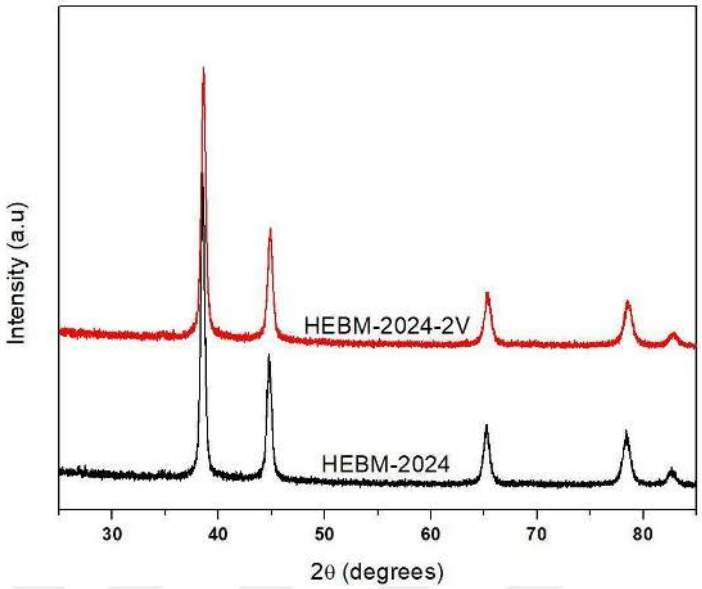

Figure 7.4 XRD patterns of HEBM-2024 and HEBM-2024-2V

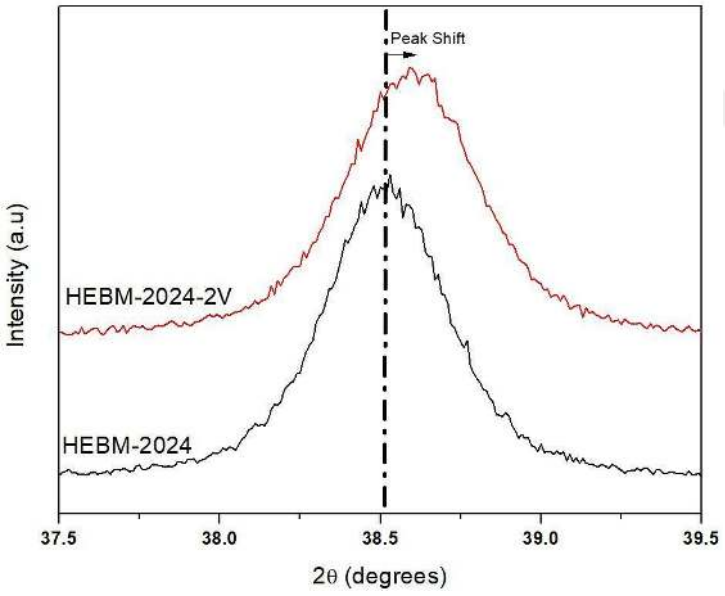

Figure 7.5 Zoomed-in region of the pattern showing peak shift for Al (111)

7.5.2 Corrosion behavior

Representative cyclic potentiodynamic polarization (CPP) curves for the HEBM-2024 and HEBM-2024-2V along with commercial AA2024-T3 alloy plate tested in 0.6 M NaCl electrolyte are shown in Figure 7.6. The electrochemical parameters extracted from the polarization curves are presented in Table 7.1. Both HEBM-2024 and HEBM-2024-2V indicated a passive region. HEBM-2024 and HEBM-2024-2V indicated pitting potential (E_{pit}) of -477 mV_{SCE} and -410 mV_{SCE}, respectively. The passive region and E_{pit} were not observed for AA2024-T3 due to pitting below the OCP [65]. HEBM-2024 showed a repassivation potential (E_{rp}) at about -726 mV_{SCE}, while HEBM-2024-2V showed much higher E_{rp} indicating significant improvement in repassivation due to V addition. The corrosion current density (i_{corr}) of HEBM-2024 and HEBM-2024-2V was similar. However, the cathodic polarization presented in Figure 7.7 indicates a decrease of cathodic current density with V addition compared to HEBM-2024 and AA2024-T3. The decrease in cathodic kinetics could be attributed to the refined microstructure and the decrease in cathodic efficiency of cathodic particles due to V addition.

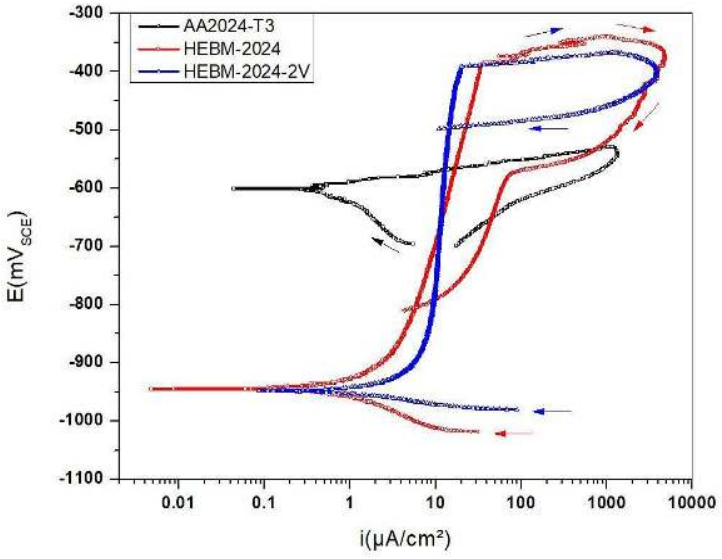

Figure 7.6 Cyclic Potentiodynamic Polarization of HEBM-2024, AA2024-T3, HEBM-2024-2V

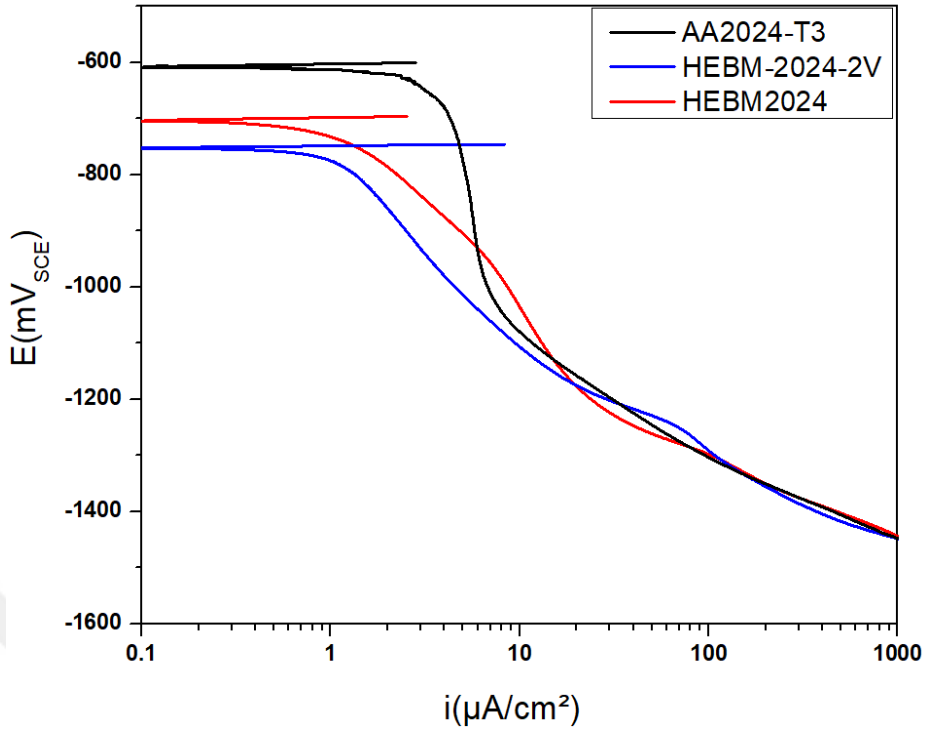

Figure 7.7 Cathodic polarization of AA2024-T3, HEBM-2024 and HEBM-2024-2V

Table 7.1 The average electrochemical parameters and corresponding standard deviations of alloys determined from CPP curves in 0.6 M NaCl at room temperature.

	E_{corr} (mV_{SCE})	i_{corr} ($\mu A/cm^2$)	E_{pit} (mV_{SCE})	E_{rp} (mV_{SCE})	E_{ptp} (mV_{SCE})
HEBM-2024	-990(±95)	0.91 (±0.08)	-477 (±20)	-736 (±10)	-592 (±11)
HEBM-2024-2V	-985 (±85)	0.97 (±0.04)	-410 (±20)	-492 (±5)	-
AA2024-T3	-595 (±18)	3.12 (±0.57)	<E_{corr}	-	-

The enhancement in corrosion resistance of AA2024 by the V addition was confirmed by immersion tests conducted in 0.1 M NaCl solution. The BSE images taken after 2 hours of immersion are shown in Figure 7.8 and the images taken after 14 days of immersion are shown in Figure 7.9. Corrosion initiated around the Fe-containing particles. The matrix showed a microstructure free from large pits. The size and depth of the pits after 14 days of immersion were comparatively less in HEBM-2024-2V.

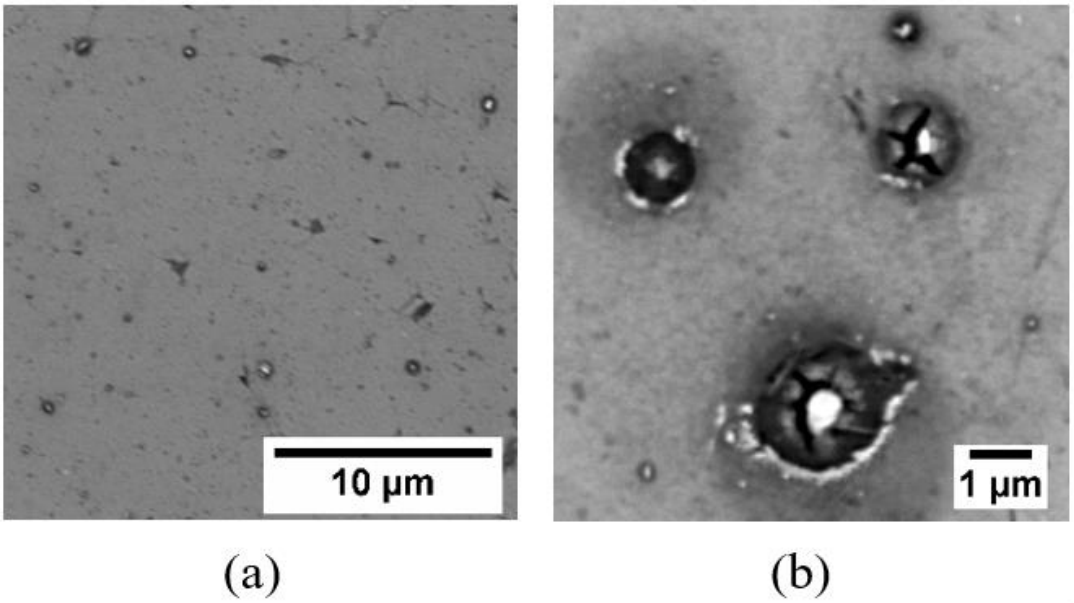

Figure 7.8 BSE images of a) and b) HEBM-2024-2V after immersion in 0.1 M NaCl for 2 hours (without removing corrosion products)

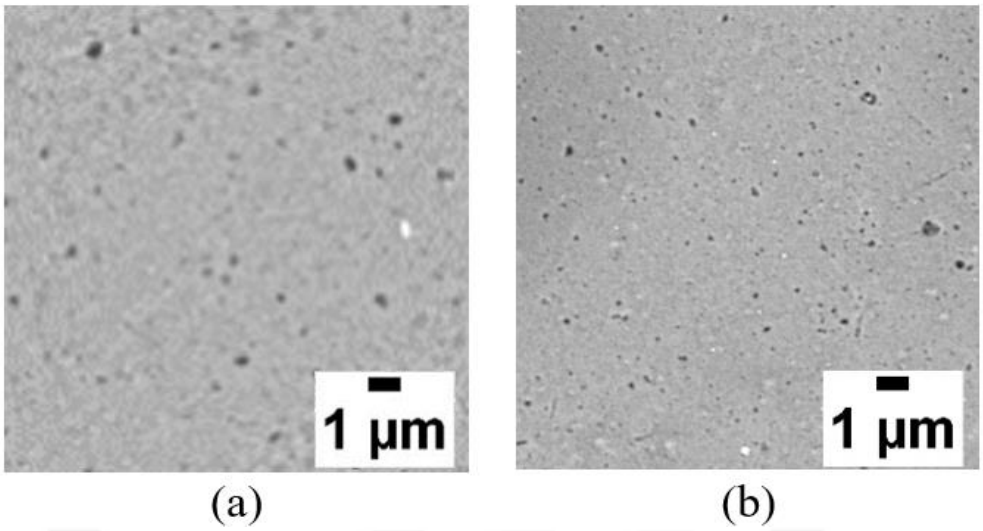

Figure 7.9 a) HEBM-2024 b) HEBM-2024-2V after immersion in 0.6M NaCl for 2 weeks (after cleaning in 30wt% HNO3 solution)

The EDS area maps in Figure 7.10 and Figure 7.11 shows the elemental distribution around a pit in HEBM-2024-2V alloy after 2 hours of immersion in 0.1 M of NaCl . The pit was formed around the Fe rich particle. Figure 7.10 shows that unlike other alloying elements of AA2024, V accumulates around cathodic V rich particle and within the pit.

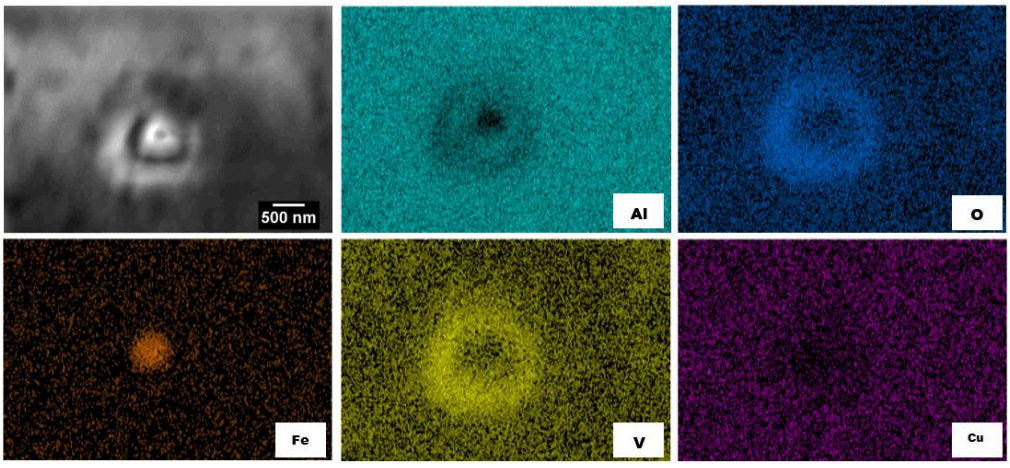

Figure 7.10 EDS Mapping of HEBM-2024-2V alloy immersed in 0.6 M of NaCl Solution for 2 hours.

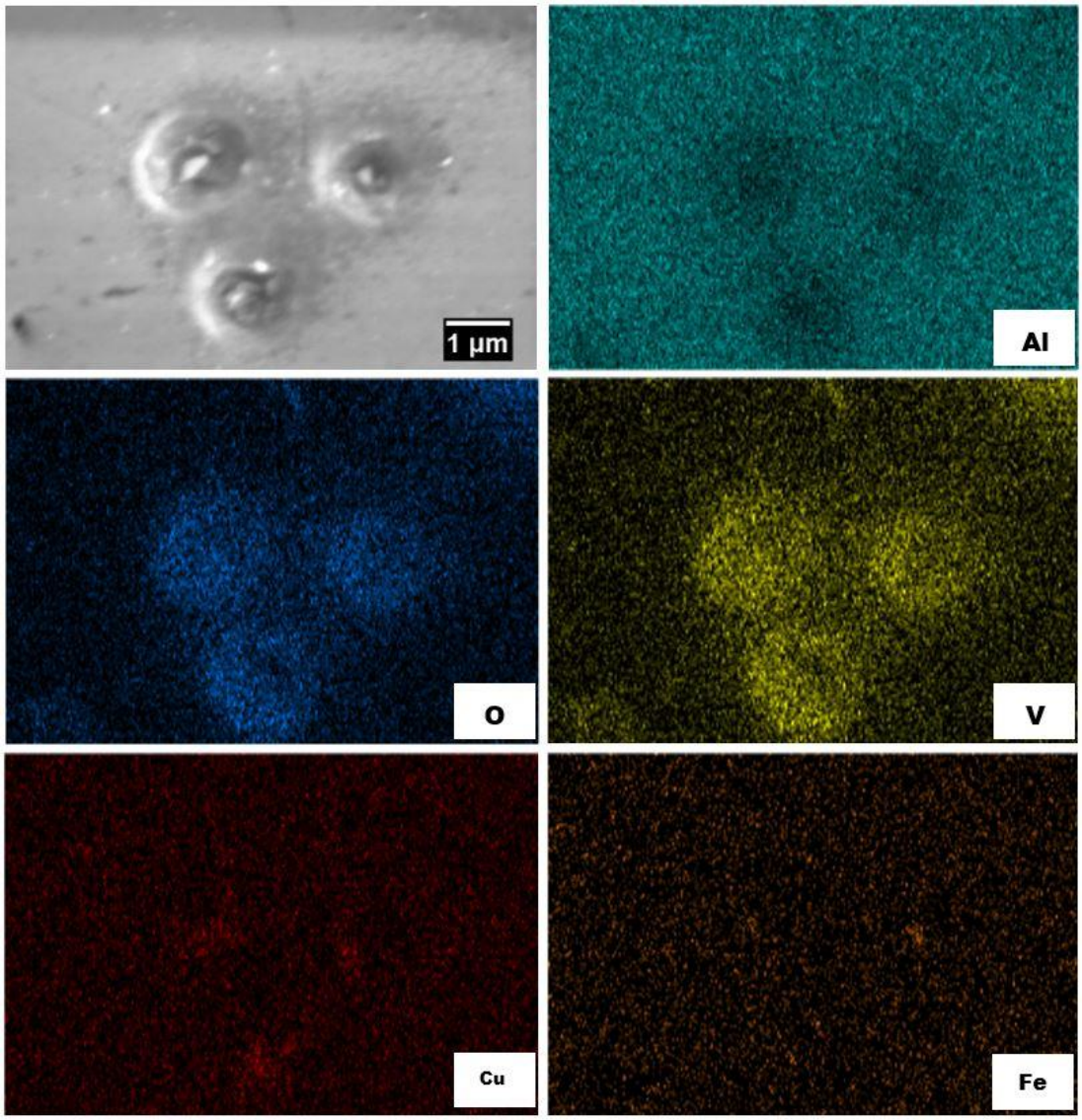

Figure 7.11 EDS Mapping of HEBM-2024-2V alloy (around multiple pit region) immersed in 0.6 M of NaCl Solution for 2 hours.

7.5.3 Hardness

The Vickers hardness values of the alloys along with commercial AA2024-T3 is presented in Figure 7.12. The average hardness of HEBM-2024-2V is ~271 HV which is about twice that of average hardness of AA2024-T3 (~138 HV). This high hardness could be due to the nanocrystalline microstructure, the refined intermetallic compounds, and the extended solubility of the alloying elements, which is consistent with the reported literature on high energy ball milled commercial alloys

[6,65,102,110]. The influence of the V addition can also be seen in the increment of average hardness of HEBM-2024-2V compared to HEBM-2024 (~251 HV). This increase can be attributed to the solid solution strengthening and dispersion hardening caused by V.

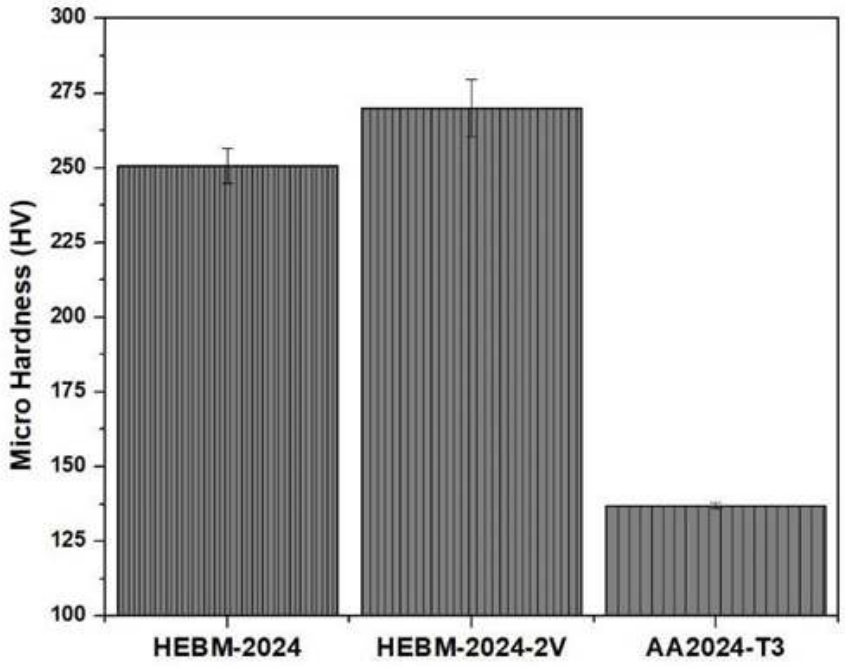

Figure 7.12 Vickers hardness measured for HEBM-2024, HEBM-2024-2V and AA2024-T3

7.5.4 General discussion

The improved hardness and corrosion resistance of HEBM-2024-2V could be attributed to the combined influence of extended solid solubility of V in AA2024 and refined microstructure, as reported [6,38,58,134,139,148]. The improved corrosion resistance in ball milled alloys containing elements like V could be attributed to a) Reduction in the concentration and mobility of point defects due to the incorporation of V into the passive film. b) Repassivation of the alloy due to dissolution of V within pit and subsequent deposition of V on the cathodic particles. X-ray photoelectron spectroscopy and Mott-Schottky analysis in Al-V alloys revealed the presence of oxidized V (V^{+3},V^{+4},V^{+5}) within the passive film and decrease in point defect

concentration [110,148,161]. Witharamage et al. [148] have analyzed pits formed in an in situ consolidated Al-V alloy and reported the deposition of V on cathodic Fe rich particles. Similarly, Christudasjustus et al. [161] reported the deposition of V on cathodic C-rich phases, which were considered to result in high corrosion resistance. In the present study, accumulation of V in the pits around Fe rich particles (Figure 7.10) indicates the release of V within the pit, which could subsequently deposit on Fe rich particle, decrease the cathodic activity and lead to repassivation. The improved corrosion resistance by V addition could be similar to corrosion inhibition mechanism of vanadate inhibitors for Al alloy [164]. In summary, V addition to commercial Al alloys through high-energy ball milling could produce alloys with high strength and corrosion resistance, which are also capable of releasing inhibitors on demand [165] or in-situ coatings [166].

7.6 Conclusions

The influence of V addition on the hardness and corrosion of AA2024 produced by high energy ball milling was investigated. The main conclusions can be summarized as follows:

- The alloys produced by high energy ball milling and subsequent consolidation by cold compaction exhibited a uniform microstructure and were free of coarse constituent particles.

- The V addition enhanced the hardness of AA2024. The addition of 2 wt. % V resulted in an increase hardness of ~%10.

- The V addition resulted in a nanocrystalline AA2024 capable of repassivation when polarized in a 0.6 M NaCl electrolyte and showed a ~35% increase in repassivation potential compared to nanocrystalline AA2024 without V addition.

- The improved corrosion resistance with V addition has been attributed to the extended solid solubility of the V which lead to formation V-ions within the

pits. The deposition of V on cathodic particles suppressed cathodic reaction and enhanced the repassivation ability.

CHAPTER 8

CORROSION BEHAVIOR OF BINARY AL-M ALLOYS PRODUCED BY HIGH ENEGY BALL MILLING

This chapter includes the corrosion performance of the binary Al-M alloys, which are not reported in the reviewed literature. Four elements, including a rare earth and transition metals were selected for following considerations,

1) Transition metals have significantly low solubility in Al. There are many transition metals including Cr, Mo, Si, Ni, Ti, V, Nb, Mn have been mechanically alloyed with Al and tested for corrosion investigation in the reviewed literature [37,38]. There is a gap in the transition metal elements and Y, Zr and Fe could be suitable candidates.

2) The results of the previous chapters have illustrated that Fe is present in the microstructure more than initial composition due to abrasion of milling media. In addition, pitting corrosion is observed around the cathodic Fe-rich particles in the ball milled alloys. Therefore, a supersaturated Al-Fe matrix could be less detrimental to pitting due to potentially diminished galvanic activity in between matrix and particles. Furthermore, Fe is an impurity for Al alloys, and it is a burden to refine Fe content in many cases. Hence, recycled alloys where Fe content is accumulated after each cycles that includes thermomechanical treatments. There are many works reporting the mechanical response of high energy ball milled Al-Fe alloys. However, corrosion behavior is not well understood and warrants further research.

3) Rare earth elements are known to be added to Al and some of them have shown excellent properties [61,68,94,167,168]. The influence of rare earth elements as alloying element is vast and requires investigation. Furthermore, supply and safety are important considerations for rare earth elements. Therefore, La is selected as an alloying elements.

8.1 Results on Binary Al alloys

The experimental section is covered in 8.2.3. Out of 25 g alloy powder, only 3.4 and 5.7 g alloy powder were recovered for Al-5at%La and Al-5at%Y, respectively. The rest of the materials was chunky bulk materials that were cold welded to vials. The BSE microstructures for Al-5Zr, Al-5Y and Al-5La are presented in Figure 8.1-3.

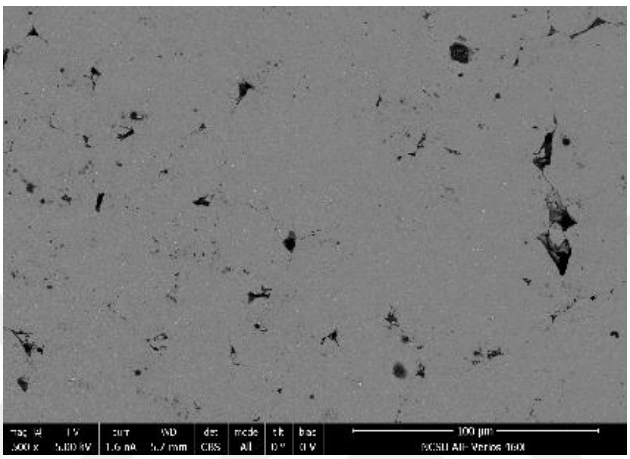

Figure 8.1 BSE image for Al-5La

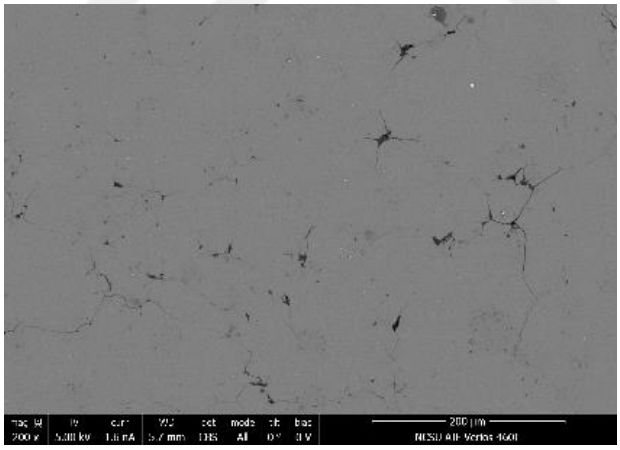

Figure 8.2 BSE image for Al-5Y

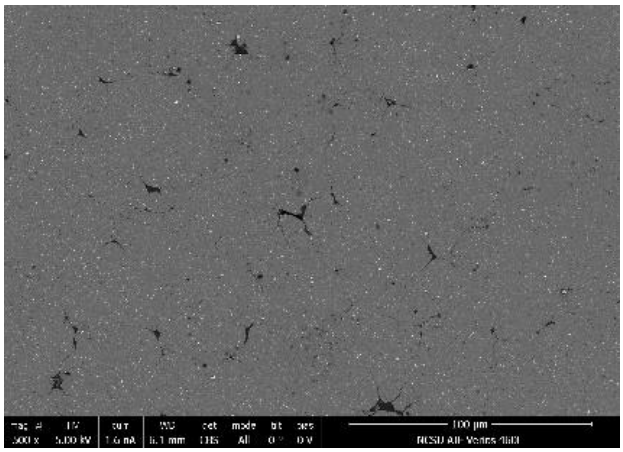

Figure 8.3 BSE image for Al-5Zr

The consolidated alloy microstructures exhibited homogenous distribution but in higher amount of secondary phase particles that is attributed to low level of solute solubility. On the contrary, Al-5Fe alloy exhibited significant solid solubility that is further verified in chapter 8.2.3. In addition, comparison of hardness (Figure 8.4 Hardness of Al-5at. % Y, La, Zr and Fe and CPP test results (Figure 8.5) demonstrated that Al-5at.%Fe is not only superior to abovementioned alloys but also has superior hardness to any alloy of produced with same condition in the literature along with outstanding corrosion resistance. Therefore, the Al-5Fe system is extensively investigated for the rest of this chapter.

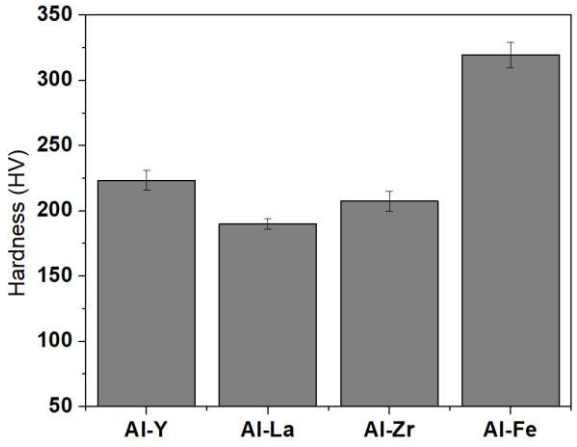

Figure 8.4 Hardness of Al-5at. % Y, La, Zr and Fe

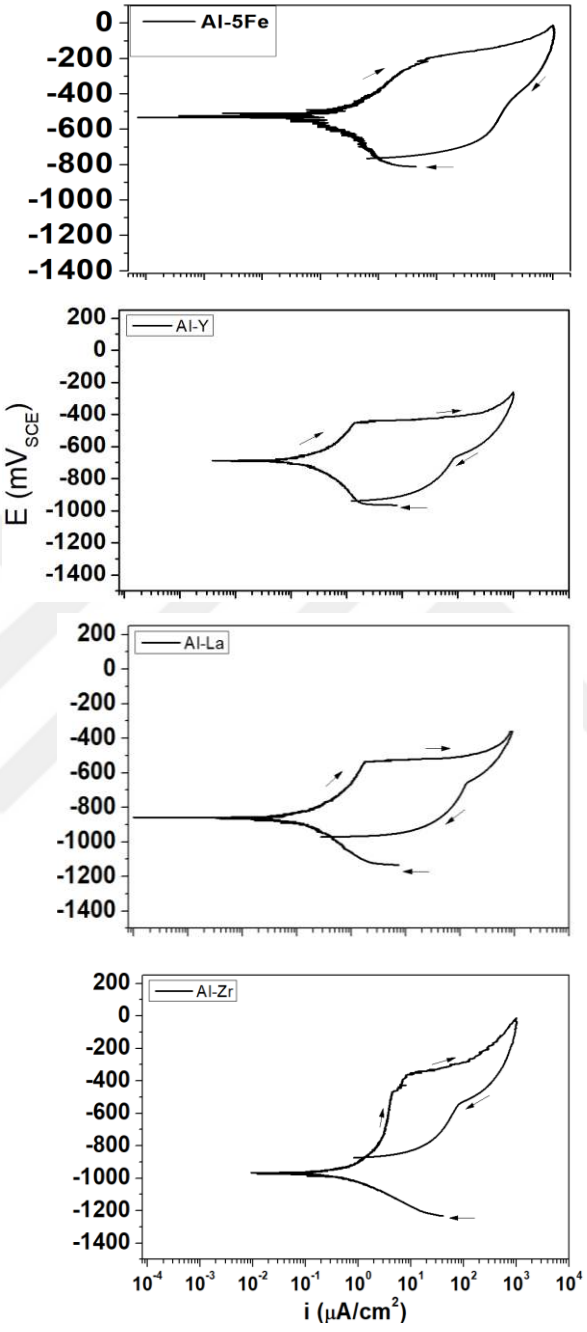

Figure 8.5 CPP curves of Al-5at% Y, La, Fe and Zr tested in 0.1 M NaCl

8.2 Corrosion behavior of a bulk nanocrystalline Al-Fe alloy

8.2.1 Abstract

Nanocrystalline Al-Fe alloy, with uniform microstructure and high solid solubility of Fe, has been produced by high-energy ball milling. Cyclic potentiodynamic polarization tests revealed high pitting potential. Hardness and corrosion resistance of the Al-Fe alloy were higher than any commercial Al alloy. High hardness and corrosion resistance were attributed to the nanocrystalline structure and formation of solid solution. X-ray photoelectron spectroscopy, secondary ion mass spectrometry, and scanning transmission electron microscopy indicated the incorporation of Fe to the surface film and Fe enrichment at the alloy/surface film interface, which were attributed to the enhanced corrosion performance.

8.2.2 Introduction

The increasing demand for high-strength and low-weight alloys has led to a wide variety of aluminum alloy applications. Iron (Fe) is generally undesirable and the most common impurity in aluminum alloys [169], which forms secondary phases due to extremely low solid solubility- a maximum ~0.025 at.% at 655 °C [170]. However, Al alloys with high iron content could be auspicious considering the cost and efforts being made to refine Fe content. Considering the abundance and low cost of Fe, few studies reported of introducing the secondary phases intentionally to enhance the high temperature performance owing to the high melting temperature of Al-Fe intermetallics [171]. However, these brittle Al-Fe intermetallics have significantly limited the plastic deformation capability [172] and deteriorated corrosion resistance due to galvanic interactions with the Al matrix [77]. Therefore, exploring new techniques that reverse the deleterious effects of iron in aluminum while preserving the benefits of it is of great merit.

Various techniques, including rapid solidification [67], additive manufacturing [173,174], and severe plastic deformation techniques [172,175–179], have been

proposed to synthesize Al-Fe alloys with modified microstructures. High-energy ball milling (HEBM) is a proven technique for homogenizing the microstructure by uniform dispersion of constituent particles and increased solid solubility of alloying elements [35]. The vast majority of the studies on high-energy ball milled Al-Fe alloys investigated the microstructure and mechanical properties. Sasaki et al. reported the significant grain refinement in mechanical alloyed Al-5at.%Fe alloys whose matrix consists of refined intermetallic constituents such as Al_6Fe and $Al_{13}Fe_4$ [175,180]. The alloys are reported to have compressive strengths exceeding 1 GPa with high ductility. Nayak et al. reported the increasing hardness with increasing Fe content in Al-Fe alloys due to formation of $Al_{13}Fe_4$, a large number of defects during the alloying process, and absence of soft Al phase [176]. Mukhopadhyay et al. reported the dissolution of 4.5 at.% Fe in Al matrix by mechanical alloying for 20 h [172]. It should be noted that solid solubility of Fe in Al at room temperature is negligible.

Aluminum alloys, unlike pure aluminum, exhibit poor corrosion resistance due to the micro galvanic interaction of heterogeneities in the microstructure, which leads to the breakdown of the protective passive film and promotes localized corrosion [13]. Iron has an extremely detrimental effect on corrosion because it is present in the form of cathodic constituents such as Al_3Fe, although it is present in the composition in relatively small amounts [77]. In addition, iron may also be present in the form of more detrimental compounds such as AlCuFeSi, Al_7Cu_2Fe, AlCuFeMn, AlFeMnSi in the high-strength aluminum alloys [69,70,72,82,84]. Since the corrosion of aluminum alloys strongly depends on their microstructure, nanocrystalline alloys are expected to have different corrosion properties due to their refined microstructure. Mechanical alloying is a promising method for the formation of nanocrystalline alloys, among the techniques that can provide modified structures and thus aid in a significant enhancement in corrosion resistance [35,38]. Recent studies on nanocrystalline Al alloys produced by high-energy ball milling have demonstrated the possibility of simultaneous improvement in strength and corrosion [7,9,47,55,65,102], where Al-Cr [46,101], Al-V [148], Al-Mo, Al-Nb, Al-Mn, Al-Ti, Al-Si [9,47] alloys prepared by high-energy ball milling exhibited enhanced strength and corrosion performance than commercial Al alloys. Additionally, the corrosion performance was attributed to the

improved solid solubility of the corrosion-resistant elements within the Al matrix, which provided solute enrichment at the metal/film interface, increased propensity for re-passivation, release of inhibitory compounds, and increased vacancy annihilation in the passive film [38,148,161].

The abovementioned literature reports the presence of iron and iron-containing intermetallics in the high-energy ball milled aluminum alloys. The source of iron in these works is attributed to either iron impurities in the material or possible contamination from hardened stainless-steel milling media [9,35,39,181]. However, understanding the role of the Fe contamination on the microstructure and corrosion characteristics of ball milled alloys attracted limited attention. Moreover, iron restricts the widespread use of aluminum alloys, especially in recycled aluminum, where the iron content accumulates after each recycling step. It has been shown that the detrimental effects of iron could be reduced by controlling the intermetallics. For example, fast solidification rates in Al-Fe alloys have resulted in high corrosion resistance [67]. Therefore, understanding the corrosion, microstructure, and mechanical properties of ball milled Al-Fe alloys is of great importance for the development of new Al alloys, reducing costs, and improving recyclability, since recycling of the Al is considered critical for sustainability [182,183].

The corrosion and strength of a nanocrystalline Al-Fe alloy have been investigated in this study. The role of iron as an alloying element in the high-energy ball milled Al-5at.%Fe alloys was investigated in terms of corrosion and strength and compared with pure Al and Al-5at.%M alloys (M: Si, Cr, Ti, Mn, Ni, Mo, V, Nb) prepared with the same experimental parameters reported in the literature [9]. The role of microstructure and passive film was investigated and discussed to evaluate the mechanisms and effectiveness of iron in improving the corrosion resistance and strength of the Al-5at.%Fe alloy.

8.2.3 Experimental

8.2.3.1 Alloy production

Al-5at.%Fe alloy powder was mechanically alloyed in a Fritsch Pulverisette 5 ball mill. Gas atomized aluminum powder (99.7% purity) and iron powder (5 at.%) were weighed in a high purity argon atmosphere within a glovebox. The powder mixture was placed in hardened stainless-steel containers and sealed inside the glovebox along with the following elements: Stainless-steel balls with a diameter of 10 mm and a ball to powder weight ratio of 16:1, 1.5 wt.% stearic acid as a process controlling agent (PCA). Mechanical alloying was conducted for 100 hours at a rotation speed of 280 rpm. Ball milling process was programmed with a one hour pause after each hour of milling operation to eliminate problems due to overheating. The milling status was examined to check the powder structure in the glovebox after every quartet of the milling operation. The milled Al-5at.%Fe powder was then consolidated into the 7 mm diameter pellets with 3 mm thickness through compaction at laboratory ambient temperature. 3 GPa of single-ended pressure was applied for 10 minutes on each specimen. The cold compacted cylindrical pellets are referred to as Al-5Fe alloy in this manuscript.

8.2.3.2 Characterization

The Scanning Electron Microscopy (SEM) was performed in a FEI Verios 460L field emission SEM equipped with an Oxford energy dispersive X-ray spectrometer with an electron landing energy of 20 kV. Specimens for Transmission Electron Microscopy (TEM) investigation were prepared in a ThermoFisher Quanta 3D FEG, a Focused Ion Beam and Scanning Electron Dual- beam Microscope (FIB-SEM). Specimens were protected with a platinum coating to avoid surface damage from ion implantation and irradiation. A landing voltage of 30 kV with various beam currents was utilized to monitor the specimen. Cross-section lift-out with an approximate thickness of 1–2 µm of lamella was performed by an omniprobe manipulator. Further thinning and contamination cleaning were carried out after placing the lamella on a TEM grid. TEM specimens were stored under vacuum after final polishing until TEM investigation in

a Thermofisher Talos F200X Field Emission Gun Scanning Transmission Electron Microscope (S/TEM) operated at 200 kV.

X-Ray Diffraction (XRD) investigation was carried out in a Rigaku SmartLab diffractometer equipped with a graphite monochromator. XRD pattern scanned in the range of 25 to 85 2θ with a scan speed of 1°/min and step size of 0.01°. The average grain size was calculated by Scherrer`s equation after eliminating the contribution of instrumental broadening of which determined using LaB_6 standard.

Vickers hardness of the alloys was obtained using a Mutitoyo hardness tester with a 100 g applied load and 10 s of dwelling time. The hardness tests were carried out at least 10 times to calculate the average Vickers hardness.

8.2.3.3 Post corrosion surface characterization

X-ray photoelectron spectrometry (XPS) analysis was carried out to investigate the oxide film developed on the alloy surface. Samples were polished to 0.05 µm using colloidal silica and immersed in 0.1 M NaCl solution for 2 hours. The oxide film investigation was conducted on 2x2 mm scan area with a 60˚ take-off angle. Instrument chamber pressure was kept below 10^{-9} mbar and Mg anode was used as the X-Ray source of 300 W. CASA software was utilized to analyze XPS data and the background was eliminated using the Shirley function.

Time-of-flight secondary ion mass spectroscopy (ToF-SIMS) was performed to obtain elemental depth profiling on Al-5at%Fe 2hr immersed specimen in 0.1 M NaCl solution. The pressure of the main chamber inside the instrument was maintained below 10^{-9} mbar. Primary ion source of Bi^{3+} with 25 keV and 0.35 pA target current was rastered over 100 x 100 µm area. Cs^{+} ion beam was used to sputter the surface with 1 keV and 7.2 nA current over 150 x 150 µm area.

8.2.3.4 Electrochemical tests

Specimens were cold mounted into the epoxy resin and were ground with SiC emery paper to 400-600-800 grit under running water before the final grinding step of 1200 grit under ethanol. The interface between the metal and epoxy resin was sealed with a quick set epoxy resin to eliminate possible crevice corrosion. The samples were kept in a fume hood for 24 hours prior to the electrochemical tests. Electrochemical tests were carried out in a conventional three-electrode flat-cell where a platinum mesh was used as a counter and a saturated calomel electrode (SCE) was used as the reference electrode. Electrochemical test was carried out using a Biologic VMP-300 multichannel potentiostat connected to a computer with EC-lab software. Electrochemical tests that performed in 0.01 M NaCl electrolyte. The open-circuit potential (OCP) was measured for 20 min after immersing the working electrodes to electrolyte. The CPP scans were obtained with a scan rate of 1 mV/s from 0.250 V_{SCE} below the OCP. Reverse scans were performed until the anodic current density reached to 200 $\mu A/cm^2$. All the CPP tests were repeated at least three times to ensure reproducibility.

8.2.4 Results and Discussion

Backscattered electron (BSE) images of the high-energy ball milled and subsequently consolidated Al-5Fe alloy are shown in Figure 8.6.a. Consolidation was possible because of plastic deformation at the interparticle boundaries resulting in mechanical bonding. However, porosities were visible due to highly hardened particles with irregular shape. The high magnification SEM image (Figure 8.6.b) shows a homogeneous microstructure free of coarse intermetallics. The BSE images and EDS analysis demonstrated the uniform dispersion of iron within the aluminum matrix along with refined bright iron-rich particles.

The STEM Dark field (DF) image of the Al-5Fe alloy is shown in Figure 8.6.c, along with the estimated grain size distribution presented in Figure 8.6.d. Figure 8.6.c shows

the presence of nano-sized grains in the microstructure. The distribution of the grain size indicated a right skew and a mean grain size of 19.1 nm, indicating that the vast majority of the grains are below 20 nm. The selected area diffraction (SAED) pattern (Figure 8.6.e) confirmed the alloy to be to be FCC Al (PDF Card −00 to 004–0787_Al) [116]. The lattice parameter through the (111) plane in the SAED pattern was calculated 4.0369 Å, while the lattice parameter for pure Al is 4.0495 Å. The decrease of the lattice parameter indicates the existence of smaller iron atoms in the substitutional lattice sites of aluminum. It can therefore be attributed to the formation of a supersaturated solid solution of iron in aluminum as a result of HEBM [184].

The X-ray diffraction patterns of the Al-5Fe alloy and pure Al are shown in Figure 8.6.f. The XRD pattern shows all the characteristic peaks of Al in both samples, and the Fe-containing phases are not detected in the scan. This can be attributed to the combined effects of the increased solid solubility and the phases falling below the detection limit of the XRD. The XRD pattern shows a shift of the peaks towards higher 2θ values compared to pure Al. For example, the (111) peak of the Al-5Fe alloy is shifted to 38.589° from 38.472°, and the lattice parameter of the Al-5Fe alloy decreased from 4.0495 Å to 4.0377 Å. This shift was attributed to the increased solubility of iron and the formation of an Al-Fe solid solution. The estimated solid solubility of iron in aluminum is calculated with reference to the published literature [172], which gave an estimated solid solubility of iron in aluminum to be ~2.53 at.%, while using the data from the TEM investigation gave an estimated solubility of ~2.61 at.%. The data from the XRD and TEM studies agree well and indicate the supersaturated solid solution of aluminum and iron. This increase in the solid solubility can be attributed to intense plastic deformation that resulted from the ball milling, causing defects such as grain boundaries and increased dislocation densities [114]. The defects when combined with local stresses, pave the way for the incorporation of iron into the structure and consequently substitution by Al atoms [114,184]. Significant peak broadening was observed in the Al-5Fe alloy, which can be attributed to grain refinement and lattice strain due to the ball milling. The peak broadening was used to calculate the average grain size, which was 18.1 nm, similar to the value estimated using TEM. In close agreement, the XRD and TEM studies revealed a nanocrystalline

structure and significantly increased iron solubility, which has a maximum solubility of 0.025 at.% at 655 °C and negligible solubility at room temperature [1].

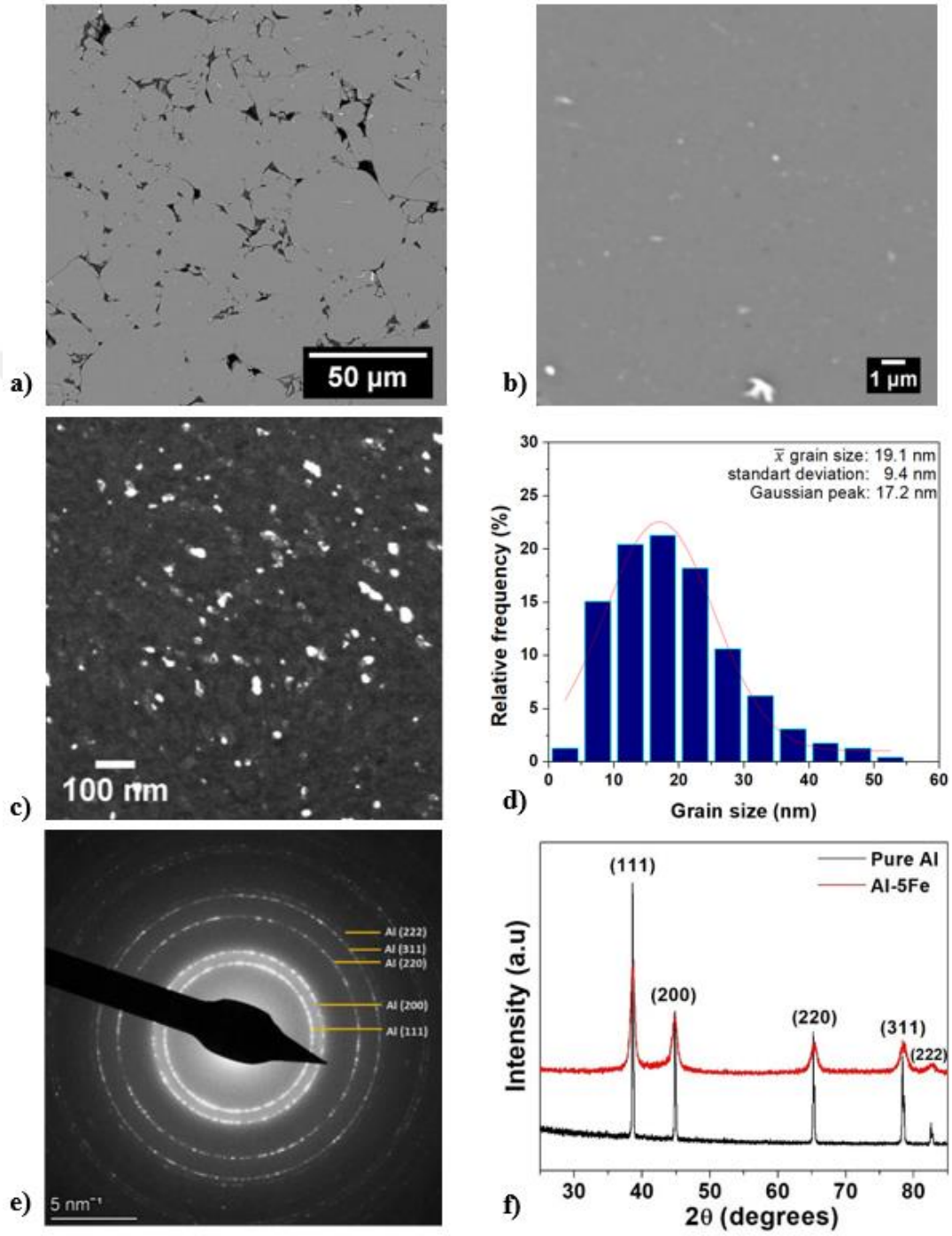

Figure 8.6 Microstructural characterization of Al-5Fe alloy. a) BSE image of cold compacted Al-5Fe alloy b) High-magnification BSE image of Al-5Fe Alloy c) STEM-DF micrograph of Al-5Fe alloy d)

Grain size distribution, estimated from the image presented in Figure 8.2 e) SAED pattern of the Al-5Fe alloy f) XRD pattern of Al-5Fe alloy and Pure Al for the comparison.

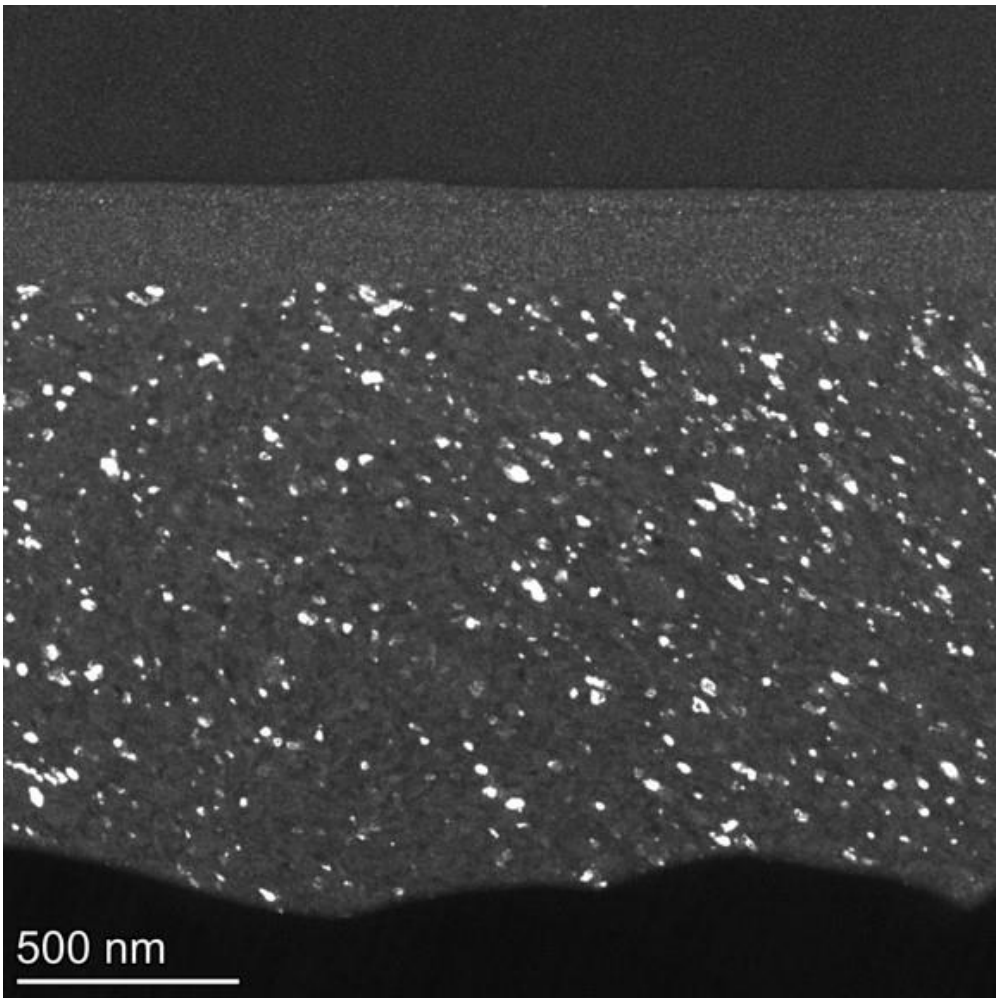

Figure 8.7 TEM-DF image used for grain size estimation

Representative cyclic potentiodynamic polarization curves of the Al-5Fe alloy along with pure Al are shown in Figure 8.8.a. The experimental parameters and conditions were selected with reference to the work of Esquivel et al. [9] for the comparison of Al-5Fe alloy with Al-5M (M: V, Mo, Nb, Cr, Si, Ti, Mn) alloys that were produced and characterized under the same conditions. The CPP curves show the effects of the iron addition on the corrosion behavior. The anodic current density of the Al-5Fe alloy

was significantly lower than that of pure Al, which can be attributed to the presence of a passive film on the alloy surface. A significant passive region was observed in the polarization curves of the Al-5Fe alloy. The pitting potential (E_{pit}) at the breakdown of the passive film of the Al-5Fe alloy was significantly nobler (390 mV higher) than that of pure Al. The transition potential (E_{tr}) of the Al-5Fe alloy was 295 mV higher than the E_{tr} of pure Al. The E_{pit} and E_{tr} values for the tested alloys and for the Al-5M alloys are presented in Figure 8.9. The pure Al and nanocrystalline Al (NC Al) are also included in Figure 8.9. The nobler pitting potential means more resistance against pitting corrosion. E_{tr} indicates the ability of the alloys to repassivate after passive film breakdown. The influence of high-energy ball milling is clearly revealed in the comparison of NC Al with pure Al. The Al-5Fe alloy showed an increase in corrosion resistance, where E_{pit} and E_{tr} of Al-5Fe were nobler than Al-5Mn, Al-5Ti, Al-5Si, and Al-5Cr. Considering E_{pit}, the corrosion resistance of the Al-5Fe alloy ranked after Al-5V, Al-5Mo, and Al-5Nb alloys.

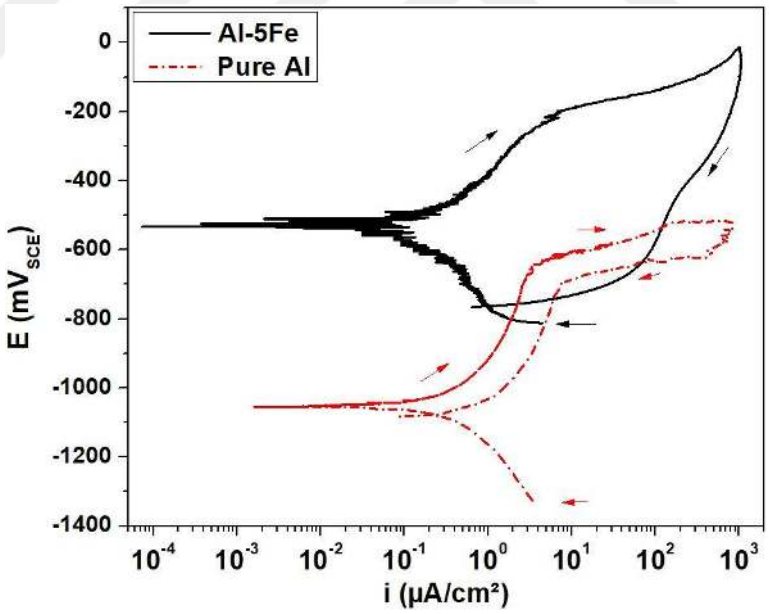

Figure 8.8 Representative CPP curves of Al-5Fe alloy and pure Al for the comparison in a 0.01 M NaCl electrolyte

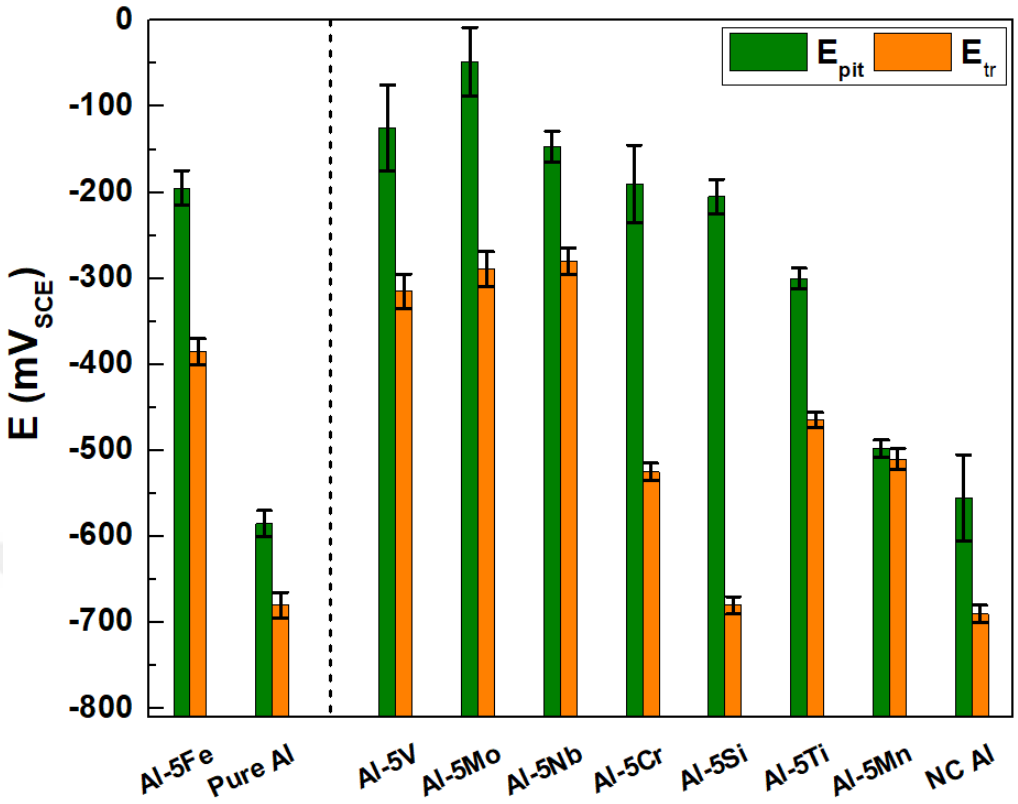

Figure 8.9 E_{pit} and E_{tr} for Al-5Fe alloy in comparison with E_{pit} and E_{tr} for HEBM Al-5M (M: V, Mo, Nb, Cr, Si, Ti, Mn with 5 at.%) and nanocrystalline aluminum (NC Al) [37].

The post-corrosion characterization of the Al-5Fe alloy was further investigated to analyze the pitting behavior and initiation of corrosion after immersion tests in 0.1 M NaCl. Surface examination by SEM and EDS was performed to analyze the pitting behavior and initiation of corrosion. The BSE image of the Al-5Fe alloy immersed in 0.1 M NaCl is shown in Figure 8.10.a. The size, and morphology of the pits are in accordance with the high-energy ball milled alloys, which can be attributed to a homogeneous microstructure [9,65]. The zoomed image with EDS mapping (Figure 8.10.b) shows that the pit is formed in the form of trenches initiated by the Fe-rich particle, which is cathodic to the matrix. The lack of coarse Fe intermetallics and constitutional particles resulted in high corrosion resistance as confirmed by potentiodynamic polarization experiment.

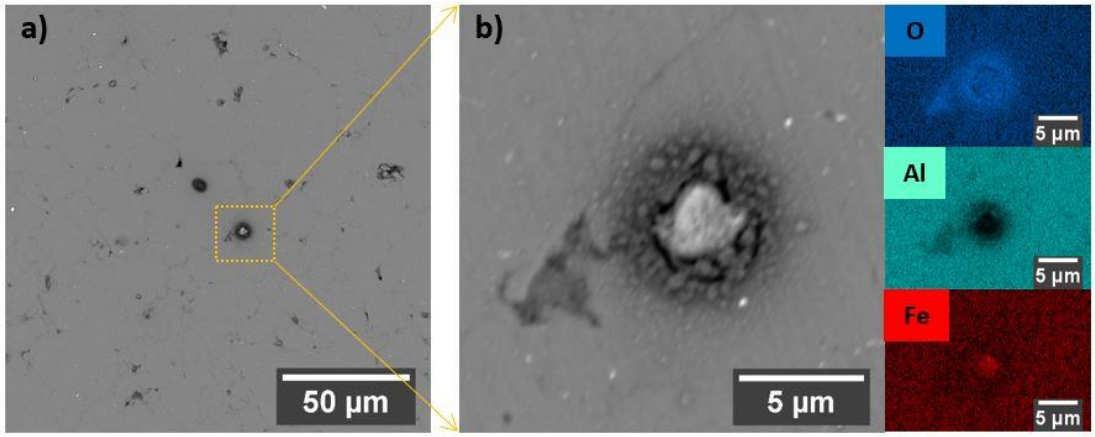

Figure 8.10 a) SEM-EDS micrographs (BSE) of the Al-5Fe alloy immersed in 0.1 M NaCl solution for 2 hours b) Higher magnification image of the region shown by yellow box with EDS mapping.

The surface film investigation of the Al-5Fe alloy by ToF-SIMS is presented in Figure 8.11. The negative ion intensities versus sputter time for the Al-5Fe alloy is plotted in Figure 8.11. The SIMS analysis for the Al-5Fe alloy shows the depth profiles for OH^-, $^{18}O^-$, Al_2^-, AlO_2^-, FeO_2^-, where Al_2^- and Fe_2^- ions represent Al and Fe in metallic state, respectively, while AlO_2^- and FeO_2^- ions correspond to Al and Fe in oxidized state, respectively. The $^{18}O^-$ is selected as the representative for oxygen due to the saturation of the detector in the case of $^{16}O^-$ selection [185]. The depth profile can be divided into two main zones: Surface film and alloy substrate, which is divided with a dashed line indicated as the interface. In the initial phase of sputtering, a rapid increase in metallic ion intensity is observed, which tends to stabilize with increasing sputtering time. The alloy substrate begins when the Al^- ion reaches a plateau and remains constant. The surface film can be identified up to about 120 s sputter time. The Fe^- ion appears to show a slight hump at the interface, which is attributed to Fe enrichment at the metal/film interface. This phenomenon is also reported in other literature where the solute enrichment is observed due to the rapid oxidation kinetics of Al [11,161] . A simplified layered model is illustrated in Figure 8.12 to understand the elemental distribution. The surface film consists mainly of Al oxide with Fe oxide located at the top portion, while the metallic Fe enrichment is located at the metal/film interface.

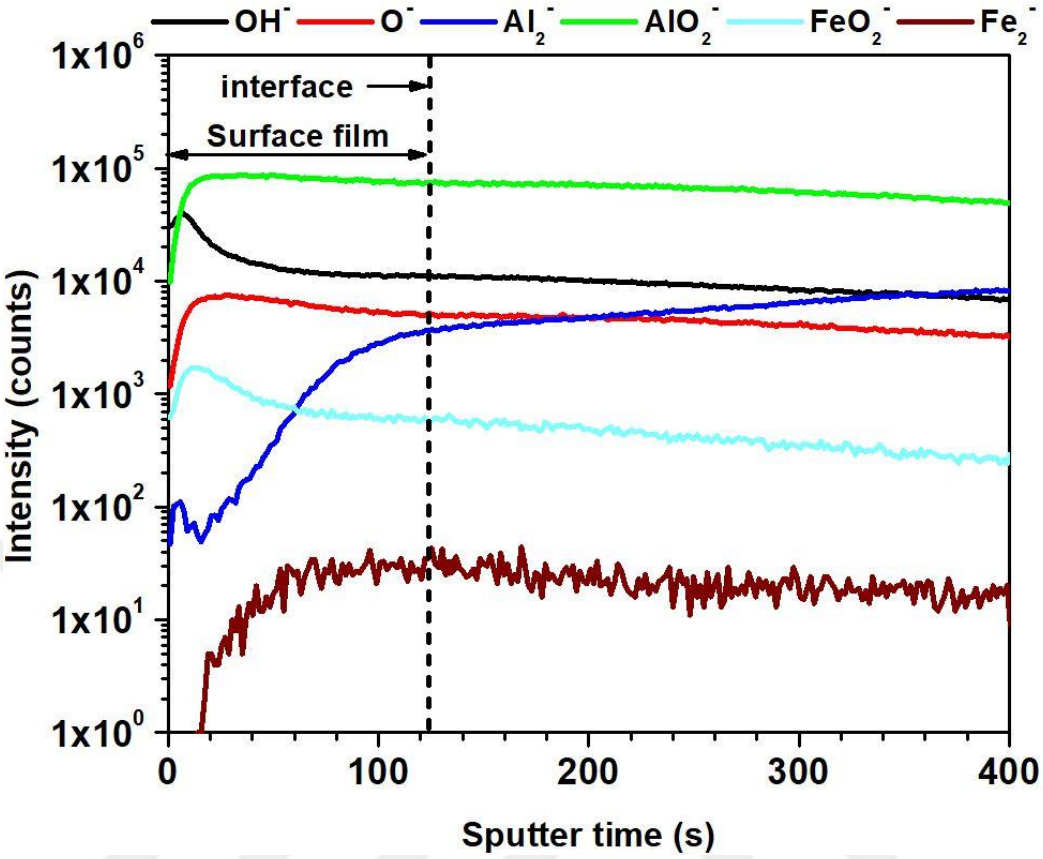

Figure 8.11 ToF-SIMS data showing the negative ion depth profiles with respect to sputter time.

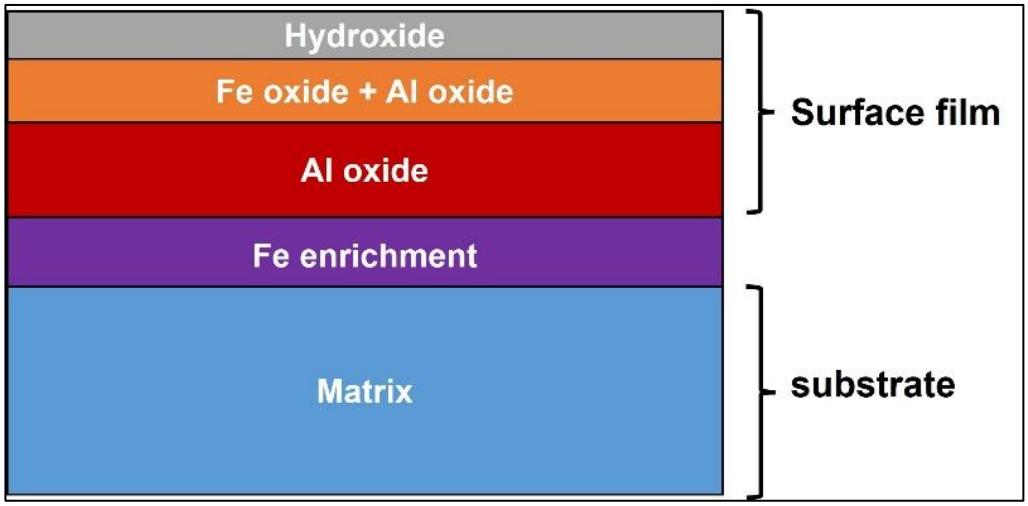

Figure 8.12 Schematic representation of layered model of the surface film.

The passive film was further investigated using XPS after the immersion in 0.1 M NaCl for 2 hours. Al, O, and Fe peaks were detected in the XPS survey scan of the Al-5Fe alloy. XPS Survey scan is presented in Figure 8.13 The high-resolution regional scans of the Al2p, Fe2p3/2 and O1s peaks of the Al-5Fe alloy are shown in Figure 8.14. The binding energies (BE), full width half maximum (FWHM), and intensities (in atomic percent) of the species are reported in Table 8.1. The Al2p peak (in Figure 8.14.a) showed peaks at two binding energies, metallic Al (Al^0) with a lower binding energy at 72.69 eV and Al oxide/hydroxide (Al^{3+}) with a higher binding energy at 75.2 eV. The O1s peak shown in Figure 8.14.c was compromised of two peaks (I and II), where O(I) is attributed to hydroxide or carbon bonded with oxygen obtained at a higher binding energy of 533.03 eV and O(II) is coming from the oxide contribution obtained at a lower binding energy of 531.77 eV [148]. The high-resolution peak corresponding to Fe2p3/2 is presented in Figure 8.14b, which is deconvoluted into four peaks: FeO(OH) (712.79 eV), Fe_2O_3 (711.16 eV), FeO (709.68 eV), and metallic Fe^0 (706.1 eV). Fe_2O_3 had the highest intensity among the three oxides, followed by FeO(OH) and FeO. The elemental concentration of Al oxide thickness on the surface of Al-5Fe alloy was estimated by the XPS investigation, and the oxide thickness was 7 nm, calculated with the help of the method reported in the literature [186]. The estimation by XPS survey illustrates that the oxide film was a combination of O, Al, and Fe. The oxide to Al ratio was estimated to be 2.62, which is about 1.75 times higher than the stoichiometric value of Al_2O_3. The higher stoichiometric ratio can be attributed to the additional presence of iron oxides along with the hydroxides. Moreover, the theoretical ratio of as-added metallic Fe/Al (5/95 at.%) should be 0.05 but the surface shows the ratio to be 0.13 which signifies the strong contribution coming from the Fe enrichment at the metal/film interface.

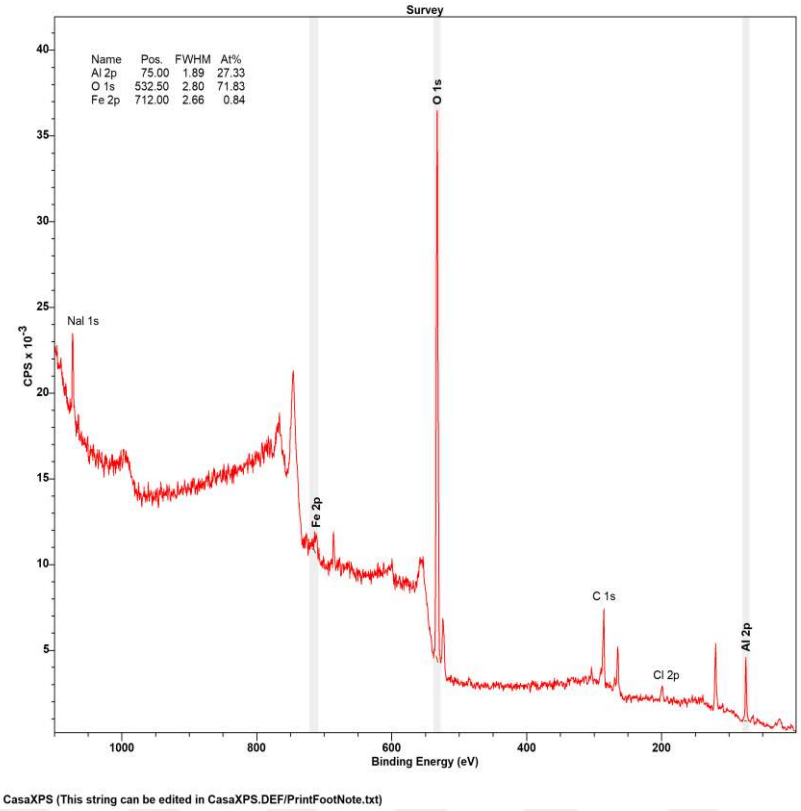

Figure 8.13 XPS survey scan for Al-5Fe alloy immersed in 0.1 M NaCl for 2 hours

Table 8.1 Binding energies (BE), full-widths at half maximum (FWHM) and intensities (in atomic percent) of the Al-5Fe alloy after 2 hours immersion in 0.1 M NaCl

Peak	**BE (eV)**	**FWHM**	**Intensity (at.%)**
O(I)	533.03	2.2	51.16
O(II)	531.77	2.1	21.47
Al^{3+}	75.20	1.7	24.89
Al^{0}	72.69	1.1	1.21
FeO	709.68	2.3	0.35
Fe_2O_3	711.16	2.2	0.44
FeO(OH)	712.79	2.8	0.32
Fe^{0}	706.31	1.8	0.16

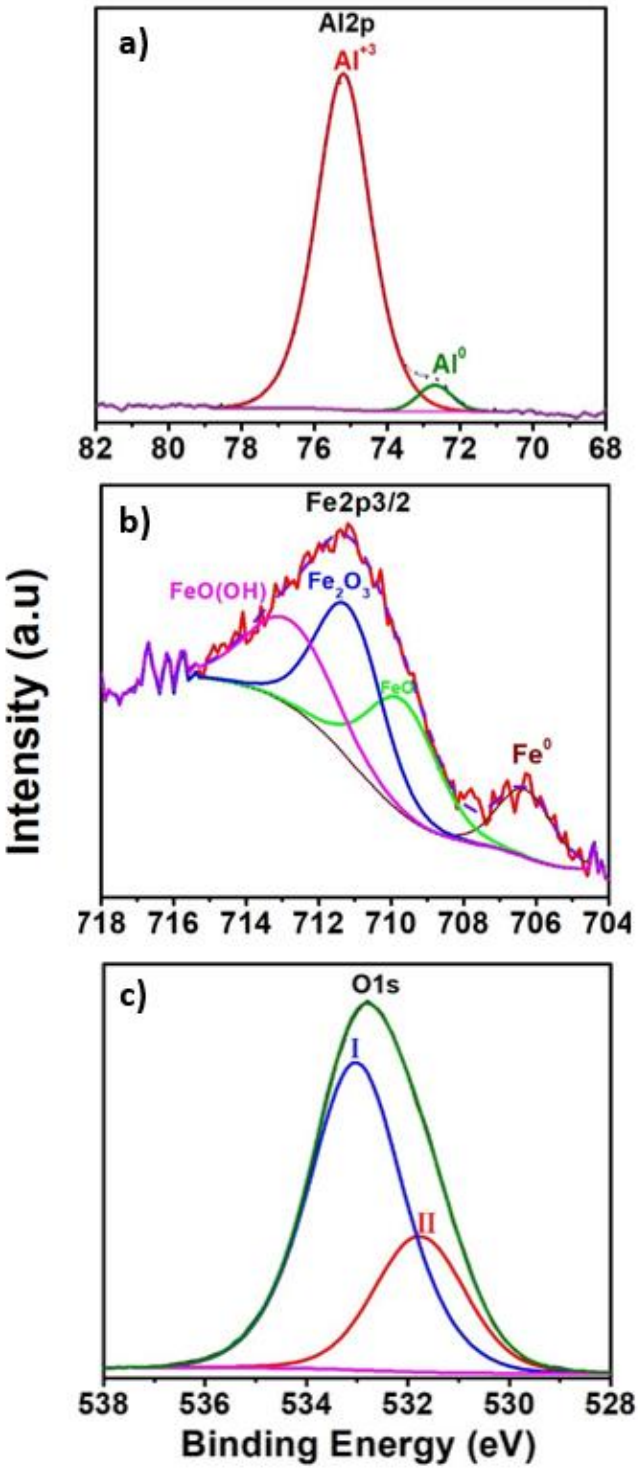

Figure 8.14 XPS high-resolution regional scan of a) Al2p, b) Fe2p3/2 and c) O1s peaks showing the metallic and oxidized species.

STEM cross-sectional images of the passive film for the Al-5Fe alloy after 2 hours of immersion in 0.1 M NaCl solution are shown in Figure 8.16 In Figure 8.16.b, the passive film is shown and indicated by dotted lines. The average thickness of the passive film was 5.7 nm and agreed with the estimated data from XPS analysis. The EDS mapping obtained from the zone in Figure 8.16.c indicated the distribution of O on top of the alloy (Figure 8.16.d) and therefore verified the uniformly formed passive film. Additionally, the Fe enrichment is observed at the metal/film interface (Figure 8.17and Figure 8.18 that is in correlation with TOF-SIMS and XPS investigation.

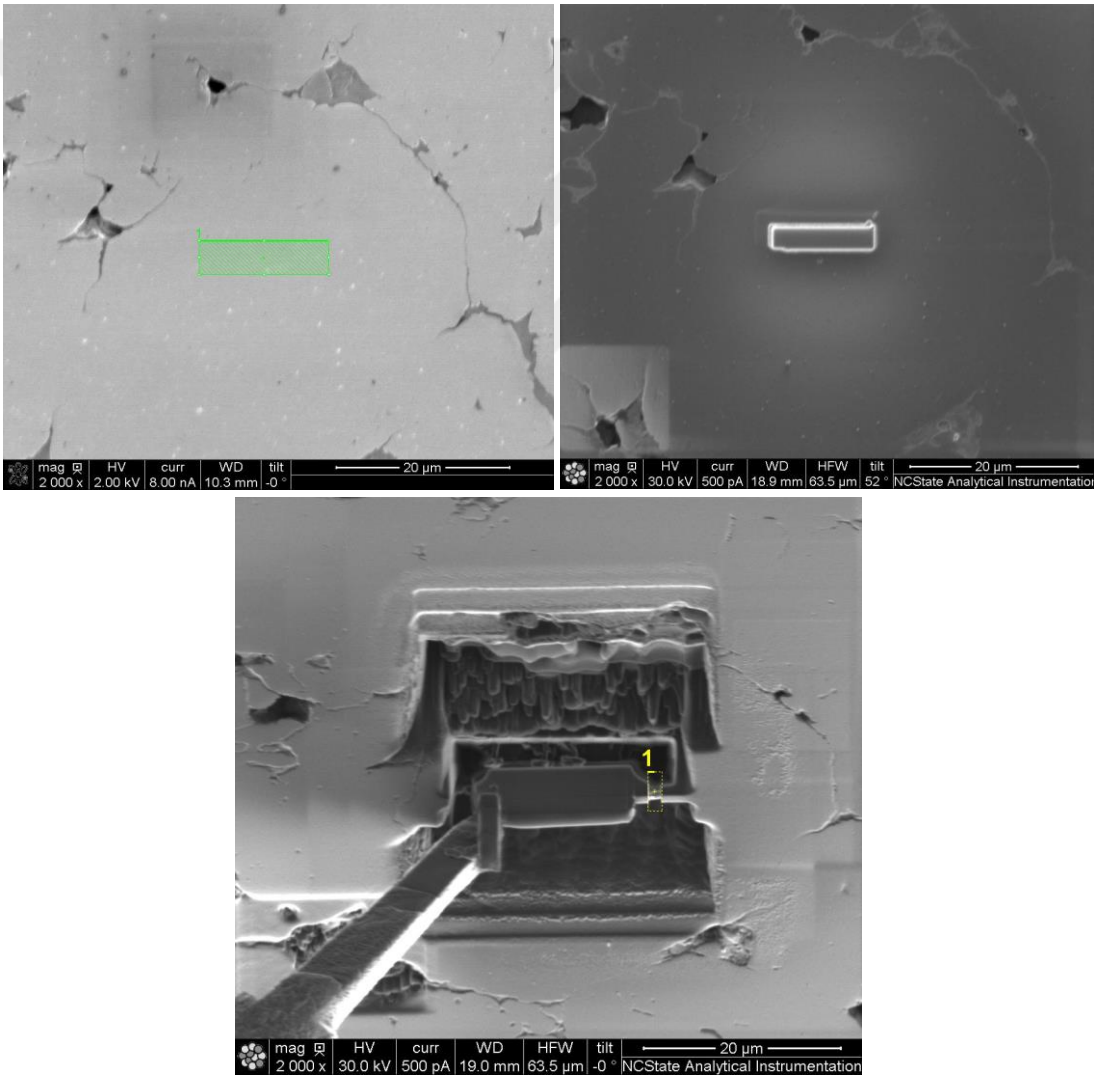

Figure 8.15 FIB location for TEM sample preparation

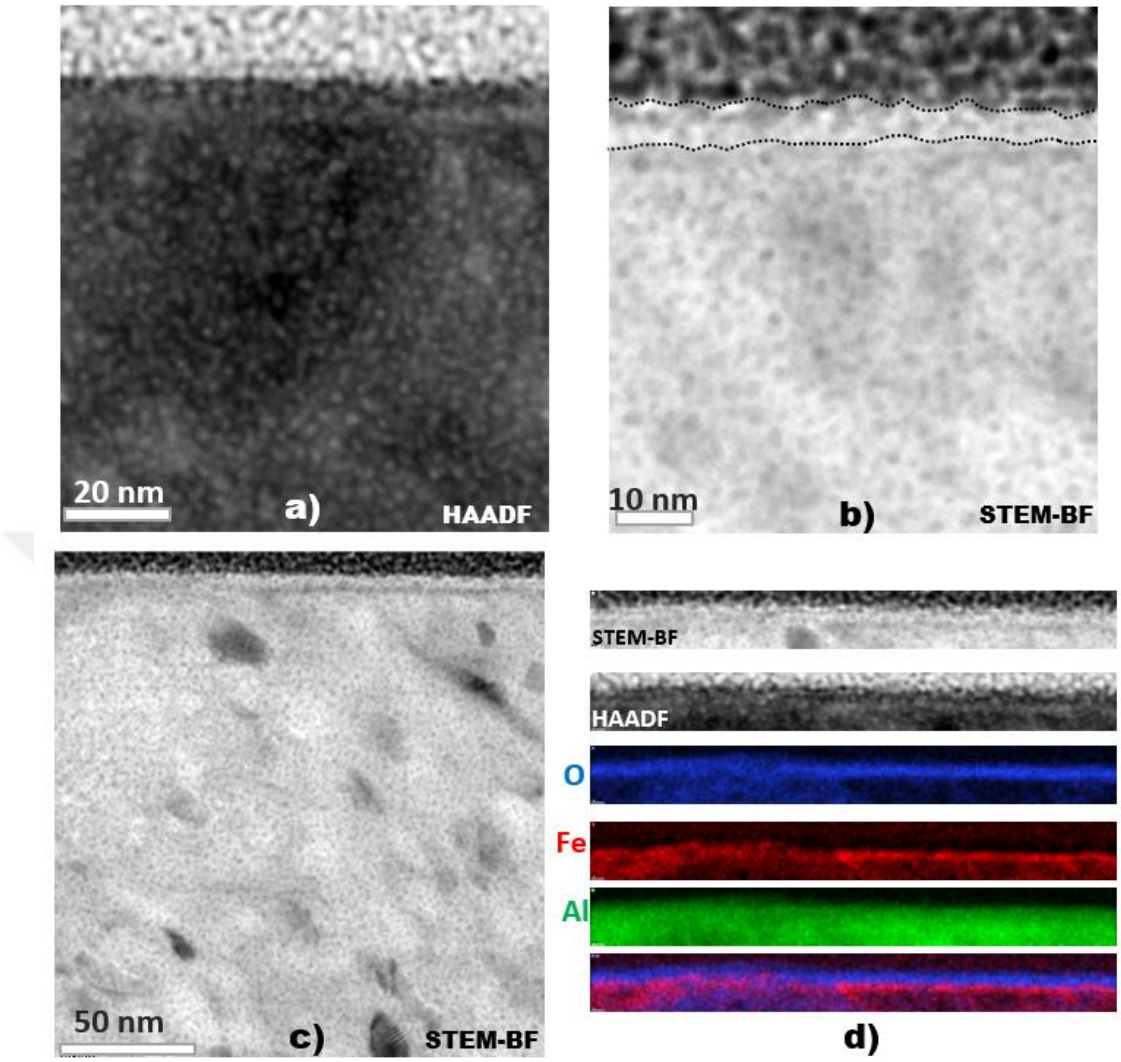

Figure 8.16 Passive film structure of Al-5Fe alloy a) High angle annular dark field (HAADF), b) and c) STEM Bright field (BF) images showing the uniform passive film, d) STEM-BF and HAADF images and EDS elemental mapping for Al, Fe, O; taken from c).

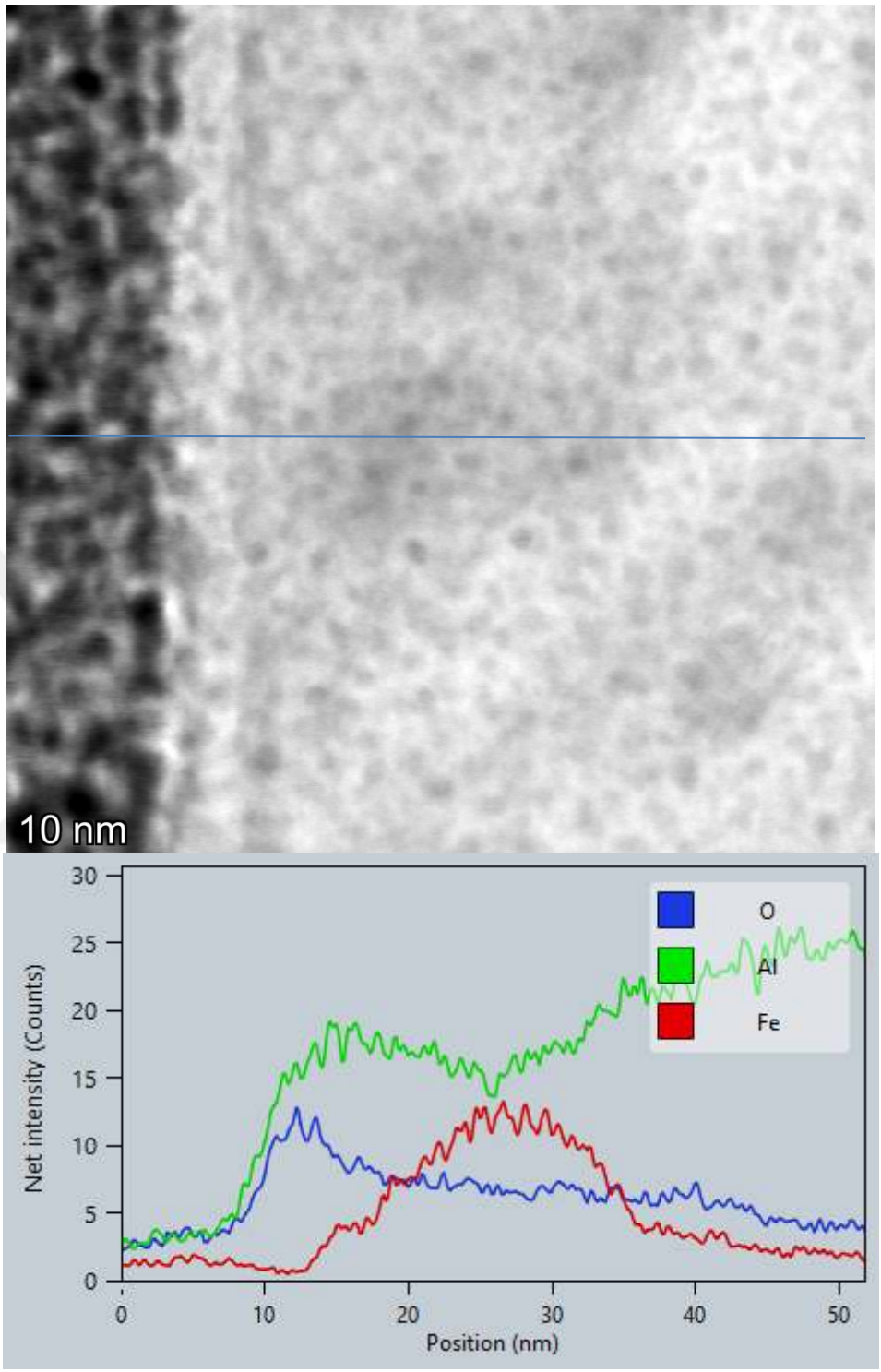

Figure 8.17 STEM BF image and EDS line scan for Al-5Fe alloy

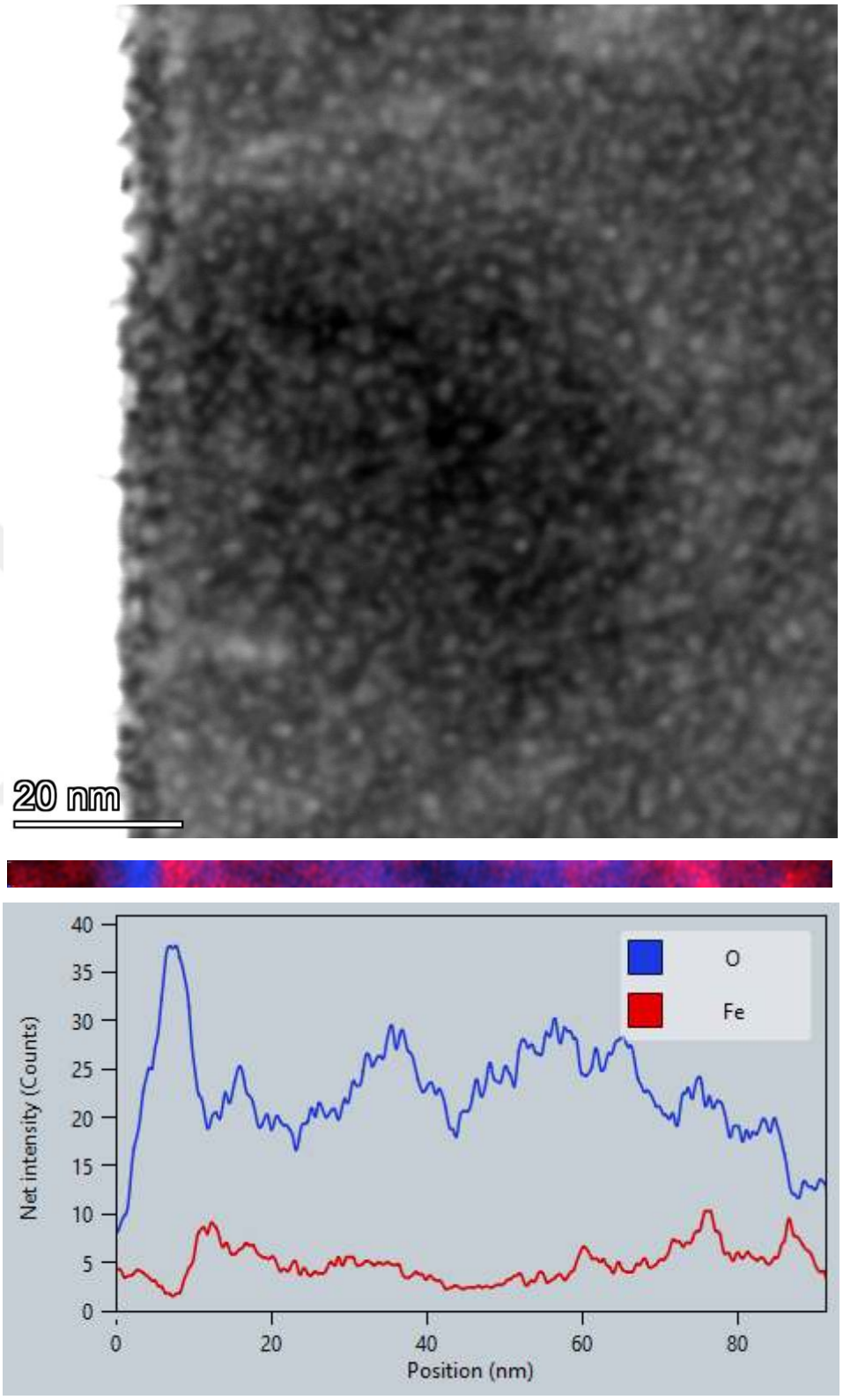

Figure 8.18 STEM HAADF image and EDS line scan for Al-5Fe alloy

The hardness of the Al-5Fe alloy is presented in Figure 8.19. The Al-5Fe alloy with an average hardness of 319 HV, showed significantly higher hardness compared to commercially available high-strength aluminum alloys, as shown in Figure 8.19.a. The hardness of the Al-5Fe alloy was also compared with nanocrystalline Al-5M alloys that were prepared by high-energy ball milling (Figure 8.19.b) [9], where the Al-5Fe alloy showed a superior value than reported Al-5M alloys, which can be attributed to the combined influences of grain refinement, enhanced solute solution and uniform dispersion of secondary phases.

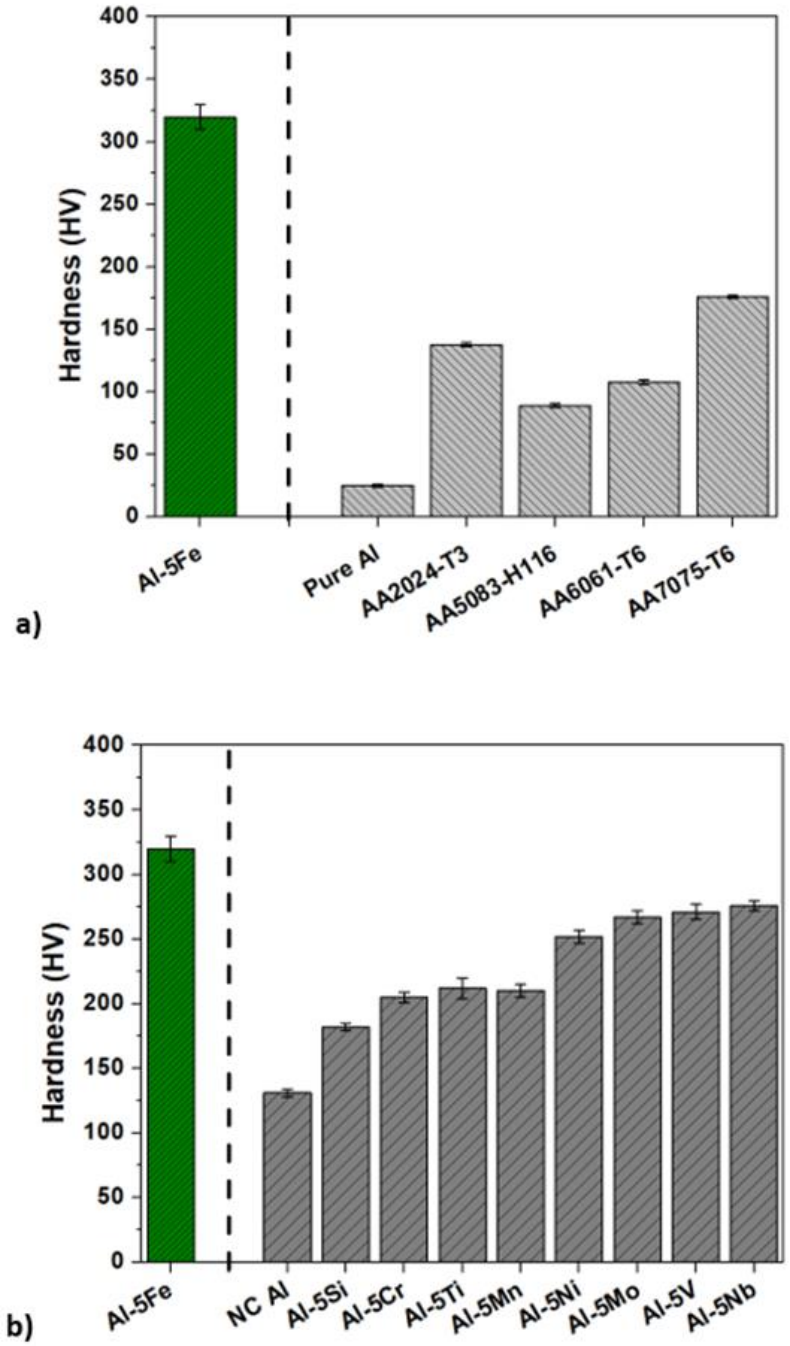

Figure 8.19 Plot of Vickers hardness a) Comparison of Al-5Fe with pure Al, AA2024-T3, AA5083-H116, AA6016-T6, AA7075-T6 b) Comparison of Al-5Fe with nanocrystalline Al (NC Al) and Al-5M alloys (M: Si, Cr, Ti, Mn, Ni, Mo, V, Nb with 5 at.%)

8.2.5 Discussion

The Al-5Fe alloy investigated in this study exhibited superior hardness and corrosion resistance. Compared to pure Al, the corrosion resistance of the Al-5Fe alloy was significantly higher due to the synergistic effect of extended solid solubility and a nanocrystalline structure known for its advantage on the passivation capabilities of the alloys [3,58,139]. This study is new and interesting from both technological and scientific perspectives. The alloying elements reported to improve corrosion performance in nonequilibrium Al alloys are based on expensive elements such as Cr, Ni, Ti, V, Mn, Nb, and Ta which leads to high material costs. Considering the elemental costs of the alloys calculated based on the data presented in [187]; the cost of the Al-5Fe alloy (~1.75 $/kg), is significantly lower than other binary alloys such as Al-5V (~3.78 $/kg), Al-5Nb (~8.06 $/kg) and Al-5Mo (~4.13 $/kg).

Fe is known for its deleterious effects on the corrosion performance of the Al alloys, and its content accumulates continuously during primary and secondary processing of aluminum. Therefore, it requires close control to monitor the Fe content, which is highly challenging to refine from the alloy. Considering the material cost of Fe and the efforts made to refine from the microstructure, the Al-5Fe alloy results were very promising for the direct employment of high Fe-containing materials as high-performance alloys. In addition, it should be cognizant of the fact that recycling, which is critical for sustainability, introduces Fe [188] and therefore reduces the corrosion performance of the alloys and limits the use of recycled Al in several applications [67,189,190]. The results of this study indicate that a bulk Al alloys with high Fe content and high corrosion resistance can be produced, which is promising for recycling of Al alloys.

The intermetallic compounds of Al-Fe in the ball milled alloy were refined and therefore the unfavorable effects were eradicated [191]. The extended solid solution of Fe in Al appears to cause significant improvement in corrosion performance. Additionally, the electrochemical potential difference between cathodic Fe-intermetallic compounds and the Fe-rich matrix could be decreased, which resulted in decreased galvanic activity and therefore higher pitting corrosion resistance [73].

The high corrosion resistance of the ball milled alloys such as Al-V alloys is attributed to one or more of the following mechanisms proposed in the literature [9,148]: Improved passivity by enrichment of alloying element at metal/film interface, improved ability of alloy for repassivation, release of corrosion inhibiting compounds such as vanadates and molybdates, and higher vacancy annihilation due to solute ion doped passive layers. The modification in the passive film of Al-5Fe alloy was demonstrated by XPS and SIMS studies. The surface film showed the presence of metallic and oxidized Fe in the passive film of Al-5Fe alloy. The presence of Fe in oxidized state within the passive film could lead to a change in the number of oxygen vacancies, which can be attributed to the formation of low mobility species [148]. In addition, SIMS and XPS studies did not reveal the presence of chloride in the passive film structure. The Cl incorporation is known to be a token for the localized Al corrosion [192–194] and the absence of chloride could be attributed to the Fe in the passive film that interferes with the Cl incorporation, which needs further focused research. Witharamage et al. [148] and Christudasjustus et al. [161] attributed the improved corrosion resistance to either an additional barrier from metallic V enrichment or deposition of V in the form of vanadate on cathodic phases in the nanocrystalline Al-V alloy. The solute enrichment at the metal/film interface in Al-Fe alloy (Figure 6.d) is similar to the aforementioned works however suggests different mechanisms. In all likelihood, Fe enrichment at the metal/passive film interface causes an extra Fe oxide layer that provides an obstacle to formation of the pit. However, unlike V-oxyanions, which act as an inhibitor, Fe does not assist in formation of an inhibitor that decreases the cathodic response. Therefore, it is more likely to suggest two mechanisms in Al-5Fe alloy in improving the corrosion resistance: 1) presence of Fe enrichment at metal/film interface that hinder the penetration of chloride ions, and 2) decrease in potential difference between cathodic particle and the matrix due to enhanced solid solution.

The Al-5Fe alloy investigated herein showed the highest hardness among Al-5-M alloys, along with significant corrosion performance, ranking after V, Mo, and Nb. This high strength can be attributed to the uniform dispersion of refined Al-Fe intermetallics, significant grain refinement, and the enhanced solid-state solubility of

iron [118,143,159,195]. The strengthening mechanisms that contribute to the overall strength of the Al-5Fe alloy can be estimated by quantifying the individual contribution of each mechanism are presented in Table 8.2.

The yield strength of the Al-5Fe alloy (σ_y) can be estimated using the following equation:

$$\sigma_y = \sigma_{gb} + \sigma_{ss} + \sigma_{other} \quad (1)$$

where, σgb is the strength contribution from grain boundaries, σ_{ss} is the strength contribution from solid solution strengthening, σ_{other} is the strength contribution from other strengthening mechanisms; mainly strength due to dislocations σ_d, and strength contribution from fine intermetallic phases; σ_{Or}

The contribution from grain boundaries can be estimated by Hall-Petch equation [144];

$$\sigma_{gb} \approx \sigma_o + k(d)^{1/2}$$

Where σ_o is the friction stress for the base metal (17 MPa) [119], k and d are the Hall-Petch coefficient (0.098 MPa $m^{1/2}$) [121,196] and average grain size, respectively. The individual contribution of the σ_{gb} was estimated as ~709 MPa.

Considering the different atomic radii of Al (143.2 pm) and Fe (127.4 pm), the individual contribution of solid solution strengthening can be estimated by [173,197];

$$\sigma_{ss} = G\varepsilon \left(\frac{x}{4}\right)^{1/2}$$

Where G represents the shear modulus (26 GPa) , ε represents the difference in between the Al and Fe atom fractions (0.11) [198] and x represents the concentration of Fe atom in the solid solution. The individual contribution from the Fe atoms in the solid solution is estimated as ~231 MPa.

The contribution from dislocation strengthening is estimated by Bailey-Hirsch equation [124];

$$\sigma_d = \underline{M}\alpha G b \rho^{\frac{1}{2}}$$

Where $\underline{M}$ denotes the average orientation factor (3.06), α denotes a constant (0.2), G represents the shear modulus (26 GPa), b represents the burger's vector (0.286 nm) and ρ represents the dislocation density estimated by:

$$\rho = \frac{2\sqrt{3}\varepsilon}{Db}$$

Where ε represents the lattice strain and D is average grain size which are extracted from XRD data [115].

The individual contribution from dislocation strengthening was estimated as ~220 MPa.

The strength contribution from fine precipitates can be estimated by Orowan strengthening [173,196];

$$\sigma_{Orowan} = 0.7MGb(\frac{f^{\frac{1}{2}}}{r})$$

Where M represents the Taylor factor, f and r represent the particle fraction and mean diameter of the precipitates, respectively. The significant refinement in the particles did not facilitate the reasonable estimation of the Orowan strengthening which is attributed to the radius and fraction of the particles. However, σ_{Orowan} is accounted for only minor contribution to the overall strength in high-energy ball milled alloys as reported in the literature [65,126,127,196].

The yield strength of the alloy can be estimated using Tabor's rule [120];

$$\sigma_y = H * 1/3$$

Where H represents the value of microhardness in MPa. The estimated yield strength of the Al-5Fe alloy was estimated to be 1078 MPa. The estimated contribution of individual strengthening mechanisms and the experimental estimate of the yield strength are summarized in Table 2. The total yield strength calculated by combining

the estimated individual strengthening contributions was 1160 MPa, which was in close agreement with the estimated experimental yield strength. Grain boundary strengthening was the largest contributor (~62%) to the total estimated yield strength, followed by solid solution strengthening (~21%).

The primary contribution is due to grain boundary strengthening (σ_{gb}) followed by solid solution strengthening (σ_{ss}). The other contributions to overall strength (σ_{Other}) includes strength contribution due to fine precipitates by Orowan strengthening σ_{Orowan} and contributions from dislocations [65,121,122,173].

Table 8.2 Estimated different strengthening contributions to the yield strength of Al-5Fe alloy

	σ_{gb} (MPa)	σ_{ss} (MPa)	σ_{other} (MPa)	$\sigma_y(estimated)$ (MPa)	$\sigma_y(experimental)$ (MPa)
Al-5Fe	709	230	225	1160	1078

8.2.6 Conclusions

Nanocrystalline Al-5Fe alloy was successfully produced by high-energy ball milling followed by consolidation through room-temperature compaction. The Al-5Fe alloy exhibited extended solid solubility of Fe in Al and homogeneous microstructure free from coarse intermetallics. The alloy exhibited high strength due to the enhanced solid solubility of Fe, ultra-fine grain refinement, and uniform distribution of Al-Fe intermetallics.

The Al-Fe alloys showed high pitting corrosion resistance as investigated using cyclic potentiodynamic polarization test. Surface characterization using STEM, XPS and SIMS revealed formation of Al-rich passive film with Fe enrichment at the surface film/substrate interface. The improvement in the corrosion performance of Al-5Fe alloy was attributed to the following factors:

- Combined influences of homogeneous microstructure and refined secondary phases with lower surface area.
- The decrease in the galvanic activity between matrix and cathodic particle, and additional barrier due to the Fe enrichment at the metal/film interface.
- The modification in the passive film structure due to the incorporation of Fe and thus the improved ability to re-passivate.

CHAPTER 9

SUMMARY AND FUTURE WORK

Annual global cost of corrosion is estimated as 2.5$ trillion [199]. Mitigating the corrosion and developing of corrosion resistant materials and coatings are challenges of corrosion research in today's world where sustainability is a critical concern. The present study addresses the corrosion issues of high strength aluminum alloys which are increasingly demanded in advanced applications. The coexistence of ultra-high strength and superior corrosion performance is a virtue that not found in conventional Al alloys. Non-equilibrium techniques promise many performance improvements, but majority of these techniques deliver materials in the form of thin films that cannot be consolidated for structural applications. High-energy ball milling is a proven technique to produce alloy powder that can be consolidated into desired shape. Recently, simultaneous enhancement in the corrosion and mechanical performance of the Al alloys has been reported through high energy ball milling of Al while there are former studies reporting similar or worse corrosion performance with the alloys produced by same processing technique. However, there are certain research gaps both in development of novel compositions and in the understanding of the mechanisms that provide the strength and corrosion performance.

The major conclusions of the present study can be summarized as follows:

- High energy ball milling is shown as an efficient method for production of commercial age hardening alloys, as they exhibit homogenous microstructure that free from coarse secondary phases, and significant grain refinement (below 100 nm).

- A comparison between the commercial age hardening alloys subjected to thermomechanical treatment and nanocrystalline alloys indicated that the corrosion and hardness performance of the high-energy ball milled alloys was significantly enhanced in the as milled & compacted state, which were not subjected to any age hardening or thermomechanical treatments.

- Milling is generally conducted under inert atmosphere to avoid oxidation possible undesired reactions. In the present study, the hypothesis along with the experimental validation of modification in the milling environment by performing the operation under air atmosphere rather than an inert atmosphere has been demonstrated. The milling under air atmospheres successfully conducted. The hardness and corrosion resistance of AA2024 milled in Ar and air was higher than that of commercial AA2024-T3, which was attributed to the refined microstructure. HEBM in air resulted in higher hardness and corrosion resistance than that in Ar. Furthermore, HEBM in air exhibited improved thermal stability which is a challenge with the nanocrystalline materials after an isothermal heat treatment at 400 °C and 500°C for one hour. Therefore, high purity milling atmosphere is not necessary to achieve superior hardness and corrosion performance for Al alloys and the powder is of great importance for potential additive manufacturing applications.

- Modification of the composition of AA2024 with V and $CeNO_3$ addition exhibited interesting outputs. The modifiers selected referencing the literature of corrosion of Al alloys, particularly high-energy ball milled alloys of which Al-V exhibited highest corrosion resistance. The influence of V addition on the hardness and corrosion of AA2024 which is dominated by cathodic constituents exhibited performance improvement in hardness (~10%) and repassivation potential (~%35) which is attributed to the extended solid solubility of the V which lead to formation V-ions within the pits. The deposition of V on cathodic particles suppressed cathodic reaction and enhanced the repassivation ability.

- The present study intended to fill the research gap in light of previous chapters and literature reviewed. Therefore, 3 candidates from transition metals and 1 from rare earth elements were selected. The results indicated a significant corrosion resistance along with the hardness in the Al-Fe alloy. The proposed mechanisms for the role of Fe in superior pitting corrosion is explained through characterization of passive film. The improved corrosion performance is

attributed to following factors of homogeneous microstructure and refined secondary, the decrease in the galvanic activity between matrix and cathodic particle, additional barrier due to the Fe enrichment at the metal/film interface and modification in the passive film due to the incorporation of Fe and thus the improved ability to re-passivate.

For the future work, the following objectives can be proposed:

- The consolidation was only performed with cold compaction. The methods that provide further densification could be employed.
- The thermal stability of the produced alloys needs to be investigated further. The modification in the milling indicated improved thermal stability that the powder could be suitable for additive manufacturing processes that includes laser melting or deposition.
- The corrosion behavior of multi-component/ multi principal alloying elements needs to be investigated.
- Computational investigation and modelling of corrosion behavior of nanocrystalline aluminum alloys produced by high-energy ball milling.

REFERENCES

[1] I. Polmear, D. Stjohn, J.-F. Nie, Qian Ma, Light Alloys Metallurgy of the Light Metals, 5th ed., Butterworth-Heinemann, 2017.

[2] V. Chak, H. Chattopadhyay, T.L. Dora, A review on fabrication methods , reinforcements and mechanical properties of aluminum matrix composites, J. Manuf. Process. 56 (2020) 1059–1074.

[3] K.D. Ralston, D. Fabijanic, N. Birbilis, Effect of grain size on corrosion of high purity aluminium, Electrochim. Acta. 56 (2011) 1729–1736.

[4] M. Liu, R. Zheng, J. Li, C. Ma, Achieving ultrahigh tensile strength of 1 GPa in a hierarchical nanostructured 2024 Al alloy, Mater. Sci. Eng. A. 788 (2020) 139576. https://doi.org/10.1016/j.msea.2020.139576.

[5] B. Chen, Surface nanocrystallization induced by shot peening and its effect on corrosion resistance of 6061 aluminum alloy, 29 (2014). https://doi.org/10.1557/jmr.2014.323.

[6] R. Gupta, B. Murthy, N. Birbilis, An Overview of High-energy Ball Milled Nanocrystalline Aluminum Alloys, 1st ed., Springer International Publishing, 2017. https://doi.org/10.1007/978-3-319-57031-0.

[7] J. Esquivel, K.A. Darling, H.A. Murdoch, R.K. Gupta, Corrosion and Mechanical Properties of Al-5 At. Pct Cr Produced by Cryomilling and Subsequent Consolidation at Various Temperatures, Metall. Mater. Trans. A Phys. Metall. Mater. Sci. 49 (2018) 3058–3065. https://doi.org/10.1007/s11661-018-4620-5.

[8] P. V. Liddicoat, X.Z. Liao, Y. Zhao, Y. Zhu, M.Y. Murashkin, E.J. Lavernia, R.Z. Valiev, S.P. Ringer, Nanostructural hierarchy increases the strength of aluminium alloys, Nat. Commun. 1 (2010) 1–7.

[9] J. Esquivel, H.A. Murdoch, K.A. Darling, R.K. Gupta, Excellent corrosion resistance and hardness in Al alloys by extended solid solubility and nanocrystalline structure, Mater. Res. Lett. 6 (2018) 79–83. https://doi.org/10.1080/21663831.2017.1396262.

[10] S. Venkatraman, M.R. Nair, D.C. Kothari, K.B. Lal, R. Raman, Anodic polarization behaviour of ion implanted aluminum in 3.5 wt.% NaCl electrolyte, Nucl. Instruments Methods Phys. Res. 19 (1987) 241–246.

[11] E.L. Principe, B.A. Shaw, G.D. Davis, Role of Oxide / Metal Interface in Corrosion Resistance : Al-W and Al-Mo Systems, Corrosion. 59 (2003) 295–313. https://doi.org/https://doi.org/10.5006/1.3277562.

[12] M. Metikoš-Hukovi, N. Radi, Z. Grubač, H.A. Tonejcv, The corrosion behavior

of sputter-deposited aluminum-tungsten alloys, Electrochim. Acta. 47 (2002) 2387–2397. https://doi.org/10.1016/S0013-4686(02)00040-3.

[13] J.R. Davis, Aluminum and Aluminum Alloys, in: Alloy. Underst. Basics, ASM International, 2001: pp. 351–416. https://doi.org/10.1361/autb2001p351.

[14] H. Gleiter, Nanostructured materials: basic concepts and microstructure, Acta Mater. 48 (2000) 1–29. https://doi.org/10.1016/S1359-6454(99)00285-2.

[15] A.R. Hind, S.K. Bhargava, S.C. Grocott, The surface chemistry of Bayer process solids: A review, Colloids Surfaces A Physicochem. Eng. Asp. 146 (1999) 359–374. https://doi.org/10.1016/S0927-7757(98)00798-5.

[16] W.E. Haupin, Electrochemistry of the Hall-Heroult process for aluminum smelting, J. Chem. Educ. 60 (1983) 279. https://doi.org/10.1021/ed060p279.

[17] C. Vargel, Corrosion of Aluminium, Elsevier, 2004. https://doi.org/10.1016/B978-0-08-044495-6.X5000-9.

[18] R.B.C. Cayless, Alloy and Temper Designation Systems for Aluminum and Aluminum Alloys, ASM Handbook, Vol. 2 Prop. Sel. Nonferrous Alloy. Spec. Mater. 2 (1990) 15–28. https://doi.org/10.1361/asmhba000.

[19] J. Brown, Foseco non-ferrous foundryman's handbook, 11th ed., Butterworth-Heinemann, Oxford, 1999.

[20] ASM Handbook Vol 4 Heat Treating, ASM International, 1991.

[21] Ö. Keleş, Alüminyumun Serüveni, İTÜ Vakfı Yayınları, İstanbul, 2021.

[22] N.L. Sukiman, R.K. Gupta, R.G. Buchheit, N. Birbilis, Influence of microalloying additions on Al – Mg alloy . Part 1 : Corrosion and electrochemical response, Corros. Eng. Sci. Technol. 49 (2014). https://doi.org/10.1179/1743278213Y.0000000128.

[23] K. Van Horn, Aluminum - Volume 1: Properties, Physical Metallurgy and Phase Diagrams, American Society of Metals, 1967. https://books.google.com.tr/books?id=3uVPnQAACAAJ.

[24] J. Li, Electrochemical Characterization of Intermetallic Compounds in AA2024-T3 and Localized Corrosion Morphology of Al-Cu-Mg at Elevated Temperature, The Ohio State University, 2014. https://doi.org/10.4324/9781315853178.

[25] E. McCafferty, Introduction of corrosion science, 2009. https://doi.org/10.1017/CBO9781107415324.004.

[26] N.L. Sukiman, X. Zhou, N. Birbilis, A.E. Hughes, J.M.C. Mol, S.J. Garcia, X. Zhou, G.E. Thompson, Aluminium Alloys - New Trends in Fabrication and Applications. (2012). https://doi.org/10.5772/3354.

[27] Z. Szklarska-Smialowska, Pitting corrosion of aluminum, Corros. Sci. 41 (1999) 1743–1767. https://doi.org/10.1016/S0010-938X(99)00012-8.

[28] M. Pourbaix, H. Zhang, A. Pourbaix, Presentation of an Atlas of chemical and electrochemical equilibria in the presence of a gaseous phase, Mater. Sci. Forum. 251–254 (1997) 143–148.

[29] Z. Ahmad, Recent Trends in Processing and Degradation of Aluminium Alloys, 2nd ed., Elsevier Science & Technology Books, 2016. https://doi.org/10.5772/741.

[30] N. Birbilis, R.G. Buchheit, Electrochemical Characteristics of Intermetallic Phases in Aluminum Alloys An Experimental Survey and Discussion, (2005) 140–151. https://doi.org/10.1149/1.1869984.

[31] R.G. Buchheit, A Compilation of Corrosion Potentials Reported for Intermetallic Phases in Aluminum Alloys, J. Electrochem. Soc. 142 (1995) 3994–3996. https://doi.org/10.1149/1.2048447.

[32] A. Staszczyk, J. Sawicki, B. Adamczyk-Cieslak, A study of second-phase precipitates and dispersoid particles in 2024 aluminum alloy after different aging treatments, Materials (Basel). 12 (2019). https://doi.org/10.3390/ma1224168.

[33] I. Polmear, Light Alloys, From Traditional Alloys to Nanocrystals, Fourth Edi, Butterworth-Heinemann, 2006.

[34] J.R. Davis, Corrosion of aluminum and aluminum alloys, Asm International, 1999.

[35] R.K. Gupta, B.S. Murty, N. Birbilis, An Overview of High-energy Ball Milled Nanocrystalline Aluminum Alloys, Springer, 2017.

[36] J. Esquivel, R.K. Gupta, Simultaneous Improvement of Mechanical and Corrosion Properties of Aluminum Alloys, in: Light Met. 2016, Springer, Cham, 2016: pp. 151–152. https://doi.org/https://doi.org/10.1007/978-3-319-48251-4_26.

[37] G.S. Frankel, C. Jahnes, R. Newman, On the Pitting Resistance of Sputter - Deposited Aluminum Alloys On the Pitting Resistance of Sputter-Deposited Aluminum Alloys, J. Electrochem. Soc. (1993). https://doi.org/10.1149/1.2220794.

[38] J. Esquivel, R.K. Gupta, Review—Corrosion-Resistant Metastable Al Alloys: An Overview of Corrosion Mechanisms, J. Electrochem. Soc. 167 (2020) 081504. https://doi.org/10.1149/1945-7111/ab8a97.

[39] C.C. Koch, Structural nanocrystalline materials : an overview, J. Mater. Sci. 42 (2007) 1403–1414. https://doi.org/10.1007/s10853-006-0609-3.

[40] C. Suryanarayana, C.C. Koch, Nanocrystalline materials – Current research and future directions, (2000) 5–44.

[41] K.M.S. Youssef, C.C. Koch, P.S. Fedkiw, Improved corrosion behavior of nanocrystalline zinc produced by pulse-current electrodeposition, Corros. Sci. 46 (2004) 51–64. https://doi.org/10.1016/S0010-938X(03)00142-2.

[42] R. Ly, K.T. Hartwig, H. Castaneda, Effects of strain localization on the corrosion behavior of ultra-fine grained aluminum alloy AA6061, Corros. Sci. 139 (2018) 47–57. https://doi.org/10.1016/j.corsci.2018.04.023.

[43] G. Tan, Y.E. Kalay, C.H. Gür, Long-term thermal stability of Equal Channel Angular Pressed 2024 aluminum alloy, Mater. Sci. Eng. A. 677 (2016) 307–315. https://doi.org/10.1016/j.msea.2016.09.048.

[44] X. Sauvage, N. Enikeev, R. Valiev, Y. Nasedkina, M. Murashkin, Atomic-scale analysis of the segregation and precipitation mechanisms in a severely deformed Al-Mg alloy, Acta Mater. 72 (2014) 125–136. https://doi.org/10.1016/j.actamat.2014.03.033.

[45] R. Khatami, A. Fattah-alhosseini, M.K. Keshavarz, Effect of grain refinement on the passive and electrochemical behavior of 2024 Al alloy, J. Alloys Compd. 708 (2017) 316–322. https://doi.org/10.1016/j.jallcom.2017.03.031.

[46] R.K. Gupta, D. Fabijanic, R. Zhang, N. Birbilis, Corrosion behaviour and hardness of in situ consolidated nanostructured Al and Al-Cr alloys produced via high-energy ball milling, Corros. Sci. 98 (2015) 643–650. https://doi.org/10.1016/j.corsci.2015.06.011.

[47] J. Esquivel, R.K. Gupta, Corrosion behavior and hardness of Al-M (M: Mo, Si, Ti, Cr) alloys, Acta Metall. Sin. (English Lett. 30 (2017) 333–341. https://doi.org/10.1007/s40195-017-0550-2.

[48] C. Suryanarayana, Mechanical Alloying : A Novel Technique to Synthesize Advanced Materials, Research. 2019 (2019). https://doi.org/https://doi.org/10.34133/2019/4219812.

[49] C. Suryanarayana, Mechanical alloying and milling, Prog. Mater. Sci. 46 (2001) 1–184. https://doi.org/10.1016/S0079-6425(99)00010-9.

[50] C. Suryanarayana, Recent Developments in Mechanical Alloying, (2015).

[51] C.C. Koch, Research on Metastable Structures Using High Energy Ball Milling at North Carolina State University (Overview), Mater. Trans. JIM. 36 (1995) 85–95. https://doi.org/10.2320/matertrans1989.36.85.

[52] E. Sikora, X.J. Wei, B.A. Shaw, Corrosion behavior of nanocrystalline bulk Al-Mg-based alloys, Corrosion. 60 (2004) 387–398. https://doi.org/10.5006/1.3287748.

[53] AN ELECTROCHEMICAL EVALUATION OF NEW MATERIALS AND by Esra Ku ş A Dissertation Presented to the FACULTY OF THE GRADUATE SCHOOL UNIVERSITY OF SOUTHERN CALIFORNIA In Partial Fulfillment of the Requirements for the Degree DOCTOR OF PHILOSOPHY (MATERIALS SCI, (2006).

[54] E. Kus, Z. Lee, S. Nutt, F. Mansfeld, A comparison of the corrosion behavior of nanocrystalline and conventional Al 5083 samples, Corrosion. 62 (2006) 152–161. https://doi.org/10.5006/1.3278260.

[55] R.K. Gupta, D. Fabijanic, T. Dorin, Y. Qiu, J.T. Wang, N. Birbilis, Simultaneous improvement in the strength and corrosion resistance of Al via high-energy ball milling and Cr alloying, Mater. Des. 84 (2015) 270–276. https://doi.org/10.1016/j.matdes.2015.06.120.

[56] M.F. Naeini, M.H. Shariat, M. Eizadjou, On the chloride-induced pitting of ultra fine grains 5052 aluminum alloy produced by accumulative roll bonding process, J. Alloys Compd. 509 (2011) 4696–4700. https://doi.org/https://doi.org/10.1016/j.jallcom.2011.01.066.

[57] K.D. Ralston, N. Birbilis, Effect of grain size on corrosion, Corrosion. 66 (2010) 1–4. https://doi.org/10.5006/1.3462912.

[58] R.K. Gupta, N. Birbilis, The influence of nanocrystalline structure and processing route on corrosion of stainless steel : A review, Corros. Sci. (2014). https://doi.org/10.1016/j.corsci.2014.11.041.

[59] G.D. Davis, W.C. Moshier, T.L. Fritz, G.O. Cote, Evolution of the Chemistry of Passive Films of Sputter- Deposited , Supersaturated AI Alloys, 137 (1990) 422–427.

[60] W. Moshier, G. Davis, J. Ahearn, Corrosion behavior of aluminum-molybdenum alloys in chloride solutions. 1986;134:2677–2684., J. Electrochem. Soc. 134 (1986) 2677–2684.

[61] M.E. Goldman, N. Ünlü, G.J. Shitlet, J.R. Scully, Selected Corrosion Properties of a Novel Amorphous Al-Co-Ce Alloy System, Electrochem. Solid-State Lett. 8 (2005) 2–6. https://doi.org/10.1149/1.1848261.

[62] J. Esquivel, M.G. Wachowiak, S.P. O'Brien, R.K. Gupta, Thermal stability of nanocrystalline Al-5at.%Ni and Al-5at.%V alloys produced by high-energy ball milling, J. Alloys Compd. 744 (2018) 651–657. https://doi.org/10.1016/j.jallcom.2018.02.144.

[63] S. Reyntjens, R. Puers, A review of focused ion beam applications in microsystem technology, J. MICROMECHANICS MICROENGINEERING. (2001) 287–300.

[64] BioLogic VMP-300, (n.d.). https://www.biologic.net/products/vmp-300/

(accessed July 7, 2022).

[65] F. Ozdemir, C.S. Witharamage, A.A. Darwish, H. Okuyucu, R.K. Gupta, Corrosion behavior of age hardening aluminum alloys produced by high-energy ball milling, J. Alloys Compd. 900 (2022) 163488. https://doi.org/10.1016/j.jallcom.2021.163488.

[66] R.K. Gupta, N.L. Sukiman, M.K. Cavanaugh, B.R.W. Hinton, C.R. Hutchinson, N. Birbilis, Metastable pitting characteristics of aluminium alloys measured using current transients during potentiostatic polarisation, Electrochim. Acta. 66 (2012) 245–254. https://doi.org/10.1016/j.electacta.2012.01.090.

[67] T. Dorin, N. Stanford, N. Birbilis, R.K. Gupta, Influence of cooling rate on the microstructure and corrosion behavior of Al-Fe alloys, Corros. Sci. 100 (2015) 396–403. https://doi.org/10.1016/j.corsci.2015.08.017.

[68] R.K. Gupta, R. Zhang, C.H.J. Davies, N. Birbilis, Theoretical study of the influence of microalloying on sensitization of AA5083 and moderation of sensitization of a model Al-Mg-Mn alloy via Sr additions, Corrosion. 70 (2014) 402–413. https://doi.org/10.5006/1117.

[69] M.K. Cavanaugh, J. Electrochem, C. Soc, M.K. Cavanaugh, J. Li, N. Birbilis, R.G. Buchheit, Electrochemical Characterization of Intermetallic Phases Common to Aluminum Alloys as a Function of Solution Temperature Electrochemical Characterization of Intermetallic Phases Common to Aluminum Alloys as a Function of Solution Temperature, (2014). https://doi.org/10.1149/2.0361412jes.

[70] J. Li, N. Birbilis, R.G. Buchheit, Electrochemical assessment of interfacial characteristics of intermetallic phases present in aluminium alloy 2024-T3, Corros. Sci. 101 (2015) 155–164. https://doi.org/10.1016/j.corsci.2015.09.012.

[71] F. Mansfeld, V. Wang, H. Shih, Development of “Stainless Aluminum,” J. Electrochem. Soc. 138 (1991) L74–L75. https://doi.org/10.1149/1.2085513.

[72] A.E. Hughes, R. Parvizi, M. Forsyth, Microstructure and corrosion of AA2024, Corros. Rev. 33 (2015) 1–30. https://doi.org/10.1515/corrrev-2014-0039.

[73] R.K. Gupta, A. Deschamps, M.K. Cavanaugh, S.P. Lynch, N. Birbilis, Relating the Early Evolution of Microstructure with the Electrochemical Response and Mechanical Performance of a Cu-Rich and Cu-Lean 7xxx Aluminum Alloy, J. Electrochem. Soc. 159 (2012) C492–C502.

[74] D.Y. Liu, J.F. Li, Y.L. Ma, R.K. Gupta, N. Birbilis, R. Zhang, A closer look at the role of Zn in the microstructure and corrosion of an Al-Cu-Li alloy, Corros. Sci. 145 (2018) 220–231. https://doi.org/10.1016/j.corsci.2018.10.003.

[75] P.C. King, I.S. Cole, P.A. Corrigan, A.E. Hughes, T.H. Muster, FIB/SEM study of AA2024 corrosion under a seawater drop: Part I, Corros. Sci. 53 (2011)

1086–1096. https://doi.org/10.1016/j.corsci.2010.12.004.

[76] Z. Zhao, G.S. Frankel, On the first breakdown in AA7075-T6, 49 (2007) 3064–3088. https://doi.org/10.1016/j.corsci.2007.02.001.

[77] K. Nişancıoğlu, Electrochemical Behavior of Aluminum-Base Intermetallics Containing Iron, J. Electrochem. Soc. 137 (2019) 69–77. https://doi.org/10.1149/1.2086441.

[78] K.D. Ralston, S. Chrisanti, T.L. Young, R.G. Buchheit, Corrosion Inhibition of Aluminum Alloy 2024-T3 by Aqueous Vanadium Species, (2008) 350–359. https://doi.org/10.1149/1.2907772.

[79] G.S. Chen, M. Gao, R.P. Wei, Microconstituent-Induced Pitting Corrosion in Aluminum Alloy 2024-T3, Corros. 52 (1996) 8–15. https://doi.org/10.5006/1.3292099.

[80] Y.L. Cheng, Z. Zhang, F.H. Cao, J.F. Li, J.Q. Zhang, J.M. Wang, C.N. Cao, A study of the corrosion of aluminum alloy 2024-T3 under thin electrolyte layers, Corros. Sci. 46 (2004) 1649–1667. https://doi.org/10.1016/j.corsci.2003.10.005.

[81] G.S. Frankel, Pitting Corrosion of Metals: A Review of the Critical Factors, J. Electrochem. Soc. 145 (2019) 2186–2198. https://doi.org/10.1149/1.1838615.

[82] L.C. Abodi, J.A. Derose, S. Van Damme, A. Demeter, T. Suter, J. Deconinck, Modeling localized aluminum alloy corrosion in chloride solutions under non-equilibrium conditions: Steps toward understanding pitting initiation, Electrochim. Acta. 63 (2012) 169–178. https://doi.org/10.1016/j.electacta.2011.12.074.

[83] K.D. Ralston, T.L. Young, R.G. Buchheit, Electrochemical Evaluation of Constituent Intermetallics in Aluminum Alloy 2024-T3 Exposed to Aqueous Vanadate Inhibitors, J. Electrochem. Soc. 156 (2009) C135. https://doi.org/10.1149/1.3076147.

[84] N. Birbilis, M.K. Cavanaugh, R.G. Buchheit, Electrochemical behavior and localized corrosion associated with Al7Cu2 Fe particles in aluminum alloy 7075-T651, 48 (2006) 4202–4215.

[85] N.D. Nam, V.D. Phung, P.T.P. Thuy, V.A. Dao, S.H. Kim, J.S. Yi, Corrosion behaviours of hot-extruded Al-xMg alloys, 8 (2019) 5246–5253. https://doi.org/10.1016/j.jmrt.2019.08.047.

[86] J.G. Brunner, N. Birbilis, K.D. Ralston, S. Virtanen, Impact of ultrafine-grained microstructure on the corrosion of aluminium alloy AA2024, Corros. Sci. 57 (2012) 209–214. https://doi.org/10.1016/j.corsci.2011.12.016.

[87] B. Sarkar, M. Marek, E.A. Starke, The effect of Copper Content and Heat Treatment on the Stress Corrosion Characteristics of Al-6Zn-2Mg-X Cu Alloys,

Metall. Trans. A, Phys. Metall. Mater. Sci. 12 A (1981) 1939–1943. https://doi.org/10.1007/BF02643806.

[88] J. Wloka, T. Hack, S. Virtanen, Influence of temper and surface condition on the exfoliation behaviour of high strength Al-Zn-Mg-Cu alloys, Corros. Sci. 49 (2007) 1437–1449. https://doi.org/10.1016/j.corsci.2006.06.033.

[89] W. Cheng, C.Y. Liu, H.F. Huang, L. Zhang, B. Zhang, L. Shi, High strength and ductility of Al–Si–Mg alloys fabricated by deformation and heat treatment, Mater. Charact. 178 (2021) 111278.

[90] M. Zha, H.-M. Zhang, X.-T. Meng, H.-L. Jia, S.-B. Jin, G. Sha, H.-Y. Wang, Y.-J. Li, H.J. Roven, Stabilizing a severely deformed Al–7Mg alloy with a multimodal grain structure via Mg solute segregation, J. Mater. Sci. Technol. 89 (2021) 141–149. https://doi.org/https://doi.org/10.1016/j.jmst.2021.01.086.

[91] L. Meng, Z. Wang, L. Wang, L. Guo, Z. Guo, Novel and efficient purification of scrap Al-Mg alloys using supergravity technology, Waste Manag. 119 (2021) 22–29. https://doi.org/https://doi.org/10.1016/j.wasman.2020.09.027.

[92] L.X. Bach, D.L. Son, M.T. Phong, L. V Thang, M.Z. Bian, N.D. Nam, A study on Mg and AlN composite in microstructural and electrochemical characterizations of extruded aluminum alloy, Compos. Part B Eng. 156 (2019) 332–343. https://doi.org/https://doi.org/10.1016/j.compositesb.2018.08.139.

[93] Y. Geng, I. Panchenko, S. Konovalov, X. Chen, Y. Ivanov, Effect of electron beam energy densities on the surface morphology and tensile property of additively manufactured Al-Mg alloy, Nucl. Instruments Methods Phys. Res. Sect. B Beam Interact. with Mater. Atoms. 498 (2021) 15–22. https://doi.org/https://doi.org/10.1016/j.nimb.2021.04.008.

[94] N. Qbau, N.D. Nam, N.X. Ca, N.T. Hien, The crack healing effect of scandium in aluminum alloys during laser additive manufacturing, J. Manuf. Process. 50 (2020) 241–246. https://doi.org/https://doi.org/10.1016/j.jmapro.2019.12.050.

[95] J. Bi, Z. Lei, Y. Chen, X. Chen, Z. Tian, X. Qin, J. Liang, X. Zhang, Effect of Al3(Sc, Zr) and Mg2Si precipitates on microstructure and tensile properties of selective laser melted Al-14.1Mg-0.47Si-0.31Sc-0.17Zr alloy, Intermetallics. 123 (2020) 106822.

[96] Y. Qi, H. Zhang, X. Nie, Z. Hu, H. Zhu, X. Zeng, A high strength Al–Li alloy produced by laser powder bed fusion: Densification, microstructure, and mechanical properties, Addit. Manuf. 35 (2020) 101346. https://doi.org/https://doi.org/10.1016/j.addma.2020.101346.

[97] X. Nie, H. Zhang, H. Zhu, Z. Hu, L. Ke, X. Zeng, Effect of Zr content on formability, microstructure and mechanical properties of selective laser melted Zr modified Al-4.24Cu-1.97Mg-0.56Mn alloys, J. Alloys Compd. 764 (2018) 977–986. https://doi.org/https://doi.org/10.1016/j.jallcom.2018.06.032.

[98] C. Suryanarayana, E. Ivanov, V. V Boldyrev, The science and technology of mechanical alloying, 306 (2001) 151–158. https://doi.org/https://doi.org/10.1016/S0921-5093(00)01465-9.

[99] C.C. Koch, The Synthesis of Non-Equilibrium Structures by Ball-Milling, Mater. Sci. Forum. 88–90 (1992) 243–262.

[100] J. Esquivel, R.K. Gupta, Simultaneous Improvement Of Mechanical and Corrosion Properties of Aluminum Alloys, Light Met. 2016. 151 (2016) 151–156. https://doi.org/10.1002/9781119274780.ch26.

[101] R.K. Gupta, D. Fabijanic, T. Dorin, Simultaneous improvement in the strength and corrosion resistance of Al via high-energy ball milling and Cr alloying, Mater. Des. 84 (2015) 270–276. https://doi.org/10.1016/J.MATDES.2015.06.120.

[102] L. Esteves, C.S. Witharamage, J. Christudasjustus, G. Walunj, S.P.O. Brien, S. Ryu, Corrosion behavior of AA5083 produced by high-energy ball milling, J. Alloys Compd. 857 (2020) 158268.

[103] J.M. Liang, M.T. Jia, X.Q. Guo, D.L. Zhang, Microstructural evolution and microhardness change of Al–7wt%Si–0.3wt%Mg alloy granules/powder particles during high energy ball milling, Mater. Sci. Eng. A. 590 (2014) 307–313. https://doi.org/https://doi.org/10.1016/j.msea.2013.10.050.

[104] F. Hadef, Synthesis and disordering of B2 TM-Al (TM=Fe, Ni, Co) intermetallic alloys by high energy ball milling: A review, Powder Technol. 311 (2017) 556–578. https://doi.org/https://doi.org/10.1016/j.powtec.2017.01.082.

[105] Y. Minamino, S. Saji, K. Hirao, K. Ogawa, H. Araki, Y. Miyamoto, T. Yamane, Diffusion of copper in nanocrystalline Al-7.8 at %Ti-0.3 at %Fe alloy prepared by mechanical alloying, Mater. Trans. JIM. 37 (1996) 130–137. https://doi.org/https://doi.org/10.2320/matertrans1989.37.130.

[106] C.C. Koch, J.D. Whittenberger, Mechanical milling/alloying of intermetallics, Intermetallics. 4 (1996) 339–355. https://doi.org/10.1016/0966-9795(96)00001-5.

[107] K.D. Ralston, N. Birbilis, M.K. Cavanaugh, M. Weyland, B.C. Muddle, R.K.W. Marceau, Role of nanostructure in pitting of Al-Cu-Mg alloys, Electrochim. Acta. 55 (2010) 7834–7842. https://doi.org/10.1016/j.electacta.2010.02.001.

[108] J.L. Searles, P.I. Gouma, R.G. Buchheit, Stress Corrosion Cracking of Sensitized AA5083 (Al-4.5Mg-1.0Mn), Metall. Mater. Trans. A. 32A (2001) 2859–2867. https://doi.org/https://doi.org/10.1007/s11661-001-1036-3.

[109] R.L. Holtz, P.S. Pao, R.A. Bayles, T.M. Longazel, Corrosion-Fatigue Behavior of Aluminum Alloy 5083-H131 Sensitized at 448 K (175 ° C), Metall. Mater. Trans. A. 43 (2012) 2839–2849. https://doi.org/10.1007/s11661-011-0866-x.

[110] L. Esteves, J. Christudasjustus, S.P. O'Brien, C.S. Witharamage, A.A. Darwish, G. Walunj, P. Stack, T. Borkar, R.E. Akans, R.K. Gupta, Effect of V content on corrosion behavior of high-energy ball milled AA5083, Corros. Sci. 186 (2021) 109465. https://doi.org/10.1016/j.corsci.2021.109465.

[111] B.C. Sousa, C. Walde, V.K. Champagne, A.T. Nardi, R.D. Sisson, D.L. Cote, Rapidly solidified gas-atomized aluminum alloys compared with conventionally cast counterparts: Implications for cold spray materials consolidation, Coatings. 10 (2020) 1–28. https://doi.org/10.3390/coatings10111035.

[112] J. R. Davis, Corrosion of Aluminum and Aluminum Alloys-ASM International, 1999. https://doi.org/DOI: 10.1361/caaa1999p001.

[113] P. Bhattacharya, P. Bellon, R.S. Averback, S.J. Hales, Nanocrystalline TiAl powders synthesized by high-energy ball milling: Effects of milling parameters on yield and contamination, J. Alloys Compd. 368 (2004) 187–196. https://doi.org/10.1016/j.jallcom.2003.08.079.

[114] C. Suryanarayana, Mechanical alloying and milling, Prog. Mater. Sci. 46 (2001) 1–184.

[115] R.A. Young, The rietveld method, 1993.

[116] S. Gates-rector, T. Blanton, The Powder Diffraction File : a quality materials characterization database, Powder Diffr. 34 (2019) 352–360. https://doi.org/10.1017/S0885715619000812.

[117] L. Lacroix, C. Blanc, N. Pébère, G.E. Thompson, B. Tribollet, V. Vivier, Simulating the galvanic coupling between S-Al2CuMg phase particles and the matrix of 2024 aerospace aluminium alloy, Corros. Sci. 64 (2012) 213–221. https://doi.org/10.1016/j.corsci.2012.07.020.

[118] M.A. Meyers, A. Mishra, D.J. Benson, Mechanical properties of nanocrystalline materials, Prog. Mater. Sci. 51 (2006) 427–556. https://doi.org/10.1016/j.pmatsci.2005.08.003.

[119] T. Shanmugasundaram, M. Heilmaier, B.S. Murty, V.S. Sarma, On the Hall – Petch relationship in a nanostructured Al – Cu alloy, 527 (2010) 7821–7825. https://doi.org/10.1016/j.msea.2010.08.070.

[120] D. Tabor, The hardness of metals, Oxford university press, 2000.

[121] C.S. Witharamage, J. Christudasjustus, R.K. Gupta, The Effect of Milling Time and Speed on Solid Solubility, Grain Size, and Hardness of Al-V Alloys, J. Mater. Eng. Perform. (2021) 1–15. https://doi.org/10.1007/s11665-021-05663-x.

[122] K.A. Darling, A.J. Roberts, L. Armstrong, D. Kapoor, M.A. Tschopp, L.J. Kecskes, S.N. Mathaudhu, Influence of Mn solute content on grain size

reduction and improved strength in mechanically alloyed Al–Mn alloys, Mater. Sci. Eng. A. 589 (2014) 57–65. https://doi.org/10.1016/j.msea.2013.09.047.

[123] K. Ma, H. Wen, T. Hu, T.D. Topping, D. Isheim, D.N. Seidman, E.J. Lavernia, J.M. Schoenung, Mechanical behavior and strengthening mechanisms in ultrafine grain precipitation-strengthened aluminum alloy, Acta Mater. 62 (2014) 141–155. https://doi.org/10.1016/j.actamat.2013.09.042.

[124] J.E. Bailey, P.B. Hirsch, The dislocation distribution, flow stress, and stored energy in cold-worked polycrystalline silver, Philos. Mag. 5 (1960) 485–497. https://doi.org/10.1080/14786436008238300.

[125] R.L. Fleischer, Solution hardening by tetragonal dist ortions: Application to irradiation hardening in F.C.C. crystals, Acta Metall. 10 (1962) 835–842. https://doi.org/10.1016/0001-6160(62)90098-6.

[126] J. Esquivel, R.K. Gupta, Influence of the V content on microstructure and hardness of high-energy ball milled nanocrystalline Al-V alloys, J. Alloys Compd. 760 (2018) 63–70. https://doi.org/10.1016/j.jallcom.2018.05.132.

[127] C.C. Koch, Nanostructured Materials Processing, Properties and Potential Applications Edited, William Andrew Publishing, New York, 2007.

[128] T.D. Shen, C.C. Koch, Formation, Solid Solution Hardening and Softening of Nanocrystalline Solid Solutions Prepared by Mechanical Attrition, Acta Mater. 44 (1996) 753–761. https://doi.org/https://doi.org/10.1016/1359-6454(95)00178-6.

[129] R.G. Buchheit, R.P. Grant, P.F. Hiava, B. Mckenzie, G. Zender, Local Dissolution Phenomena Associated with S Phase (Al2CuMg) Particles in Aluminum Alloy 2024-T3, J. Electrochem. Soc. 144 (1997) 2621–2628. https://doi.org/https://doi.org/10.1149/1.1837874.

[130] N. Birbilis, Y.M. Zhu, S.K. Kairy, M.A. Glenn, J.F. Nie, A.J. Morton, Y. Gonzalez-Garcia, H. Terryn, J.M.C. Mol, A.E. Hughes, A closer look at constituent induced localised corrosion in Al-Cu-Mg alloys, Corros. Sci. 113 (2016) 160–171. https://doi.org/10.1016/j.corsci.2016.10.018.

[131] R.K. Gupta, N.L. Sukiman, K.M. Fleming, M.A. Gibson, N. Birbilis, Electrochemical behavior and localized corrosion associated with Mg2Si particles in Al and Mg alloys, ECS Electrochem. Lett. 1 (2012) 2–4. https://doi.org/10.1149/2.002201eel.

[132] H.P. Godard, The corrosion of light metals, New York: John Wiley & Sons, 1967.

[133] F. Ozdemir, J. Christudasjustus, V.B. Vukkum, R.K. Gupta, Need of an Inert Atmosphere for high-energy ball milling of Al alloys, J. Mater. Eng. Perform. (2022) 10.1007/s11665-022-07309-y.

[134] C.S. Witharamage, J. Christudasjustus, R.K. Gupta, The Effect of Milling Time and Speed on Solid Solubility, Grain Size, and Hardness of Al-V Alloys, J. Mater. Eng. Perform. 30 (2021) 3144–3158. https://doi.org/10.1007/s11665-021-05663-x.

[135] A. Calka, W. Kaczmarek, J.S. Williams, Extended solid solubility in ball-milled Al-Mg alloys, J. Mater. Sci. 28 (1993) 15–18.

[136] M. Besterci, G. Jangg, M. Šlesár, J. Zrník, Dispersion strengthened Al-Al4C3 material prepared by mechanical alloying, Powder Metall. Process. 1 (2001) 59–69. https://doi.org/10.1016/j.matdes.2004.11.012.

[137] M. Takamichi, A. Kawaski, M. Leparoux, Graphene oxide-reinforced aluminum alloy matrix composite materials fabricated by powder metallurgy, J. Alloys Compd. 698 (2017) 807–813.

[138] B. Prabhu, C. Suryanarayana, L. An, R. Vaidyanathan, Synthesis and characterization of high volume fraction Al–Al2O3 nanocomposite powders by high-energy milling, Mater. Sci. Eng. A. 425 (2006) 192–200. https://doi.org/10.1016/j.msea.2006.03.066.

[139] G.S. Frankel, X. Chen, R.K. Gupta, S. Kandasamy, N. Birbilis, Effect of Vacuum System Base Pressure on Corrosion Resistance of Sputtered Al Thin Films Effect of Vacuum System Base Pressure on Corrosion Resistance of Sputtered Al Thin Films, J. Electrochem. Soc. 161 (2014) C195–C200. https://doi.org/10.1149/2.056404jes.

[140] H. Abdoli, M. Ghanbari, S. Baghshahi, Thermal stability of nanostructured aluminum powder synthesized by high-energy milling, Mater. Sci. Eng. A. 528 (2011) 6702–6707. https://doi.org/10.1016/j.msea.2011.05.057.

[141] H. Kotan, K.A. Darling, M. Saber, C.C. Koch, R.O. Scattergood, Effect of zirconium on grain growth and mechanical properties of a ball-milled nanocrystalline FeNi alloy, J. Alloys Compd. 551 (2013) 621–629. https://doi.org/10.1016/j.jallcom.2012.10.179.

[142] A. Valério, S.L. Morelhao, Usage of Scherrer's formula in X-ray diffraction analysis of size distribution in systems of monocrystalline nanoparticles, ArXiv Prepr. ArXiv1911.00701. (2019).

[143] J. Christudasjustus, T. Larimian, J. Esquivel, S. Gupta, A.A. Darwish, T. Borkar, Aluminum alloys with high elastic modulus, Mater. Lett. 320 (2022). https://doi.org/10.1016/j.matlet.2022.132292.

[144] N. Hansen, Hall – Petch relation and boundary strengthening, Scr. Mater. 51 (2004) 801–806. https://doi.org/10.1016/j.scriptamat.2004.06.002.

[145] I.N. Khan, M.J. Starink, A Multi-Mechanistic Model for Precipitation Strengthening in Al-Cu-Mg Alloys during Non-Isothermal Heat Treatments,

Mater. Sci. Forum. 519–521 (2006) 277–282.

[146] J. Esquivel, H.A. Murdoch, K.A. Darling, R.K. Gupta, Excellent corrosion resistance and hardness in Al alloys by extended solid solubility and nanocrystalline structure, 3831 (2018).

[147] J.A. Rotole, P.M.A. Sherwood, J.A. Rotole, P.M.A. Sherwood, Valence band x-ray photoelectron spectroscopic studies to distinguish between oxidized aluminum species, J. Vac. Sci. Technol. A. 17 (1999). https://doi.org/10.1116/1.581779.

[148] C.S. Witharamage, J. Christudasjustus, J. Smith, W. Gao, R.K. Gupta, Corrosion behavior of an in situ consolidated nanocrystalline Al-V alloy, Npj Mater. Degrad. 6 (2022). https://doi.org/10.1038/s41529-022-00225-5.

[149] T.R. Malow, C.C. Koch, Thermal stability of nanocrystalline materials, Mater. Sci. Forum. 225–227 (1996) 595–604.

[150] B.S. Murty, M.K. Datta, S.K. Pabi, Structure and thermal stability of nanocrystalline materials, Sādhanā. 28 (2003) 23–45.

[151] N. Birbilis, B. Hinton, Corrosion and corrosion protection of aluminium, Woodhead Publishing Limited, 2011.

[152] A.K. Mishra, R. Balasubramaniam, Corrosion inhibition of aluminum alloy AA 2014 by rare earth chlorides, Corros. Sci. 49 (2007) 1027–1044. https://doi.org/10.1016/j.corsci.2006.06.026.

[153] J. Li, B. Hurley, R. Buchheit, Inhibition Performance Study of Vanadate on AA2024-T3 at High Temperature by SEM, FIB, Raman and XPS, J. Electrochem. Soc. 162 (2015) C219–C227.

[154] X. Guo, B. Hurley, R.G. Buchheit, Encapsulation of NaVO3 as corrosion inhibitor into microparticles and its active corrosion protection for AA2024 based upon inhibitor control release, Corrosion. 71 (2015) 1411–1413. https://doi.org/10.5006/1913.

[155] R. Buchheit, A. Hughes, Chromate and Chromate-Free Coatings, in: Corros. Fundam. Test. Prot., 13th ed., ASM International, Materials Park, Oh, USA, 2003.

[156] D.S. Kharitonov, J.E. Soc, D.S. Kharitonov, C. Ornek, P.M. Claesson, J. Sommertune, I.M. Zharskii, I.I. Kurilo, J. Pan, Corrosion Inhibition of Aluminum Alloy AA6063-T5 by Vanadates : Microstructure Characterization and Corrosion Analysis Corrosion Inhibition of Aluminum Alloy AA6063-T5 by Vanadates : Microstructure Characterization and Corrosion Analysis, (2018). https://doi.org/10.1149/2.0341803jes.

[157] F. Ozdemir, R.K. Gupta, Influence of vanadium addition on corrosion behavior of high-energy ball milled aluminum alloy 2024, Mater. Corros. 1-8 (2022)

https://doi.org/10.1002/maco.202213478.

[158] F.H. Froes, O.N. Senkov, E.G. Baburaj, Synthesis of nanocrystalline materials - An overview, Mater. Sci. Eng. A. 301 (2001) 44–53. https://doi.org/10.1016/S0921-5093(00)01391-5.

[159] J. Christudasjustus, C.S. Witharamage, G. Walunj, T. Borkar, R.K. Gupta, The influence of spark plasma sintering temperatures on the microstructure , hardness , and elastic modulus of the nanocrystalline Al- x V alloys produced by high-energy ball milling, J. Mater. Sci. Technol. 122 (2022) 68–76. https://doi.org/10.1016/j.jmst.2022.02.008.

[160] B.L. Hurley, S. Qiu, R.G. Buchheit, Raman Spectroscopy Characterization of Aqueous Vanadate Species Interaction with Aluminum Alloy 2024-T3 Surfaces, J. Electrochem. Soc. 158 (2011) C125. https://doi.org/10.1149/1.3562557.

[161] J. Christudasjustus, M.R. Felde, C.. Witharamage, J. Esquivel, A.A. Darwish, C. Winker, R.K. Gupta, Age-hardening behavior, corrosion mechanisms, and passive film structure of nanocrystalline Al-V supersaturated solid solution, J. Mater. Sci. Technol. (2022).

[162] A. Valerio, S.L. Morelhao, Usage of Scherrer's formula in X-ray diffraction analysis of size distribution in systems of monocrystalline nanoparticles, Condens. Mater. Sci. (n.d.) 1–9.

[163] T. Uesugi, K. Higashi, First-principles studies on lattice constants and local lattice distortions in solid solution aluminum alloys, Comput. Mater. Sci. 67 (2013) 1–10. https://doi.org/10.1016/j.commatsci.2012.08.037.

[164] M. Iannuzzi, G.S. Frankel, Mechanisms of corrosion inhibition of AA2024-T3 by vanadates, Corros. Sci. 49 (2007) 2371–2391.

[165] R.K. Gupta, F. Mirza, M.U.F. Khan, J. Esquivel, Aluminum containing Na2CrO4: Inhibitor release on demand, Mater. Lett. 205 (2017) 194–197. https://doi.org/10.1016/j.matlet.2017.06.080.

[166] A. Canakci, F. Erdemir, T. Varol, S. Ozkaya, Formation of Fe – Al intermetallic coating on low-carbon steel by a novel mechanical alloying technique, Powder Technol. 247 (2013) 24–29. https://doi.org/10.1016/j.powtec.2013.07.002.

[167] N.R. Tailleart, R. Huang, T. Aburada, D.J. Horton, J.R. Scully, Effect of thermally induced relaxation on passivity and corrosion of an amorphous Al – Co – Ce alloy, Corros. Sci. 59 (2012) 238–248.

[168] V. V Zakharov, EFFECT OF SCANDIUM ON THE STRUCTURE AND PROPERTIES OF ALUMINUM ALLOYS, 45 (2003) 246–253.

[169] J.R. Davis, Corrosion of aluminum and aluminum alloys, in: ASM Int., 2000: pp. 1–24. https://doi.org/10.1361/caaa1999p001.

[170] I.J. Polmear, Light Alloys, Butterworth-Heinemann, 2005. https://doi.org/10.1016/B978-0-7506-6371-7.X5000-2.

[171] T.S. Srivatsan, A review of: "DISPERSION STRENGTHENED ALUMINUM ALLOYS" edited by Y.-W. Kim and W.M. Griffith TMS, Warrendale, Pennsylvania 795 pages, hardcover, 1988, Mater. Manuf. Process. 6 (1991) 565–568. https://doi.org/10.1080/10426919108934788.

[172] D.K. Mukhopadhyay, C. Suryanarayana, F.H. (SAM. Froes, Structural evolution in mechanically alloyed Al-Fe powders, Metall. Mater. Trans. A. 26 (1995) 1939–1946. https://doi.org/10.1007/BF02670665.

[173] X. Qi, N. Takata, A. Suzuki, M. Kobashi, M. Kato, Change in microstructural characteristics of laser powder bed fused Al–Fe binary alloy at elevated temperature, J. Mater. Sci. Technol. 97 (2022) 38–53. https://doi.org/10.1016/j.jmst.2021.04.038.

[174] W. Wang, N. Takata, A. Suzuki, M. Kobashi, M. Kato, High-temperature strength sustained by nano-sized eutectic structure of Al–Fe alloy manufactured by laser powder bed fusion, Mater. Sci. Eng. A. 838 (2022) 1–5. https://doi.org/10.1016/j.msea.2022.142782.

[175] T.T. Sasaki, T. Ohkubo, K. Hono, Microstructure and mechanical properties of bulk nanocrystalline Al-Fe alloy processed by mechanical alloying and spark plasma sintering, Acta Mater. 57 (2009) 3529–3538. https://doi.org/10.1016/j.actamat.2009.04.012.

[176] S.S. Nayak, M. Wollgarten, J. Banhart, S.K. Pabi, B.S. Murty, Nanocomposites and an extremely hard nanocrystalline intermetallic of Al-Fe alloys prepared by mechanical alloying, Mater. Sci. Eng. A. 527 (2010) 2370–2378. https://doi.org/10.1016/j.msea.2009.12.044.

[177] K. Ma, H. Wen, T. Hu, T.D. Topping, D. Isheim, D.N. Seidman, E.J. Lavernia, J.M. Schoenung, Mechanical behavior and strengthening mechanisms in ultrafine grain precipitation-strengthened aluminum alloy, Acta Mater. 62 (2014) 141–155. https://doi.org/10.1016/J.ACTAMAT.2013.09.042.

[178] J.M. Cubero-Sesin, M. Arita, Z. Horita, High Strength and Electrical Conductivity of Al-Fe Alloys Produced by Synergistic Combination of High-Pressure Torsion and Aging, Adv. Eng. Mater. 17 (2015) 1792–1803. https://doi.org/10.1002/adem.201500103.

[179] O.N. Senkov, F.H. Froes, V. V. Stolyarov, R.Z. Valiev, J. Liu, Microstructure of aluminum-iron alloys subjected to severe plastic deformation, Scr. Mater. 38 (1998) 1511–1516. https://doi.org/10.1016/S1359-6462(98)00073-6.

[180] T.T. Sasaki, T. Mukai, K. Hono, A high-strength bulk nanocrystalline Al-Fe alloy processed by mechanical alloying and spark plasma sintering, Scr. Mater. 57 (2007) 189–192. https://doi.org/10.1016/j.scriptamat.2007.04.010.

[181] J. Esquivel, R.K. Gupta, Corrosion Behavior and hardness of Al-M (M: Mo, Si, Ti, Cr) alloys, Acta Metall. Sin. (English Lett. 30 (2017) 333–341.

[182] I.K. Wernick, N.J. Themelis, Recycling metals for the envinronment, Annu. Rev. Energy Environ. 23 (1998) 465–497. https://doi.org/https://doi.org/10.1146/annurev.energy.23.1.465.

[183] D. Raabe, D. Ponge, P.J. Uggowitzer, M. Roscher, M. Paolantonio, C. Liu, H. Antrekowitsch, E. Kozeschnik, D. Seidmann, B. Gault, F. De Geuser, A. Deschamps, C. Hutchinson, C. Liu, Z. Li, P. Prangnell, J. Robson, P. Shanthraj, S. Vakili, C. Sinclair, L. Bourgeois, S. Pogatscher, Making sustainable aluminum by recycling scrap: The science of "dirty" alloys, Prog. Mater. Sci. 128 (2022). https://doi.org/10.1016/j.pmatsci.2022.100947.

[184] B.D. Saller, T. Hu, K. Ma, L. Kurmanaeva, E.J. Lavernia, A comparative analysis of solubility , segregation , and phase formation in atomized and cryomilled Al – Fe alloy powders, J. Mater. Sci. (2015). https://doi.org/10.1007/s10853-015-9019-8.

[185] P. Cornette, S. Zanna, A. Seyeux, D. Costa, P. Marcus, The native oxide film on a model aluminium-copper alloy studied by XPS and ToF-SIMS, Corros. Sci. (2020) 108837. https://doi.org/10.1016/j.corsci.2020.108837.

[186] B.R. Strohmeier, An ESCA Method for Determining the Oxide Thickness on Aluminum Alloys, 15 (1990) 51–56.

[187] L. Becker, Chemical elements by market price, (2018). http://www.leonland.de/elements_by_price/en/list (accessed June 14, 2022).

[188] S.K. Das, Emerging trends in aluminum recycling: Reasons and responses, TMS Light Met. 2006 (2006) 911–916.

[189] N.. Belov, A.. Aksenov, G.. Eskin, Iron in Aluminum Alloys Impurity and Alloying Element, Taylor & Francis, London, 2002.

[190] E.A. Starke, J.T. Staley, Application of modern aluminium alloys to aircraft, Fundam. Alum. Metall. Prod. Process. Appl. 32 (1996) 747–783. https://doi.org/10.1533/9780857090256.3.747.

[191] G. Svenningsen, M.H. Larsen, J.C. Walmsley, J.H. Nordlien, K. Nisancioglu, Effect of artificial aging on intergranular corrosion of extruded AlMgSi alloy with small Cu content, Corros. Sci. 48 (2006) 1528–1543. https://doi.org/10.1016/j.corsci.2005.05.045.

[192] P.M. Natishan, W.E.O. Grady, Chloride Ion Interactions with Oxide-Covered Aluminum Leading to Pitting Corrosion : A Review, J. Electrochem. Soc. (2014). https://doi.org/10.1149/2.1011409jes.

[193] P.M. Natishan, E. McCafferty, G.K. Hubler, Surface Charge Considerations in the Pitting of Ion-Implanted Aluminum, J. Electrochem. Soc. 135 (1988) 321–

327. https://doi.org/10.1149/1.2095608.

[194] J. Soltis, Passivity breakdown , pit initiation and propagation of pits in metallic materials – Review, Corros. Sci. 90 (2015) 5–22.

[195] Y. Estrin, A. Vinogradov, Extreme grain refinement by severe plastic deformation: A wealth of challenging science, Acta Mater. 61 (2013) 782–817. https://doi.org/10.1016/j.actamat.2012.10.038.

[196] K.A. Darling, A.J. Roberts, L. Armstrong, Influence of Mn solute content on grain size reduction and improved strength in mechanically alloyed Al–Mn alloys, Mater. Sci. Eng. A. 589 (2014) 57–65.

[197] X.C. Tong, A.K. Ghosh, Fabrication of in situ TiC reinforced aluminum, 6 (2001) 4059–4069.

[198] E. Teatum, K. Gschneidner, J. Waber, LA-2345, US Dep. Commer. Washington, DC. (1960).

[199] International Measures of Prevention, Application, and Economics of Corrosion Technologies Study, Houston, Texas, 2016. http://impact.nace.org/documents/Nace-International-Report.pdf.

CCC RightsLink

Home | Help | Live Chat | Sign in | Create Account

Corrosion behavior of a bulk nanocrystalline Al-Fe alloy

Author: F. Ozdemir,C.S. Witharamage,J. Christudasjustus,AA. Darwish,H. Okuyucu,R.K. Gupta
Publication: Corrosion Science
Publisher: Elsevier
Date: December 2022

Journal Author Rights

Please note that, as the author of this Elsevier article, you retain the right to include it in a thesis or dissertation, provided it is not published commercially. Permission is not required, but please ensure that you reference the journal as the original source. For more information on this and on your other retained rights, please visit: https://www.elsevier.com/about/our-business/policies/copyright#Author-rights

BACK | CLOSE WINDOW

CCC RightsLink

Home | Help | Email Support | Sign in | Create Account

Corrosion behavior of age hardening aluminum alloys produced by high-energy ball milling

Author: Furkan Ozdemir,Chathuranga Sandamal Witharamage,Ahmed Abdelazim Darwish,Hasan Okuyucu,Rajeev Kumar Gupta
Publication: Journal of Alloys and Compounds
Publisher: Elsevier
Date: 15 April 2022

Journal Author Rights

Please note that, as the author of this Elsevier article, you retain the right to include it in a thesis or dissertation, provided it is not published commercially. Permission is not required, but please ensure that you reference the journal as the original source. For more information on this and on your other retained rights, please visit: https://www.elsevier.com/about/our-business/policies/copyright#Author-rights

BACK | CLOSE WINDOW

SPRINGER NATURE LICENSE
TERMS AND CONDITIONS

Sep 10, 2022

This Agreement between Mr. Furkan Ozdemir ("You") and Springer Nature ("Springer Nature") consists of your license details and the terms and conditions provided by Springer Nature and Copyright Clearance Center.

License Number	5385350610494
License date	Sep 10, 2022
Licensed Content Publisher	Springer Nature
Licensed Content Publication	Journal of Materials Engineering and Performance
Licensed Content Title	Need of an Inert Atmosphere for High-Energy Ball Milling of Al Alloys
Licensed Content Author	F. Ozdemir et al
Licensed Content Date	Sep 8, 2022
Type of Use	Thesis/Dissertation
Requestor type	academic/university or research institute
Format	print and electronic
Portion	full article/chapter
Will you be translating?	no

Author of this Springer Nature content	yes
Title	Development of High Strength Corrosion Resistant Al Alloys
Institution name	Ankara Yildirim Beyazit University
Expected presentation date	Sep 2022
Requestor Location	Mr. Furkan Ozdemir Ankara, 06531 Turkey Attn: Aybu
Total	0.00 USD

Terms and Conditions

Springer Nature Customer Service Centre GmbH
Terms and Conditions

This agreement sets out the terms and conditions of the licence (the **Licence**) between you and **Springer Nature Customer Service Centre GmbH** (the **Licensor**). By clicking 'accept' and completing the transaction for the material (**Licensed Material**), you also confirm your acceptance of these terms and conditions.

1. Grant of License

1. 1. The Licensor grants you a personal, non-exclusive, non-transferable, world-wide licence to reproduce the Licensed Material for the purpose specified in your order only. Licences are granted for the specific use requested in the order and for no other use, subject to the conditions below.

1. 2. The Licensor warrants that it has, to the best of its knowledge, the rights to license reuse of the Licensed Material. However, you should ensure that the material you are requesting is original to the Licensor and does not carry the copyright of another entity (as credited in the published version).

1. 3. If the credit line on any part of the material you have requested indicates that it was reprinted or adapted with permission from another source, then you should also seek permission from that source to reuse the material.

CURRICULUM VITAE

PERSONAL INFORMATION

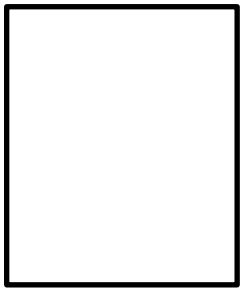

Name Surname **:** Furkan ÖZDEMİR

Date of Birth **:**

Phone **:**

E-mail **:**

EDUCATION

Bachelor **:** Middle East Technical University, Metallurgical and Materials Engineering, 2014

Master's degree **:** Middle East Technical University, Metallurgical and Materials Engineering, 2017

PhD degree : Ankara Yıldırım Beyazıt University, Materials Engineering, 2022

WORK EXPERIENCE

Research Assistant at Ankara Yıldırım Beyazıt University, 2016- on going

Research Scholar at North Carolina State University, 2020-2021

Research Scholar at University of Akron, 2019-2020

Project Assistant at Middle East Technical University, 2014-2016

Project Engineer/Trainee at Componenta b.v and Componenta A.S 2013-2014

TOPICS OF INTEREST

- Electrochemistry
- Experimental Metallurgy
- Corrosion
- Material Characterization

- Material processing - Failure Analysis
- Advanced Manufacturing - Process, Property, Performance Relationship

LIST OF PUBLICATIONS

F. Ozdemir, CS. Witharamage, J. Christudasjustus, AA. Darwish, H. Okuyucu, RK. Gupta, Corrosion behavior of a bulk nanocrystalline Al-Fe alloy, Corrosion Science, 2022, Submitted

F. Ozdemir, RK. Gupta, Influence of V addition of high energy ball milled AA2024, Materials and Corrosion, 2022

F. Ozdemir, CS. Witharamage, AA. Darwish, H. Okuyucu, RK. Gupta, Corrosion Behavior of Age Hardening Al Alloys Produced by High energy ball Milling, Journal of Alloys and Compounds, 2022

F. Ozdemir, J. Christudasjustus, V. Vukkum, H. Okuyucu, RK. Gupta, Need of inert atmosphere for high energy ball milling of Aluminum alloys, Journal of Materials Engineering and Performance, 2022

A.Patil, M. Nartu, **F. Ozdemir**, R. Banerjee, RK. Gupta, T. Borkar Effect of graphene morphology on the microstructure, mechanical and tribological behavior of nickel matrix composite, JOM, Submitted

V.Vukkum, **F. Ozdemir**, S. Storck, RK Gupta, Enhanced corrosion resistance of additively manufactured stainless steel by modification of feedstock, Corrosion Science, 2022

A.Patil, M. Nartu, **F. Ozdemir**, R. Banerjee, RK. Gupta, T. Borkar, Enhancement of the mechanical properties of graphene nanoplatelet (GNP) reinforced nickel matrix nanocomposites, Materials Science and Engineering: A, 2021

A.Patil, M. Nartu, **F. Ozdemir**, R. Banerjee, RK. Gupta, T. Borkar, Strengthening effects of multi-walled carbon nanotubes reinforced nickel matrix nanocomposites, Journal of Alloys and Compounds 2021

A.Patil, G. Walunj, **F. Ozdemir**, RK. Gupta, T. Borkar, Tribological Behavior of Carbon-Based Nanomaterial-Reinforced Nickel Metal Matrix Composites, Materials, 2021